Center for Environmentally Sustainable Transportation in Cold Climates

Development of Landslide Warning System

Beshoy Riad
Graduate Research Assistant

Xiong Zhang, Ph.D., P.E.
Associate Professor

Department of Civil, Architectural, and Environmental Engineering
Missouri University of Science and Technology

Date: November 2019

Prepared by: Beshoy Riad and Xiong Zhang
INE/CESTiCC 19.30

Center for Environmentally Sustainable Transportation in Cold Climates (CESTiCC)
Duckering Building, Room 245
P.O. Box 755900
Fairbanks, AK 99775

REPORT DOCUMENTATION PAGE

Form approved OMB No.

1. AGENCY USE ONLY (LEAVE BLANK)	2. REPORT DATE	3. REPORT TYPE AND DATES COVERED
	11/2019	Final Report: 09/2014 – 12/2019

4. TITLE AND SUBTITLE

Development of Landslide Warning System

5. FUNDING NUMBERS

6. AUTHOR(S)

Beshoy Riad, Graduate Research Assistant
Xiong Zhang, Ph.D., P.E.
Missouri University of Science and Technology

7. PERFORMING ORGANIZATION NAME(S) AND ADDRESS(ES)

Center for Environmentally Sustainable Transportation in Cold Climates
University of Alaska Fairbanks
Duckering Building, Room 245
P.O. Box 755900
Fairbanks, AK 99775-5900

8. PERFORMING ORGANIZATION REPORT NUMBER

INE/CESTiCC 19.30

9. SPONSORING/MONITORING AGENCY NAME(S) AND ADDRESS(ES)

University of Hawaii at Manoa
2500 Campus Rd, Honolulu, HI 96822

Center for Environmentally Sustainable Transportation in Cold Climates (CESTiCC)
Duckering Building, Room 245, P.O. Box 755900, Fairbanks, AK 99775

10. SPONSORING/MONITORING AGENCY REPORT NUMBER

11. SUPPLEMENTARY NOTES

12a. DISTRIBUTION / AVAILABILITY STATEMENT

No restrictions

12b. DISTRIBUTION CODE

13. ABSTRACT (Maximum 200 words)

Landslides cause approximately 25 to 50 deaths and US$1 - 2 billion worth of damage in the United States annually. They can be triggered by humans or by nature. It has been widely recognized that rainfall is one of the major causes of slope instability and failure. Slope remediation and stabilization efforts can be costly. An early warning system is a suitable alternative and can save human lives. In this project, an early warning system was developed for a 40-foot-high cut slope on the island of Hawaii. To achieve the objective, subsurface investigations were performed and undisturbed samples were collected. For the purpose of unsaturated soil testing, new testing apparatuses were developed by modifying the conventional oedometer and direct shear cells. The unsaturated soil was characterized using two separate approaches and, later, the results were discussed and compared. The slope site was instrumented for the measurement of suction, water content, displacement, and precipitation. The collected climatic data along with the calibrated hydraulic parameters were used to build an infiltration-evapotranspiration numerical model. The model estimations were compared with the field measurements and showed good agreement. The verified model was used to determine the pore-water pressure distribution during and after a 500-years return storm. Later, the pore-water pressure distribution was transferred to a slope stability software and used to study the slope stability during and after the storm. Based on a 2D slope stability analysis, the slope can survive the 500-year storm with a factor of safety of 1.20. Instrument threshold values were established for water content sensors and tensiometers using a traffic-light-based trigger criterion.

14- KEYWORDS: Unsaturated soils, Slope stability analysis, Elasto-plastic, Barcelona Basic Model, Field monitoring, Finite Element Modeling.

15. NUMBER OF PAGES: 163

16. PRICE CODE: N/A

17. SECURITY CLASSIFICATION OF REPORT	18. SECURITY CLASSIFICATION OF THIS PAGE	19. SECURITY CLASSIFICATION OF ABSTRACT	20. LIMITATION OF ABSTRACT
Unclassified	Unclassified	Unclassified	N/A

Development of Landslide Warning Systems

By

Beshoy Riad
Graduate Research Assistant

Xiong Zhang, Ph.D., P.E.
Associate Professor

Department of Civil, Architectural, and Environmental Engineering

Missouri University of Science and Technology

Performed in cooperation with

Center for Environmentally Sustainable Transportation in Cold Climates

and University of Hawaii Manoa

November 2019

DISCLAIMER

This document is disseminated under the sponsorship of the U.S. Department of Transportation in the interest of information exchange. The U.S. Government assumes no liability for the use of the information contained in this document. The U.S. Government does not endorse products or manufacturers. Trademarks or manufacturers' names appear in this report only because they are considered essential to the objective of the document.

Opinions and conclusions expressed or implied in the report are those of the author(s). They are not necessarily those of the funding agencies. This report does not constitute a standard, specification, or regulation.

METRIC (SI*) CONVERSION FACTORS

APPROXIMATE CONVERSIONS TO SI UNITS

Symbol	When You Know	Multiply By	To Find	Symbol
		LENGTH		
in	inches	25.4		mm
ft	feet	0.3048		m
yd	yards	0.914		m
mi	Miles (statute)	1.61		km
		AREA		
in^2	square inches	645.2	millimeters squared	cm^2 ft^2
	square feet	0.0929	meters squared	m^2
yd^2	square yards	0.836	meters squared	m^2
mi^2	square miles	2.59	kilometers squared	km^2
ac	acres	0.4046	hectares	ha
		MASS (weight)		
oz	Ounces (avdp)	28.35	grams	g lb
	Pounds (avdp)	0.454	kilograms	kg T
	Short tons (2000 lb)	0.907	megagrams	mg
		VOLUME		
fl oz	fluid ounces (US)	29.57	milliliters	mL gal
	Gallons (liq)	3.785	liters	liters ft^3
	cubic feet	0.0283	meters cubed	m^3
yd^3	cubic yards	0.765	meters cubed	m^3
		TEMPERATURE (exact)		
ºF temperature	Fahrenheit	5/9 (ºF-32)	Celsius temperature	ºC
		ILLUMINATION		
fc	Foot-candles	10.76	lux	lx
fl	foot-lamberts	3.426	candela/m^2	cd/cm^2
		FORCE and PRESSURE or STRESS		
lbf	pound-force	4.45	newtons	N psi
	pound-force per square inch	6.89	kilopascals	kPa

Note: Volumes greater than 1000 L shall be shown in m^3

These factors conform to the requirement of FHWA Order 5190.1A *SI is the symbol for the International System of Measurements

APPROXIMATE CONVERSIONS FROM SI UNITS

Symbol	When You Know	Multiply By	To Find	Symbol
		LENGTH		
mm	millimeters			0.039
inches		in		
m	meters			3.28
feet		ft		
m	meters			1.09
yards		yd		
km	kilometers			0.621
Miles (statute)		mi		
		AREA		
mm^2	millimeters squared		0.0016	square inches
in^2 m^2	meters squared		10.764	square feet
ft^2 km^2	kilometers squared		0.39	square miles
mi^2 ha	hectares		(10,000 m^2)	2.471
acres	ac			
		MASS (weight)		
g	grams			0.0353
Ounces (avdp)	oz			
kg	kilograms			2.205
Pounds (avdp)	lb mg	megagrams (1000 kg)		1.103
short tons	T			
		VOLUME		
mL	milliliters			0.034
fluid ounces (US)	fl oz			
liters	liters			0.264
Gallons (liq)	gal			
m^3	meters cubed			35.315
cubic feet	ft^3			
m^3	meters cubed			1.308
cubic yards	yd^3			
		TEMPERATURE (exact)		
ºC	Celsius temperature			9/5 ºC+32
Fahrenheit temperature	ºF			
		ILLUMINATION		
lx	lux			0.0929
foot-candles	fc			
cd/cm	candela/m^2			0.2919

ACKNOWLEDGMENTS

The authors wish to express their appreciation to the USDOT Tier 1 Center for Environmentally Sustainable Transportation in Cold Climates (CESTiCC) and University of Hawaii Manoa for providing financial support to this research project. The authors would also like to thank all members of the Project Technical Advisory Committee. Acknowledgment is extended to Drs. Philip Ooi, and Drs. Lin Li and Melia Iwamoto for their contributions with material collection, laboratory testing, and data analysis related to the project as well as their valuable discussions in this research.

TABLE OF CONTENTS

LIST OF FIGURES

LIST OF TABLES

EXECUTIVE SUMMARY

Rainfall-induced landslides on partially saturated soil slopes cause great damage to human lives and infrastructures. Although too many factors can affect the slope stability, rainfall is a well-recognized reason behind the instability and failures of slopes. Typically, slopes are triggered by wetting for the natural unsaturated state that causes an increase in the moisture content and the reduction of suction. This, in turn, leads to a decrease in the shear strength of the soil and the development of excessive deformations and mostly failures. Slope failure abatement usually entails employing costly mitigation measures include: retaining walls, grading, excavation, drainage, pinning, etc. A less costly alternative is an early landslide warning system.

Development of an early-warning system for rainfall-induced landslides requires understanding the influences of geology, topography, hydrological conditions, soil material properties, and human action on slope stability. Estimation of rainfall infiltration and evapotranspiration related to climatic conditions and characterization of the non-linear hydraulic and constitutive properties of the soil are two major challenges among these factors. In this study, in order to gain insight into the main factors affecting the landslide problem, an early warning system was developed for a 40-foot-high cut slope on the island of Hawaii.

In terms of soil characterization, in this study, instead of using suction-controlled testing apparatuses that are costly and time-consuming, constant water content (CWC) oedometer and direct shear tests are used. These tests have two main superiorities over the suction-controlled tests those are: (1) it requires minimal modifications to the conventional oedometer and direct shear apparatuses, and (2) it takes a concise time to perform a constant water content test (i.e., several hours). To measure the suction changes during testing, high-suction tensiometers were developed and mounted in the oedometer and direct shear cells. To validate the suitability of

constant water content test results for characterizing the unsaturated soils, suction-controlled triaxial (SCTX) tests were performed at the University of Hawaii at Manoa. The unsaturated soil was characterized using two separate approaches (based on CWC tests and SCTX tets) and, later, the results were discussed and compared that demonstrated the suitability of CWC test for unsaturated soils characterization.

A subsurface investigation program was conducted at the slope site. The program consisted of two boreholes in which SPT tests were performed. Disturbed and undisturbed samples were collected during boring. The collected samples were transported to two laboratories (i.e., University of Hawaii at Manoa and Missouri University of Science and Technology) for the purpose of testing. The slope site was instrumented for the measurement of suction (using tensiometer), water content (using water content sensors), displacement (using inclinometers), and precipitation (using rainfall logger). Continuous readings were collected from the monitoring instrumentations for the period from July 2017 to January 2018.

The collected climatic data along with the calibrated hydraulic parameters were used to build an infiltration-evapotranspiration numerical model. First, the collected climatic data, from the slope site and nearby weather stations, were used to formulate the climate-soil boundary conditions. Then, the climate-soil boundary conditions were used to estimate the amount of water the soil gains by infiltration (e.g., rainfall) as well as the amount of water it loses by evaporation or evapotranspiration. Later, HYDRUS software was used to build the hydraulic model. The main advantage of HYDRUS is the ability to consider the hydraulic hysteresis behavior of unsaturated soils. The model was validated by comparing the estimated suction and water content with the field measurements and showed good agreement. The verified model was

then used to determine the pore-water pressure distribution during and after a 500-years return storm.

The slope stability analysis was done by using SLOPE/W software in which the shear strength equation for unsaturated soils is implemented. The pore-water pressure distribution, calculated using HYDRUS during and after a 500-year storm, was transferred to SLOPE/W and used to study the slope stability during and after the storm. Based on a 2D slope stability analysis, the slope can survive the 500-year storm with a factor of safety of 1.20. Based on HYDRUS and SLOPE/W results, an instrument threshold values were established for water content sensors and tensiometers using a traffic-light-based trigger criterion.

Finally, in this study, a Finite Element Model was built to investigate the capabilities of the existing finite element software for studying such complex geotechnical problems. One of the most famous software for unsaturated soils is the CODE_BRIGHT. The Barcelona Basic Model (BBM) is implemented within the CODE_BRIGHT package. The previously calibrated BBM mechanical parameters, as well as the Soil Water Characteristic Curve parameters for the slope soil, were used to perform a hydro-mechanical analysis for the slope. However, after several trials, it was not viable for the software to capture the slope initial suction and water content distributions. This can be mainly attributed to the inability of the software to consider hydraulic hysteresis behavior. Therefore, there is room for growth and research in this area.

CHAPTER 1: INTRODUCTION

1.1 Problem Statement

The failure of soil slopes is a common phenomenon all over the world. Landslides result in 25–50 deaths/year and more than $2 billion/year in repair costs in the United States. Although landslides can be attributed to many factors, it has been widely recognized that rainfall is one of the major causes of slope instability and failure. Many researchers have reported slope failures due to rainfall infiltration (Alonso et al. 2003; Au 1998; Chen et al. 2006; Guzzetti et al. 2008; Gallage and Uchimura 2010). It is well accepted that failures of slopes are triggered by wetting starting from an unsaturated state, as a result of the increase in the moisture content and the reduction of suction. This, in turn, leads to a decrease in the shear strength of the soil and the development of deformations. For example, the 2014 Oso mudslide in Washington State was a rainfall-induced landslide that killed 43 people and led to a total loss of 10 billion dollars (Sun et al. 2015).

An early warning of the failure and instability of slopes can save human lives by allowing the evacuation of people living in the area and stopping the operation of roads near the slope. Development of such an early-warning system for rainfall-induced landslides requires understanding the influences of geology, topography, hydrological conditions, soil material properties, and human action on slope stability, and these are very complicated. Estimation of rainfall infiltration and evapotranspiration related to climatic conditions and characterization of the non-linear hydraulic and constitutive properties of the soil are two major challenges among these factors. The former is related to the amount of water entering and leaving the soil, and the latter represents the influence of the water content and associated stress change on slope stability.

Unsaturated soil gains water through rainfall infiltration and loses water by evaporation or by evapotranspiration. By definition, evaporation refers to the process by which water changes state from liquid to vapor and escapes from the bare soil surface to the atmosphere. Transpiration refers to the process by which water in the soil is absorbed by vegetation roots and transported via the xylem to the leaves, where, again, it changes state from liquid to vapor and escapes to the atmosphere from the leaf surface. The two processes usually occur simultaneously and are therefore referred to by one term, evapotranspiration. Two steps are involved in evapotranspiration: water vaporization and vapor removal. Energy is required to change the state of the water molecules from liquid to vapor. The principal source of heat energy for evapotranspiration is solar radiation from the sun and air temperature. The driving force for the water vapor removal process is the difference in relative humidity between the soil surface and the surrounding atmosphere. Wind speed also significantly influences the water removal process. Other factors such as soil permeability, soil water salinity (which is related to osmotic suction), and vegetation characteristics, also significantly influence the evapotranspiration rate. During a rainfall event, the amount of water entering the soils depends upon rainfall intensity, duration, soil topography, hydrological conditions, soil moisture conditions, and runoff. At present, there is no well-established model to directly relate these climatic factors to the possibility of rainfall-induced landslide.

In terms of soil characterization, a suction-controlled triaxial testing apparatus has been used extensively to characterize unsaturated soils. However, the apparatus is very sophisticated and, therefore, expensive. A suction-controlled triaxial testing apparatus typically costs more than 60,000 dollars, a price only a few research universities can afford. In addition, due to the extremely low permeability of unsaturated soils, it is very time-consuming to perform suction-controlled triaxial testing on such soils. It is common to take 2-3 months for just one test.

Furthermore, the behavior of unsaturated soils is complicated and influenced by many factors. Typically more than two dozen tests are needed to fully characterize one unsaturated soil. Consequently, 2-3 years are often needed to fully characterize the unsaturated soils at one site (e.g. Sivakumar 1993; Sharma 1998; Hoyos 1998). This has been the main obstacle for the implementation of unsaturated soil mechanics in engineering practice. Zhang (2016) found that the results from the suction-controlled triaxial test apparatus are problematic for unsaturated soil characterization. There is a great need for research in these directions.

1.2 Background

A slope has been selected as a test site for establishing landslide early warning systems. The slope was recently instrumented with tensiometers to measure suction and rainfall recording instruments. Data has been collected by a remote, real-time data logger to record transient responses during heavy rainstorms. Undisturbed soil specimens have been taken through a comprehensive site investigation program performed by the University of Hawaii at Manoa. In order to establish effective landslide early warning systems, some key issues must be addressed, such as estimation of rainfall infiltration and evapotranspiration related to climatic conditions and evaluation of the non-linear hydraulic and constitutive properties of the soil. The research team at the Tier 1 Center for Environmentally Sustainable Transportation in Cold Climates (CESTiCC) worked closely with researchers from UHM to solve problems in the process of developing these early warning systems for rainfall-induced landslides.

1.3 Objectives

This project intended to address some key research needs in the development of an early warning system for rainfall-induced landslides, such as the necessity of costly and sophisticated

equipment and the time-consuming testing process in the characterization of unsaturated soils, development of accurate infiltration-evaporation model, and prediction of slope failure under the influence of rainfall (climatic) events.

1.4 Research Methodology

The proposed research objectives were achieved through equipment development, laboratory testing, constitutive modeling, numerical simulation, and validation with field data. Specifically, equipment was developed to rapidly measure the soil-water characteristic curve, free-shrinkage curve, and stress-strain behavior for unsaturated soils. Laboratory tests were performed at both the University of Hawaii at Manoa (UHM) and Missouri University of Science and Technology (MST) to characterize unsaturated soils. The test results were compared and analyzed to develop advanced constitutive models for the tested soils. Some of the models were used in numerical analyses to analyze the slope stability under different rainfall events. The analysis results were validated through the field monitoring data.

The following major tasks were accomplished to achieve the objectives of this study:

- Task 1: Literature Review
- Task 2: Site Description and Field Monitoring
- Task 3: Development of Test Apparatus
- Task 4: Characterization of Soil Behavior and Constitutive Modelling
- Task 5: Calibration of the Infiltration-Evapotranspiration Model and Implementation
- Task 6: Slope Stability Analysis

- Task 7: Draft of Final Report and Recommendations

Task 1: Literature Review

The review covered current progress in the characterization of unsaturated soils. The emphasize was on (1) suction-controlled tests, undrained compression and shear tests with measurement of suction changes, and associated methods for analyzing the tests results for constitutive modeling purpose; (2) methods to estimate the evapotranspiration rate using field climatic data and an infiltration model for rainfall events; (3) available constitutive models for unsaturated soils, and (4) slope stability for unsaturated slopes. This task was accomplished through a critical review of technical literature and research in progress. Results from this task are presented in Chapter 2.

Task 2: Site Description and Field Monitoring

A 12.20m-high slope site in Hawaii was selected for this study. A subsurface investigation program was conducted to collect disturbed and undisturbed soil samples for testing and characterization. Later, the slope was instrumented with specific instrumentation to obtain data to validate the calculations. The field instruments consisted of (a) tensiometers for suction measurements, (b) water content sensors for gravimetric water content measurements, (c) inclinometers for displacement measurements, and (d) a rainfall gage for precipitation measurements. This task was performed by the research team at the University of Hawaii at Manoa. The field description and instrumentations are presented in Chapters 3 and 4.

Task 3: Development of Testing Apparatus

High suction tensiometers were developed for measuring suction by following the methods in the literature of Ridley and Burland (1993) and Tarantino and Mongiovi (2003).

Devices were also fabricated to quickly measure the soil-water characteristic curve and free-shrinkage curves for unsaturated soils. Existing equipment for saturated soils such as oedometer tests and direct shear tests were modified to characterize unsaturated soil behavior. Undrained soil tests were mainly used to quickly characterize unsaturated soils. This task is presented in Chapter 5.

Task 4: Characterization of Soil Behavior and Constitutive Modelling

Unsaturated soils specimens retrieved from the slope site in Hawaii were used for the systematic testing program. The equipment developed in task 3 was used to rapidly determine the soil-water characteristic curve. The developed high suction tensiometers (HST) were used to measure the soil suction during testing. The HST along with the modified triaxial, oedometer, direct shear, and unconfined compression apparatuses were used to perform undrained (i.e., constant water content) testing for the collected samples. Based on the experimental results, the unsaturated soil in the field was fully characterized. The test results were compared with the results obtained from UHM through suction-controlled triaxial tests for constitutive modeling purposes. This task is presented in Chapters 6 and 7.

Task 5: Calibration of the Infiltration-Evapotranspiration Model and Implementation

The constitutive model and the infiltration model were developed at UHM. Numerical analyses were performed to simulate the evapotranspiration and infiltration processes. Climatic conditions at the monitoring site were used as boundary conditions for the numerical simulations. The results were compared with the measured suction data to validate the models. UHM took the lead in this task with the help of MST. A full description of this task is presented in Chapter 8.

Task 6: Slope Stability Analysis

After the infiltration model was validated, parameter studies were performed to investigate different climatic conditions on slope stability. The results, alongside data collected from the tensiometers and rainfall recording instruments, plus information on storm duration from weather stations, were used to estimate the pore water pressures, changes in mechanical stresses and factors of safety during future rainstorms; and, ultimately, to identify the instrument threshold values when a landslide will be triggered. The results led to the development of a landslide warning system. UHM took the lead in this task with help from MST. This task is included in Chapters 9 and 10.

Task 7: Draft of Final Report and Recommendations

Upon completion of the aforementioned tasks, a final report was drafted. The report included a literature survey and discussion of the results of other researchers, a description of the research methods and approach for this project, the test procedures and results, numerical simulation validation and results, this project's findings and limitations, and suggestions for further study. The conclusions and recommendations are presented in Chapter 11.

CHAPTER 2: LITERATURE REVIEW

"Landslides are one of the most widespread and effective agents in sculpting the earth's surface" (Eckel 1958). Landslides and other geo-material movements cause approximately 25 to 50 deaths and from 1 to 2 billion dollars' worth of damage in the United States annually (Turner and Schuster 1996). Landslides can be triggered naturally or by human activities as well. Natural triggers include intense precipitation, earthquakes, scouring, and volcanic eruptions. According to recent surveys, half of the 40 most destructive worldwide landslides in the past century resulted from prolonged or intense rainfall (Sidle and Ochiai 2006). The U.S. Geology Survey reported that the most frequent and widespread damaging landslides in the U.S. are induced by prolonged or heavy rainfalls. The rainfall-induced landslides are shallow and cause the geo-material to move (i.e., debris flow) rapidly from upland to downhill. Landslide mitigation requires employing costly measures such as grading, excavation, drainage, pining, retaining structures, etc. A less costly alternative is an early warning system that is especially suited towards slopes that are prone to rainfall-induced landslides.

The occurrence of debris flows on the island of Oahu has been well-documented in a report by the U.S. Geology Survey (Peterson et al., 1993). Due to recent rainfall, the island of Oahu, Hawaii has experienced numerous landslides along the state highways and elsewhere. This encouraged the University of Hawaii at Manoa and the Center for Environmentally Sustainable Transportation in Cold Climates (CESTiCC) to launch a project to develop a site-specific landslide warning system for a precarious cut slope adjacent to the main thoroughfare just north of the Pali Highway. A site-specific landslide warning system can be developed empirically based on correlations between rainfall intensity/duration and previous slide occurrences (e.g., Keefer et al. 1987; Wilson 1992; Capparelli and Tiranti 2010; Greco et al. 2013), or

mechanistically, based on either principles of limit equilibrium (slope stability analysis; e.g., Eichenberger et al. 2013; Thiebes et al. 2014; Baum and Godt 2010; Kanjanakul et al. 2016) or based on soil volume change and stress-deformation behavior via a numerical analysis. Since the mechanistic approaches are more rational, they form the focus of this work. The development of such a mechanistic early-warning system requires understanding the influences of geology, topography, hydrological conditions, soil material properties, and human action on slope stability. Estimation of rainfall infiltration and evapotranspiration related to climatic conditions and characterization of the non-linear hydraulic and constitutive properties of the soil are two major challenges among these factors. The former is related to the amount of water entering and leaving the soil, and the latter represents the influence of the water content and associated stress change on slope stability.

The most challenging factors for developing an early-warning landslide system are (1) fully characterizing the unsaturated soils, (2) estimating the rainfall infiltration and evapotranspiration, (3) calibrating a suitable saturated-unsaturated transient flow model that is able to estimate the change in stress due to rainfall events, and (4) utilizing the appropriate model (slope stability or numerical) for factor of safety predictions and real-time warning. These factors are the main focus of this project and in the following section a literature review is provided for every factor separately.

2.1 Unsaturated Soil Testing and Characterization

Saturated soils are a special case of unsaturated soils in which the soils consist of two phases only (i.e., water and solid phases). This makes testing and analyzing saturated soils much simpler than unsaturated soils. Even though for saturated soils, there are some laborious tests that

take time and effort, such as the consolidated drained (CD) triaxial test which is called the slow test. Most of the existing saturated soil testing apparatuses and standards were built upon the major assumption that the soil pores are fully occupied by water. This assumption makes saturated soil testing and data analysis relatively easy. For saturated soils, the volume changes equal to the water volume flow in or out of the sample when the load is applied, which is easy to measure during testing using a volume gage. For unsaturated soils, the soil behavior is even more complicated due to the simultaneous presence of three phases (i.e., solid, water, and air phases) (Kohgo et al. 1993). As a consequence, the sample total volume change is no longer equal to water volume change because of the presence of air phase in soil pores. This makes the use of the conventional triaxial test insufficient for unsaturated soils. To overcome this limitation, Bishop and Donald (1961) adopted the first double-cell suction controlled triaxial apparatus (SCTX). Two significant modifications were made to change the conventional triaxial test into suction-controlled triaxial apparatus. The first one is the use of double cells to measure the volume change of unsaturated soil specimens. The second one is to replace the porous stone at the base pedestal with a high air entry (HAE) ceramic disc to control matric suction with the axis-translation technique (Hilf 1956).The SCTX is the most popular unsaturated soil testing system. Moreover, it allows researchers to control the stress, air, and pore water pressures separately to eliminate the complicated coupling effect. Besides, using SCTX test, the soil mechanical behavior under specific (pre-selected) stress paths could be investigated. Since the 1960s the SCTX test has been used by many researchers to study and investigate constitutive behaviors of unsaturated soils (Bishop and Blight 1963; Fredlund 1979; Fredlund and Morgenstern 1976; Fredlund et al. 1978; Fredlund and Morgenstern 1977; Jennings and Burland 1962; Matyas and Radhakrishna 1968; and Sivakumar 1993). However, there are many limitations for the SCTX test, such as the need for sophisticated equipment and the sensitivity of

measurements to temperature changes. Also, the SCTX test is a consolidated drained test. Because of large sample dimensions and low permeability of unsaturated soils, the SCTX test is very time consuming, laborious and costly. Usually, to fully characterize one unsaturated soil it takes several years (Hoyos Jr 1998; Sharma 1998; Sivakumar 1993).

The SCTX is established based on the divide and conquer approach, which implicitly includes an assumption that the unsaturated soil is stress path independent. However, it is well established that the unsaturated soil behavior is stress path-dependent (Zhang 2016). One significant additional limitation for the SCTX is that the results are theoretically problematic. The principals of SCTX were investigated and discussed by Zhang (2016). It was concluded that if the soil elastic behavior is stress path independent then the SCTX test results could be acceptable. However, the soil plastic behavior is stress path-dependent and the test results are only a collection of elastic behaviors of the soil with different pre-consolidation stresses and are always lower than the results from the idealized stress path as shown in Figure 1.1. Moreover, applying continuous load into the drained unsaturated soil will result in non-uniform suction changes within the sample. As a result, the sample cannot be considered as a representative elementary volume (REV). In other words, using SCTX test we made a good sample representing the field conditions to a non-REV sample. If the soil is not a REV, the test results cannot be used for constitutive modeling purposes (Zhang 2016). Because of the limitations mentioned above of the SCTX test and the non-availability in most of the universities and research centers due to high cost and time-consuming, there was a great need to develop and modify simple testing equipment for unsaturated soils to be used for common engineering projects.

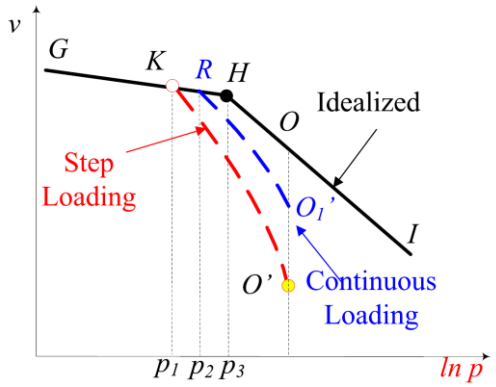

Figure 2.1 Schematic plot of the effects of loading procedure on suction-controlled triaxial test results (Zhang 2016).

To overcome the SCTX limitations, modifications were proposed to make the conventional saturated soil testing apparatuses (i.e., direct shear and oedometer apparatuses) suitable for unsaturated soils. For instance, Gan and Fredlund (1988) proposed the suction-controlled direct shear test, in which soil suction was controlled using the axis-translation technique, to characterize the shear strength of unsaturated soils. By testing different samples at different suction levels, the shear strength parameters could be determined based on Fredlund's equation (Fredlund et al. 1978). Later, the suction-controlled direct shear test was successfully used by many researchers to investigate unsaturated soils shear strength (De Campos and Carrillo 1995; Nam et al. 2011). However, sophisticated modifications are required to transform the conventional apparatus to a suction control purpose and are complicated to operate. Moreover, to control suction the water shall be allowed to flow in and out from the sample and, again, due to the extremely low permeability of unsaturated soils, suction-controlled tests could be time-consuming as well.

Similarly, the oedometer test was modified by several researchers to make it suitable for unsaturated soils by introducing a suction control system through axis-translation or vapor equilibrium technique (Dineen and Burland 1995; Kassiff and Shalom 1971; Maswoswe 1985;

Romero et al. 1995). The suction controlled oedometer test is much cheaper and relatively easier to perform compared to the SCTX. However, practically, it requires major modifications to the conventional oedometer cell and it takes a fair amount of time to run a test due to the long-time required for suction equilibrium. In the past, using the oedometer test results for constitutive modeling purposes was restricted due to the lack of any method to calculate the lateral stress. As a result, most researchers used the oedometer results for only verify their models, based on two assumptions: (a) elastic shear strains are small and negligible and (b) the K_0 consolidation line shares the same constant slope for saturated and unsaturated soils. Zhang et al. (2016a) demonstrated that these assumptions are problematic. Moreover, without any assumptions, they derived an explicit formulation for the at-rest coefficient and developed an optimization approach for simple and objective identification of the material parameters in elasto-plastic models for unsaturated soils using the results from suction-controlled oedometer tests.

With the recent developments in high-suction tensiometers, the matric suction changes can be easily measured. Based on this concept, Zhang et al. (2016b) modified a constant water content oedometer cell (CWOD) for unsaturated soils that is schematically presented in Figure 1.2. The major advantages of the modified cell are (1) no significant modifications are introduced to the conventional cell and (2) it takes a short time (only 4 to 7 hours) to run a CWOD for unsaturated soils, which is 300 to 400 times less than the time required for an SCTX test. In addition to the modified equipment, the method developed by Zhang et al. (2016a) can be utilized to identify the material stiffness parameters in elastoplastic models for unsaturated soils. Besides the stiffness parameters, the shear strength parameters shall be identified as well. However, the shear strength obtained using the approach developed by Zhang et al. (2016a) represents an extrapolation of soil shear strength behavior that is inaccurate.

In this project, a constant water content direct shear test is developed for the purpose of identifying the shear strength parameters for unsaturated soils. Similar to the CWOD, the conventional direct shear cell is equipped with a miniature high-suction tensiometer to measure suction changes during normal and shear loading. Knowing the suction value at failure, the equation proposed by Fredlund et al. (1978) can be used to adopt the unsaturated soil shear strength parameters.

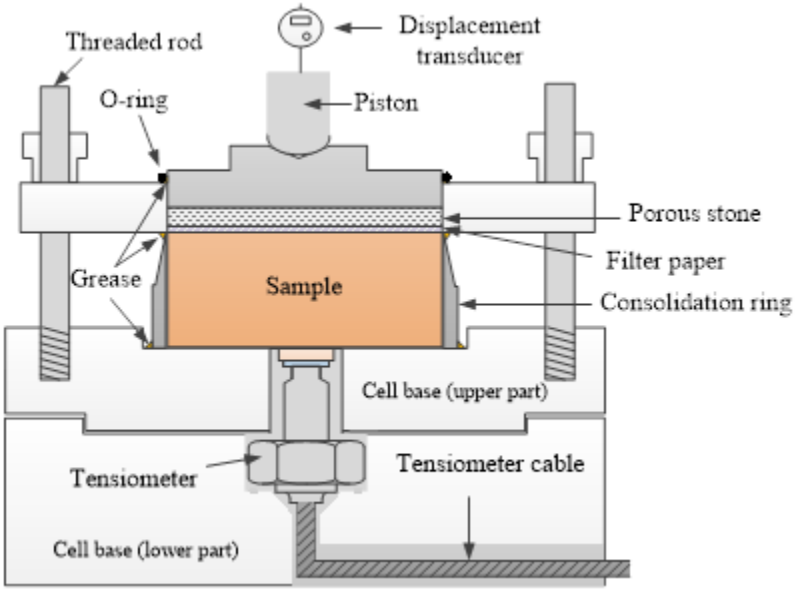

Figure 2.2 Modified one-dimensional oedometer cell (Zhang et al. 2016b).

2.2 Methods to Estimate the Infiltration and Evapotranspiration Rates

The study of unsaturated natural slopes is a very complicated problem. The climate (i.e., water loss or gain) significantly affects the shear strength of unsaturated soils. Water loss could be due to evaporation from ground surface or by transpiration from vegetation, which is referred as evapotranspiration. Water gain could be due to rainfall or any other form precipitation that provides water infiltration to the soil. Thus, weather conditions determine the boundary condition at the ground surface. A soil gains water by rainfall infiltration and loses water by

evapotranspiration. Although it is easy to find the amount of rainfall infiltration by direct measurements, tremendous efforts were aimed at evaluating the evapotranspiration values. Three general approaches are used extensively to estimate evapotranspiration: the temperature methods, the radiation methods, and the combination methods (Jacobs et al. 2001). The one that has gained considerable acceptance in the geotechnical field and is used by many researchers (e.g., Baum and Godt 2010, Kanjanakul et al. 2016, Rahardjo et al. 2013, and Zhang et al. 2018) is the combined method. The combined method equation was developed by Penman (1948) and later modified by Kohler and Parmele (1967). In this project the combined method was also utilized to provide an estimate for the evapotranspiration rates.

2.3 Hydro-Mechanical Constitutive Modeling

As previously mentioned, studying natural slopes landslides is a very complicated task due to the soil-climate interaction that subjects cycles of wetting and drying to the unsaturated soils. Hysteresis is a common feature in the mechanical (loading-unloading) behavior of soils in general and hydraulic (wetting-drying) behavior of unsaturated soils. Plastic strains may cumulate due to load combinations beyond the yield stress or due to hysteretic behavior of unsaturated soils. Consequently, slopes are suffering from deteriorations, plastic deformation, and, sometimes, failures (Turner and Schuster, 1996; Peterson et al., 1993; Wilson, 1992; Eichenberger et al., 2013, Thiebes et al., 2014, Baum and Godt, 2010, and Kanjanakul et al., 2016). The first elastoplastic model for unsaturated soils was pioneered by Alonso et al. (1990). The model was later referred to as the Barcelona Basic Model (BBM) and gained considerable acceptance within the unsaturated soils research community. Since then, a number of constitutive models have been proposed to simulate the mechanical behavior of unsaturated soils, and reviews of these models can be found in Gens (1996), Gens et al. (2006), and Sheng et al.

(2008a). However, Wheeler and Karube (1996) pointed out the inconsistency between the mechanical and hydraulic behaviors in the BBM that relate to using one simple elastic equation to simulate the hydraulic behavior which is inconsistent with the elastoplastic mechanical behavior.

Several models were proposed to simulate the hydraulic behavior of unsaturated soils intending to neglect the soil deformation (e.g., Van Genuchten, 1980; and Fredlund and Xing, 1994). These models described the degree of saturation change with suction and called Soil-Water Characteristic Curve (SWCC) or Soil-Water Retention Curve (SWRC) that were obtained from experimental tests under constant stresses. Since soil deformation was not included, the soils are implicitly assumed to be rigid. However, most of these models were developed for deformable soils in which the mechanical and hydraulic behaviors are coupled together. Hysteresis is a common feature in the hydraulic behavior of unsaturated soils. At a given matric suction value, the water content on a drying curve is always higher than that on a wetting curve. The hydraulic hysteresis may affect the mechanical behavior of unsaturated soils and vice versa. Vaunat et al. (2000) proposed the first coupled hydro-mechanical constitutive model for unsaturated soils with the main focus on considering the effect of hydraulic hysteresis on mechanical behavior. After that, several models were proposed to simulate the coupled hydro-mechanical behavior of unsaturated soils with considerable focus on the effect of hydraulic hysteresis on mechanical behavior (e.g., Buisson and Wheeler, 2000; Romero and Vaunat, 2014; Wheeler et al., 2003; Gallipoli et al., 2003a, 2003b; Simms and Yanful, 2005; Sheng et al. 2004, 2008; Tamagnini, 2004; Wheeler et al., 2004; Sun et al., 2007a, 2007b, 2010; Zhou and Sheng, 2009; Nuth and Laloui, 2008; Tarantino 2009; Masin, 2010; Sheng and Zhou, 2011). However, most of these models have limitations regarding consistency between hydraulic and mechanical behavior, and they require sophisticated experimental testing for unsaturated soil.

Recently, Zhang and Lytton (2009a and 2009b) proposed the Modified State Surface Approach (MSSA) to study the volume change for unsaturated soils using independent stress state variables (i.e., mean net stress and suction). In the MSSA, the void ratio constitutive surface was divided into an elastic surface and a plastic surface. The plastic surface is a unique constant surface, but the elastic surface is moveable, depending on the occurrence of the plastic deformation. The MSSA was used to explain the BBM and many other unsaturated soil behaviors. Later on, Zhang and Lytton (2011) extended the MSSA to study the coupled hydro-mechanical behavior of unsaturated soils. They paid special attention to the compatibility among the elastoplastic relations for the three soil phases. The BBM was used, then, to demonstrate how to use the MSSA to modify an existing model to simulate the hydro-mechanical behavior of unsaturated soils. One of the main challenges to most of the existing models is predicting an unsaturated soil behavior under undrained conditions in a consistent way. This challenge was addressed and resolved by the MSSA. The soil hysteresis behavior, both mechanical and hydraulic, of unsaturated soils was neglected during formulating the MSSA. Since only the BBM is implemented in some of the available software (e.g., CODE_BRIGHT and COMSOL), it is considered in this project. The BBM along with Van Genuchten (1980) model are used to study the hydraulic and mechanical behavior of the concerned slope.

2.4 Slope Stability for Unsaturated Slopes

Limit Equilibrium Analysis

The pore-water pressure calculated from a transient seepage analysis can be easily integrated into a slope stability analysis. Limit equilibrium methods (e.g., Bishop 1955; Price and Morgenstern 1965; Spencer 1967) that discretize the failure wedge into vertical slices, as shown

in Figure 1.3, have been widely utilized to assess the stability of saturated and dry slopes. For partially saturated soils slopes, the effect of suction on the shear strength shall be considered. Fredlund et al. (1978) proposed an equation for the shear strength of unsaturated soils considering the suction effect as an independent stress state variable. This equation is known as the extended Mohr-Coulomb failure criterion. By using the extended Mohr-Coulomb failure criterion, the conventional limit equilibrium methods can be easily modified for unsaturated soil slopes. The moment equilibrium (F_m) and force equilibrium (F_f) can be generally expressed as (Fredlund and Rahardjo 1993):

$$F_m = \frac{\sum\left[c'\Delta l R + \left(N - u_w \Delta l \frac{\tan\phi^b}{\tan\phi'}\right) R\tan\phi'\right]}{\sum Wx} \qquad \text{(Eq. 2.1)}$$

$$F_f = \frac{\sum\left[c'\Delta l\cos\theta + \left(N - u_w \Delta l \frac{\tan\phi^b}{\tan\phi'}\right)\tan\phi'\cos\theta\right]}{\sum N\sin\theta} \qquad \text{(Eq. 2.2)}$$

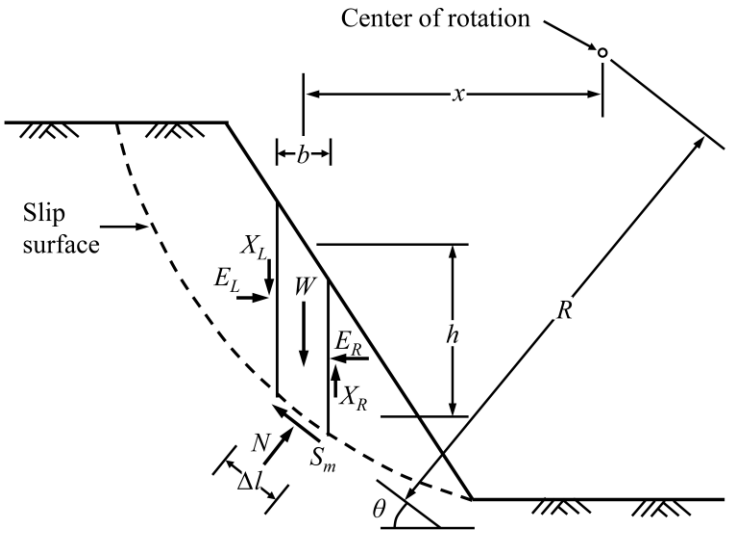

Figure 2.3 Forces acting on a slice of a failure wedge (modified from Fredlund and Rahardjo, 1993).

Several commercial software packages were adopted for the combined transient seepage and slope stability analysis (e.g., *SEEP/W* and *SLOPE/W*) (Ng and Shi 1998; Gasmo et al., 2000; Tsaparas et al. 2002; Huat et al., 2006; Rahardjo et al., 2007, 2010; Cascini et al., 2009; Rahimi et al., 2010). More specifically, any transient flow software can be used to calculate the pore water pressure (u_w) under a rainfall infiltration. Later, the obtained pore water pressure values can be transferred into a slope stability software (e.g., *SLOPE/W*). In this project, HYDRUS software was used to calculate the pore water pressure due to its ability to consider the hydraulic hysteresis behavior of unsaturated soils. Then, the obtained pore water pressure was transferred to SLOPE/W for slope stability analysis.

Although limit equilibrium analysis generally leads to satisfactory results for practical purposes, the analysis has been criticized for lack of a sound theoretical basis (Chen 2013; Miller and Hamilton, 1989; Michalowski, 1995; Yu et al., 1998). For instance, Lu et al. (2012) conducted a slope stability analysis and showed that the limit equilibrium method performs well if rational failure triggered; however, it may fail to search for the potential shallow slip surface if translation failure triggers.

Finite Element Analysis

Displacement of soil mass was totally neglected by the limit equilibrium methods (Fredlund and Rahardjo 1993). The calculated pore water pressure from transient flow analysis can also be integrated into a finite element slope stability analysis. The main advantage of using FEM is that the deformation triggered by stress changes is fully taken into account.

The slope stability global factor of safety can be obtained by using the shear strength reduction technique (Cai and Ugai 2004; Griffiths and Lu, 2005; Huang and Jia, 2009; Le et al., 2015). For a shear strength reduction technique, the soil cohesion (c) and ϕ' are incrementally

divided by a strength reduction factor (SRF) until excessive deformations are observed or the solution does not converge. The main principles of strength reduction method are:

$$c_d = \frac{c}{SRF},\ \phi_d' = \frac{\phi'}{SRF} \qquad \text{(Eq. 2.3)}$$

Alternatively, a local factor of safety (*LFS*) at one point can be obtained by finite element analysis. Lu et al. (2012) defined the LFS as the ratio of the available shear strength to the current shear strength at one point. The superiority of local factor of safety approach is that it could provide more insight if local failure is more critical (e.g., stress concentration at the toe of a vertical cut); however, it could not be used as an index to assess slope stability if global failure is more critical.

CHAPTER 3: SITE DESCRIPTION, SUBSURFACE INVESTIGATION, AND FIELD MONITORING

3.1 Location

A natural slope was selected in the state of Hawaii for slope stability analysis and developing a site-specific early warning system by the research team at the UHM (Iwamoto 2018). The 12.20-m-high cut slope is adjacent to Kalanianaole Highway on the southeast side of the island of Oahu, Hawaii with Le Jardin Academy lying on the northeast as shown in Figure 3.1.

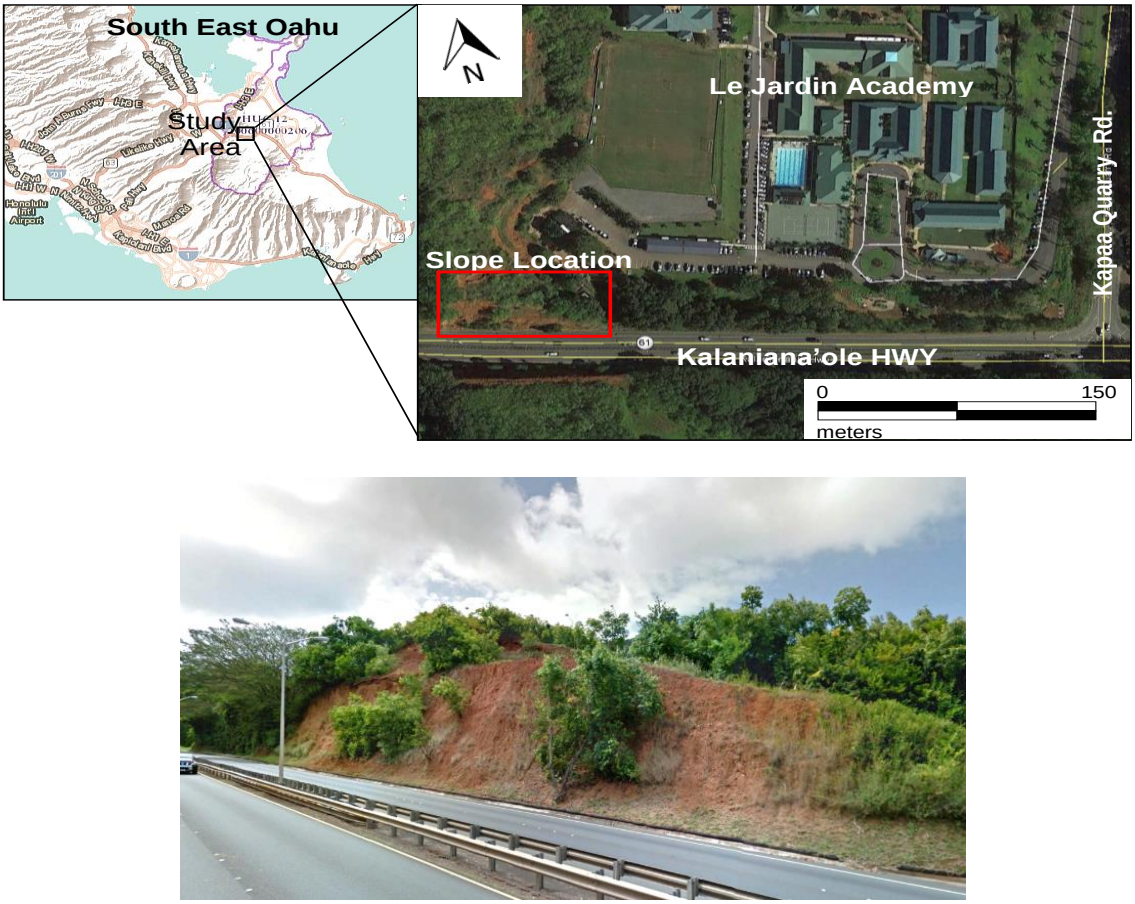

Figure 3.1 Location of the natural slope on Kalanianaole Highway (Google maps, 2017).

The elevation view of the slope is shown in Figure 3.2, where it can be seen that the lower and upper portions of the compound slope are 55^{o} and 63^{o}, respectively.

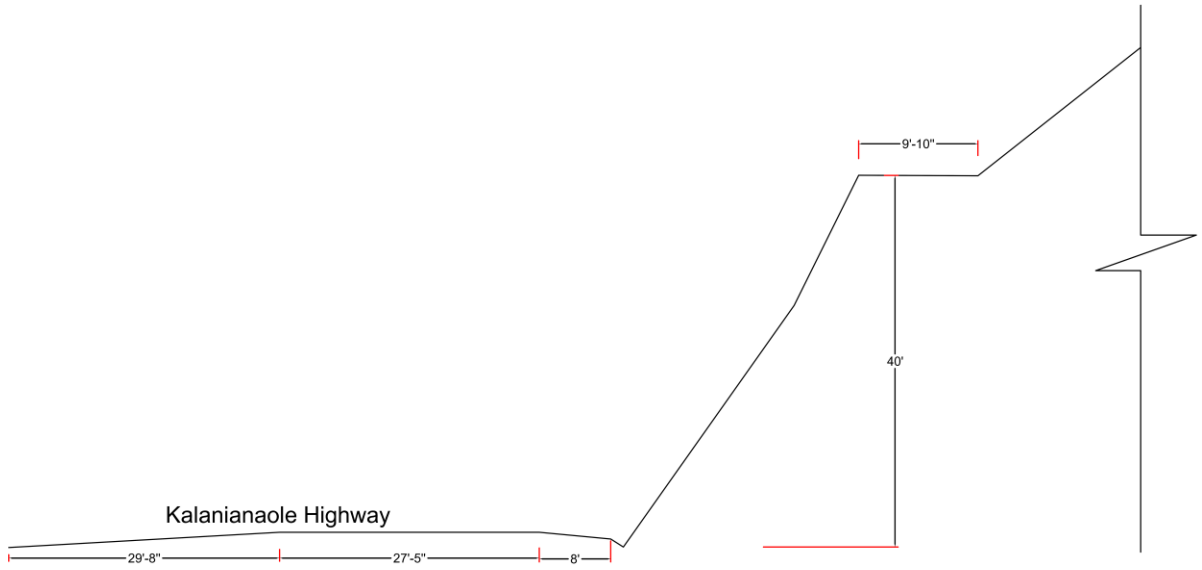

Figure 3.2 Cross-section view for the concerned slope (Iwamoto 2018).

3.2 Geology and Hydraulic Conditions

The island of Oahu was formed by the extrusion of basaltic lava from the Waianae and Koolau shield volcanoes. The older Waianae Volcano is estimated to be middle to late Pliocene in age and forms the western third of Oahu, while the Koolau Volcano is estimated to be late Pliocene to early Pleistocene in age and accounts for about the eastern two-thirds of Oahu. The Koolau and Waianae volcanos may have grown as separate islands but were eventually joined and saddled by the Leilehua Plateau (Hazlett and Hyndman 1996). The Leilehua Plateau and the Waianae volcano braced the western flank of the Koolau volcano (Figure 3.3). A portion of the steep, unsupported eastern flank eventually slid into the ocean as more and more magma rose into the volcano. Known as the Nuuanu slide, this is one of the largest known slides on earth. The slope lies within the Koolau caldera as shown in Figure 3.3. Rising hydrothermal fluids and

gases emanating from the active volcano has caused intense decomposition of the basaltic lava and breccia, and over time, this material has weathered into a saprolite. The slope crest lies about 50 m above the mean sea level (MSL). The groundwater table was not encountered in any of the drilled boreholes. However, according to Engott et al. (2017), the groundwater table at this site is about El. 5.80 m, which is 44.20 m below the slope crest.

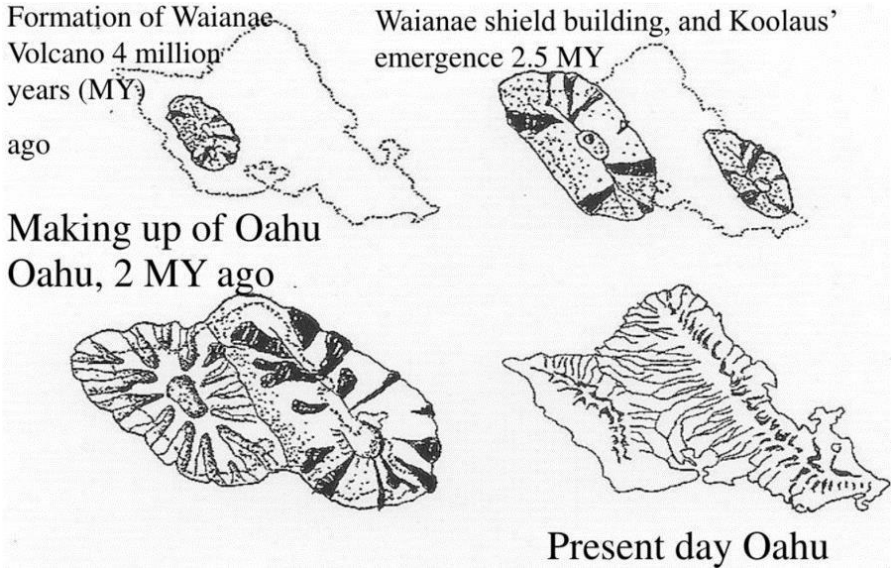

Figure 3.3 Formation of Oahu by coalescence of the Waianae and Koolau volcanoes (Carlquist 1970).

3.3 Nearby Historical Landslide

The current Pali Highway lies southeast of the concerned slope site. Since completion in the late 1950s, it has experienced a number of landslides, many of which have been documented by Torikai and Wilson (1992) and Macdonald et al. (1983). Two maps summarizing some of these slides are shown in Figures 3.4 and 3.5. Figure 3.4 from Deb and El-Kadi (2009) presents slides occurring before 2006. Figure 3.5 illustrates slope failures taken from a NASA landslide database which records globally occurring landslides from 2006 to the present.

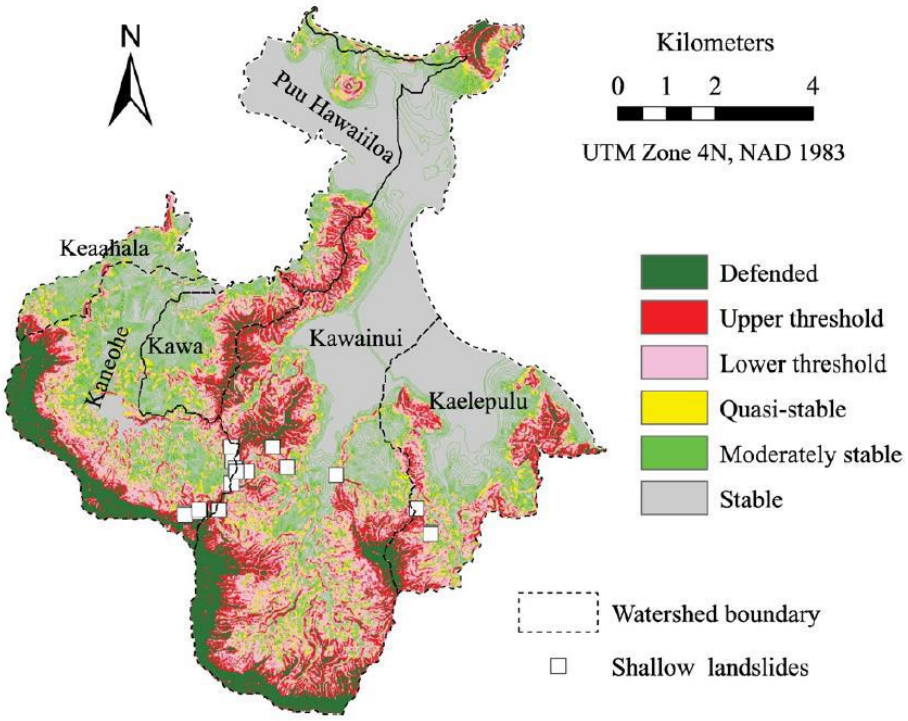

Figure 3.4 Locations of rainfall-induced shallow landslides from 1940 – 2006 (Deb and El-Kadi 2009).

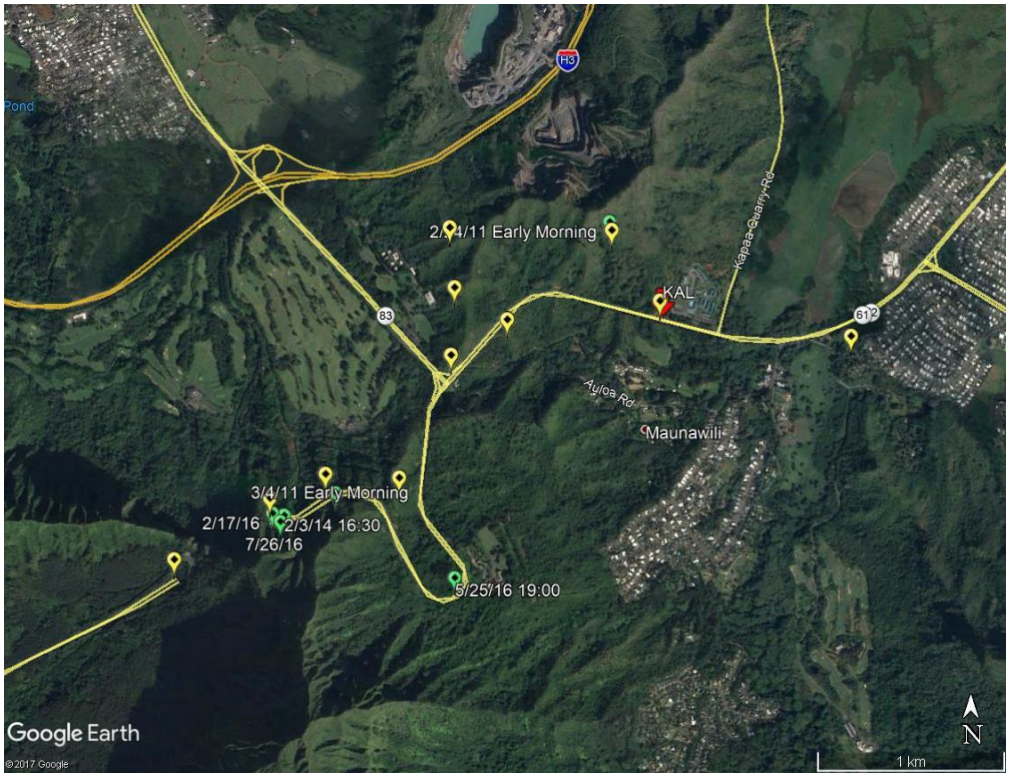

Figure 3.5 Map summarizing the locations of recent landslides (20011 – present) on Pali Highway and its vicinity (from Kirschbaum et al., 2010).

3.4 Geotechnical Investigation

The subsurface investigation program was provided and supervised by the UHM team (for more details refer to Iwamoto, 2018). Two boreholes nominated B2 and B3 were drilled by Geolabs, Inc, to a depth of 7.60 m (25 ft) with continuous sampling. Disturbed and undisturbed samples were collected through split-spoon and California samplers, respectively. Inclinometers casings were then inserted into the boreholes and grouted in-place after reaching the bottom of the borings. In-place inclinometers were then installed inside the casings in borings B2 and B3. In addition, boreholes were drilled nearby for the tensiometer installation and water content tensors. The boreholes, tensiometers and water content sensors locations and the corresponding depths are shown in Figure 3.6.

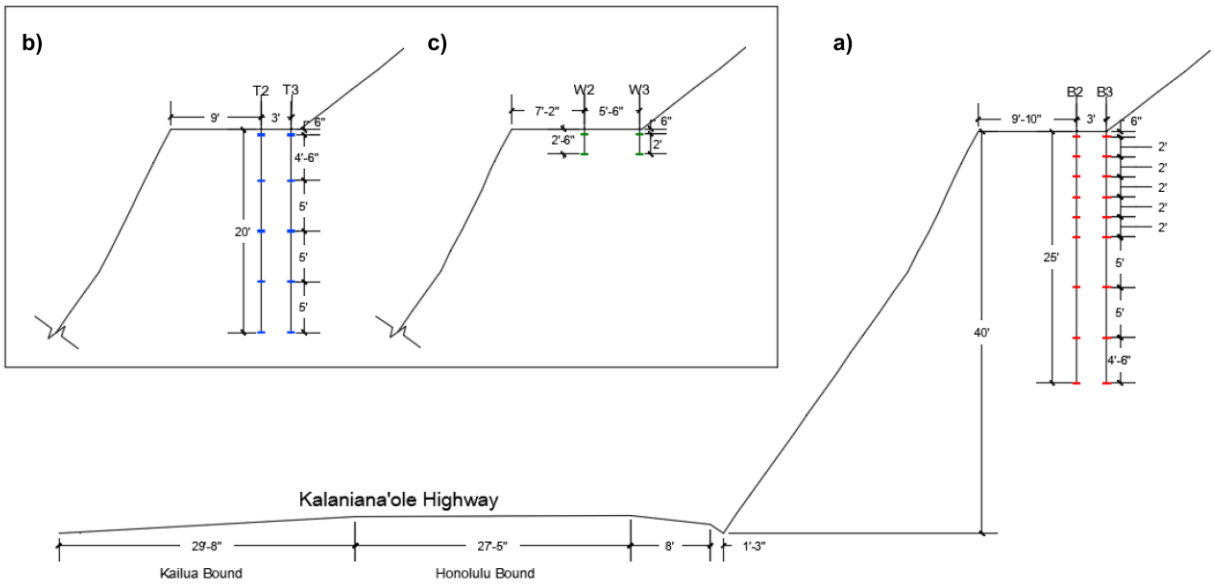

Figure 3.6 Instrumented slope (a) borehole locations, (b) tensiometers, and (c) water content sensors (Iwamoto, 2018).

Split spoon samples were used for index testing to measure the soil grain size distribution, atterberg limits, water content, and specific gravity. Soil samples from the

California samplers were utilized for shear and stiffness tests as well as to obtain the soil-water characteristic curve (SWCC).

Standard Penetration Test

Standard penetration tests (SPT) were conducted in both boreholes, and the collected soil was classified as red-brown stiff to very stiff uniform elastic silt (MH) or saprolite with more than 90% files. Figure 3.7 shows the SPT blow counts corrected for overburden plotted versus depth. The average corrected SPT value over the depth for both boreholes B2 and B3 is approximately 26 blows/ft.

Undisturbed Soil Samples

Modified California samplers were used to obtain relatively undisturbed soil samples because Shelby tubes would have likely crimped when pushed into such stiff soil and Picher samples were not available at the time of drilling. The modified California sampler is a thick-wall sampler that is driven into the soil using an SPT falling hammer. Strictly speaking, samples from the modified California Sampler are technically "disturbed" due to the large area ratio of the sampler and due to hammer advancement of the sampler. However, this was the only option provided by the driller to obtain soil samples for strength and stiffness testing. To reduce the effects of disturbance, the outer portion of the modified California samples were trimmed down from a diameter of 2.8 inches to 2.4 inches for strength testing, and to 2.5 inches for consolidation testing.

Approximately half of the collected undisturbed soil samples were tested at the University of Hawaii at Manoa (UHM), and the other half was provided to the MST team for the purpose of conducting constant water content consolidation and direct shear tests for calibrating

the Barcelona Basic Model (BBM) soil parameters. At the University of Hawaii, isotropic compression and constant water content triaxial tests were performed on the other half of samples. Simultaneously and independently, the BBM parameters were calibrated using test results from both groups (i.e., UHM and MST) to enable comparison of the parameters from both approaches to be made.

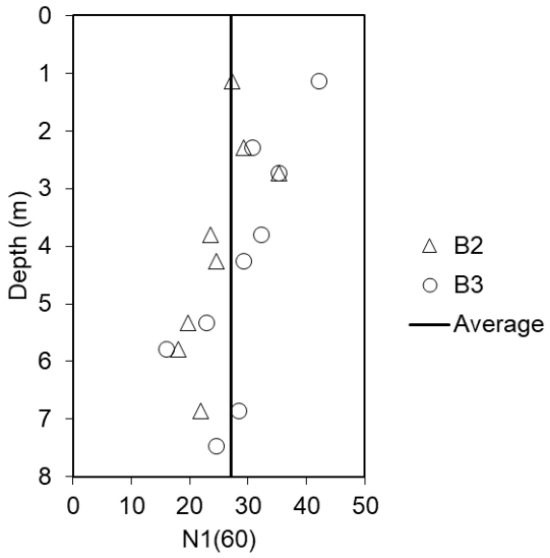

Figure 3.7 SPT blow counts versus depth (Iwamoto, 2018).

CHAPTER 4: FILED INSTRUMENTATIONS

4.1 Instrumentation Types, Layout and Installation

The field instrumentation program was designed, installed and monitored by the team at the University of Hawaii at Manoa (UHM). However a brief summary of the instrumentation activities and results are provided in this chapter (for detailed description refer to Iwamoto, 2018 Ph.D. thesis). Table 4.1 shows the installed instruments at the slope. The distribution of the instrumentations is shown in Figure 3.6.

Table 4.1 Instrumentation purpose and location.

Instrument	Purpose	Make, model and accuracy	Location	Depth
Inclinometer	To measure the lateral deflection of the slope	Geokon MEMs 6150-4 (±0.05 mm/m)	B2 and B3	≤7.62 m (25 ft)
Tensiometer	To measure soil suction	Decagon MPs-6 (±10% accuracy)	T2 and T3	≤6.1 m (20 ft)
Water content sensor	To measure soil water content	Decagon GS-3 (±3% accuracy)	W2 and W3	≤0.76 m (2.5 ft)
Rain gage	To measure precipitation	Campbell Scientific TE525WS-L tipping rain bucket (±1% accuracy)	Above ground	NA

The inclinometers were embedded down to a depth of 7.6 m (25 ft) below the slope crest, which is below the sliding surface for most rainfall-induced landslides (usually between 2 and 4 m deep according to (Eichenberger et al., 2013). Five tensiometers were installed each in boreholes T2 and T3 at depths of 0.15 m (0.5 ft), 1.52 m (5ft), 3.05 m (10 ft), 4.57 m (15 ft) and 6.1 m (20 ft). The measurable suction of Decagon MPS-6 tensiometers ranges from 9 to 100,000 kPa. Water content sensors were installed in boreholes W2 and W3 at depths of 0.15 m (0.5 ft) and 0.76 m (2.5 ft). Wires from all instruments were connected to two Geokon 16-channel multiplexers, which in turn was wired to a GEOKON Micro-1000 datalogger. The datalogger

was programmed to collect readings every 4 hours. The whole system was powered by a 12V battery charged by a solar panel during the day. A rain gage was housed separately from the datalogger and solar panel to minimize obstruction when collecting precipitation.

4.2 Field Measurements

This section presents the collected readings from the monitoring instrumentations for the period from July 2017 to January 2018.

Precipitation

Due to limited resources, only a rain gage was installed at the slope site rather than a comprehensive weather station that would provide all the data necessary to estimate the potential water evaporation. The rainfall record over the entire monitoring period is shown in Figure 4.1. There exists a gap in all the instrument data from 12/2/2016 to 1/27/2017 due to a 12V battery that had to be replaced and damage in the tensiometer cables. There were two other times when the rainfall data need to be corrected due to rain gage clogging. To correct the rainfall records, data from five nearby rain gages were collected and averaged using an inverse-distance-weighting method. The corrected and adjusted rainfall data shown in Figure 4.2.

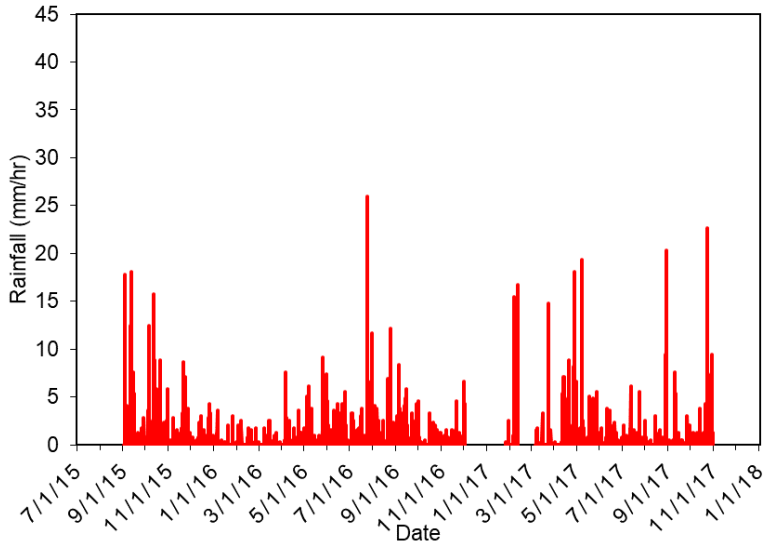

Figure 4.1 Rainfall record at the slope site (Iwamoto, 2018).

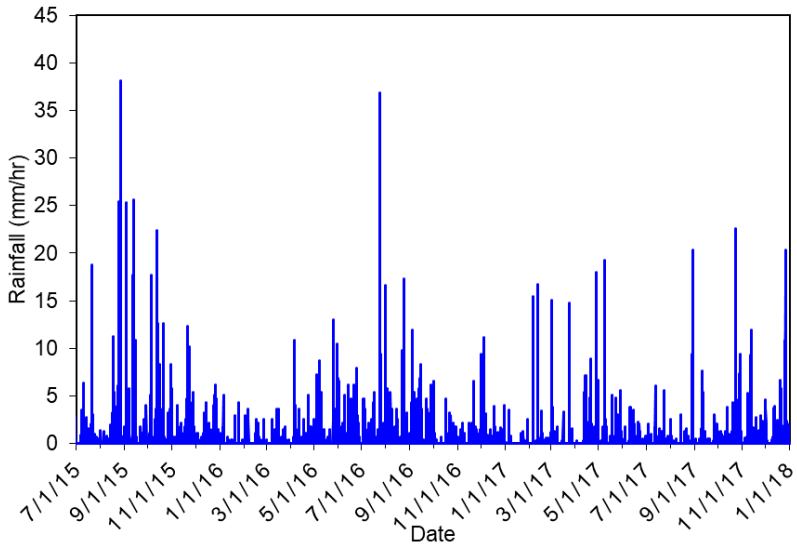

Figure 4.2 Corrected and adjusted rainfall data (Iwamoto, 2018).

Inclinometer

The inclinometers readings at different depths are shown in Figure 4.2. It is clear that the ground deflections were minimal (< 2 mm) during the monitoring period. This amount of deflection is probably within the tolerance error of the inclinometer. For all intents and purposes, the lateral deflections are considered negligible during the period of this study.

Tensiometer and Water Content Sensors

Suction is plotted versus time at the shallower tensiometers (≤1.5 m) in Figure 4.3a and the deeper tensiometers (≥3.0 m) in Figure 4.3b. From Figure 4.3, it is interesting to note that suctions are affected by precipitation mostly at shallow depths (<1.50 m). Beyond this depth, the soil suctions are fairly constant. Figure 4.4 shows the suction and water content sensor reading plotted in juxtaposition to show the interaction between them. The fact that suction decreases when water content increases illustrates that the instruments are responding logically.

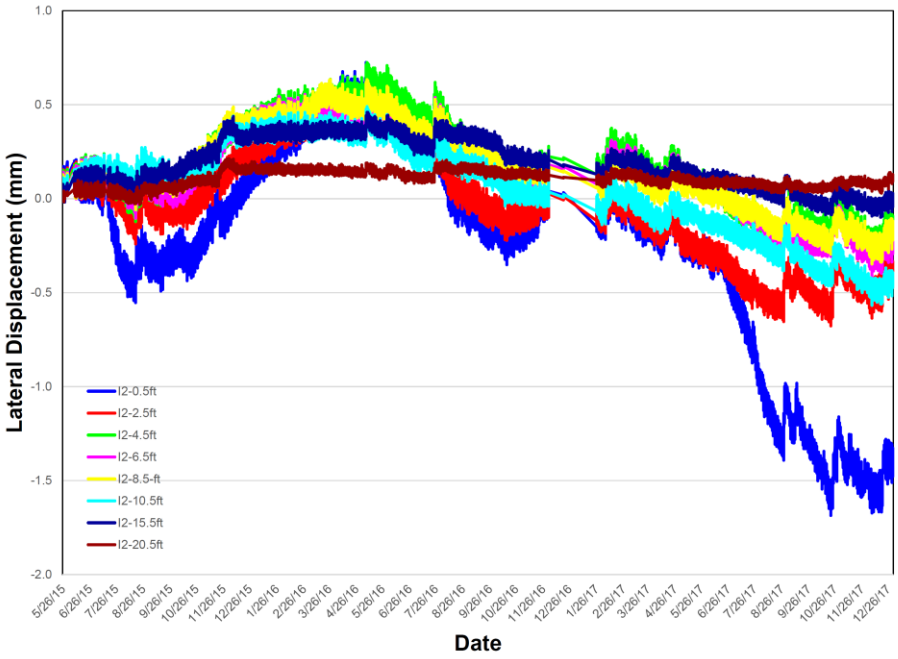

(a)

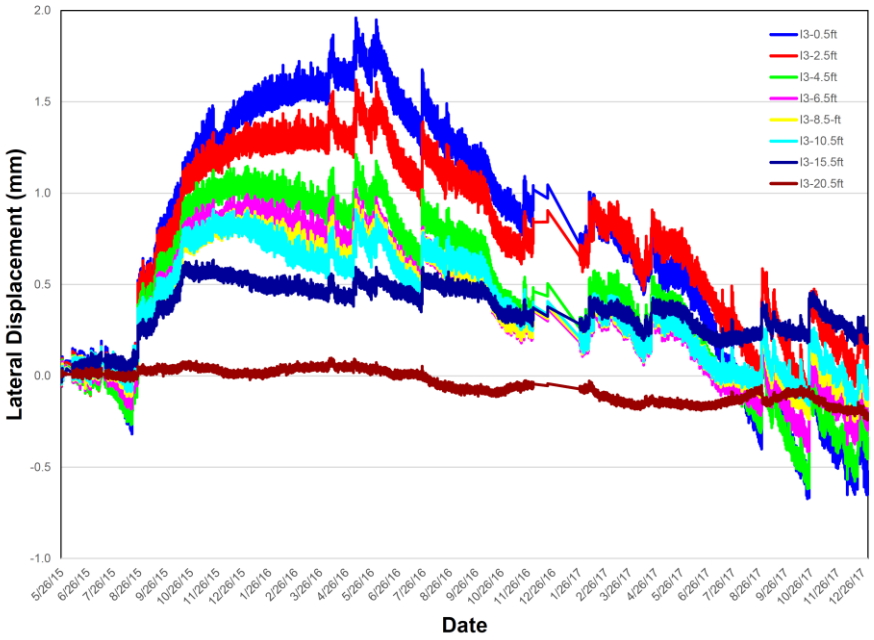

(b)

Figure 4.3 Inclinometer deflection readings at borings (a) B2 and (b) B3 (Iwamoto, 2018).

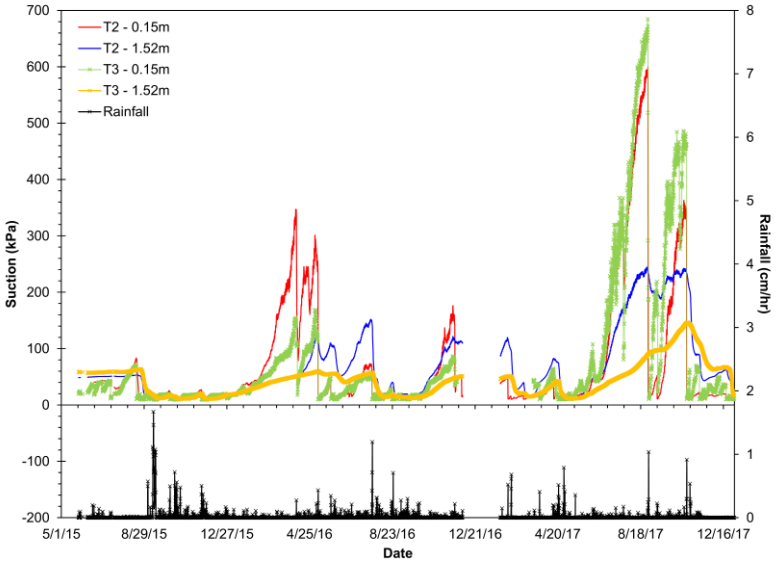

(a)

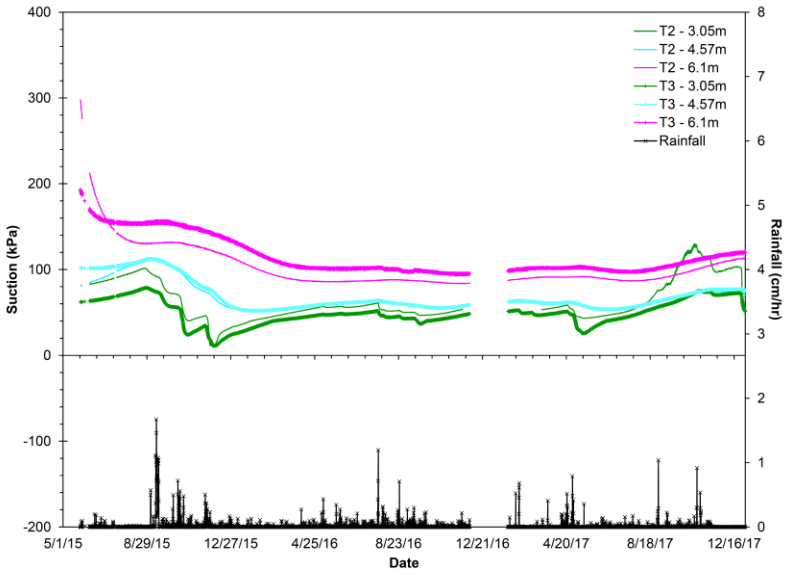

(b)

Figure 4.4 Suction versus time for (a) shallow tensiometers (⩽1.50 m deep) and (b) deep tensiometers (⩽3.0 m deep) (Iwamoto, 2018).

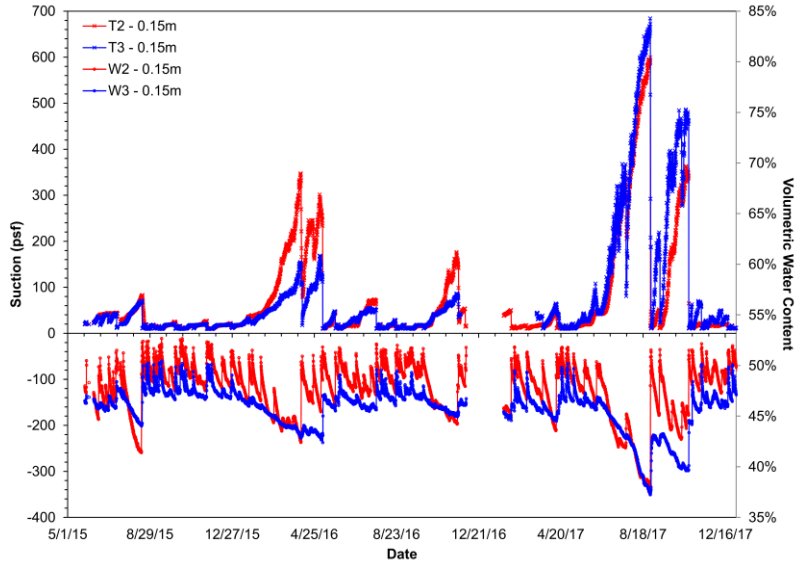

(a)

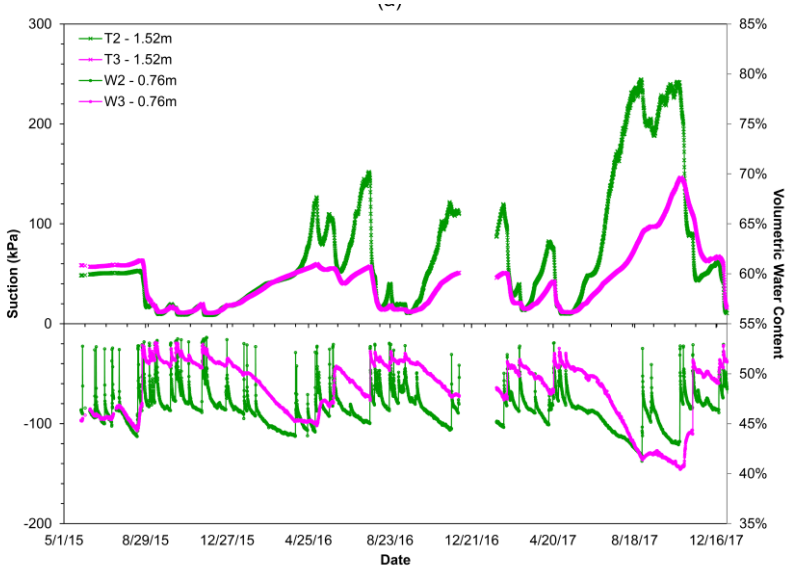

(b)

Figure 4.5 Suction and water content versus time for (a) 0.15 m deep tensiometers and (b) 1.5 m deep tensiometers (Iwamoto, 2018).

CHAPTER 5: DEVELOPMENT OF TEST APPARATUS

5.1 Introduction

In this chapter, the work done by the team at MST to develop apparatus for rapid testing for unsaturated soils is presented in detail. The work mainly consisted of developing high suction tensiometers to be equipped in a modified oedometer cell and direct shear apparatus. Then, the modified equipment was used for constant water content oedometer and direct shear tests. These modifications were done for the purpose of facilitating unsaturated soil testing. For saturated soils, due to the simplicity and equipment availability, the oedometer cell is widely used to characterize soil behavior. However, the conventional oedometer cell cannot be directly used for unsaturated soil investigation due to difficulties in measuring soil suction. Ridley and Burland (1993) developed the first high-suction tensiometer for direct suction measurements. Since then, several high-suction tensiometers have been developed and utilized for both laboratory and field suction measurements (Meilani et al., 2002; Take and Bolton, 2003; and Lourenço et al., 2006). Le et al. (2011) mounted a high-suction tensiometer on a conventional oedometer cell for direct suction measurement during undrained testing of unsaturated soils. Similarly, in this chapter, a new high-suction tensiometer is fabricated and, then, mounted on a modified oedometer cell and used for constant-water content oedometer cell. All details of fabrications and modifications are presented in this chapter.

The direct shear test is usually used to identify the saturated soil shear strength parameters. Different from saturated soils, the shear strength of unsaturated soils is significantly influenced by the suction value at failure. The shear strength of an unsaturated soil can be determined using modified direct shear or suction-controlled triaxial shear equipment (Escario

1980, Ho and Fredlund 1982, Gan and Fredlund 1988, Escario et al. 1989, Wheeler and Sivakumar 1993, Vanapalli et al. 1996). However, experimental studies related to the determination of the shear strength of unsaturated soils are time-consuming and require extensive and costly laboratory facilities. For this reason, the application of shear strength studies in engineering practice has been limited. In recent years, several semi-empirical shear strength functions were proposed to predict the shear strength of unsaturated soils. Vanapalli and Lane (2002) proposed a procedure that uses the saturated shear strength parameters (i.e., c' and φ') along with the soil-water characteristic curve to determine the unsaturated soil shear strength at the corresponding suction value. Obviously, this procedure built upon the major assumption that the suction value does not change significantly during shearing. However, this assumption is problematic because the volumetric changes in soils during shearing (i.e., contraction or dilation) will cause suction changes.

Moreover, the normal load applied during shearing causes suction changes. All the mentioned efforts were to eliminate the introduction of significant modifications into the direct shear apparatus, however, they made the simple test more complicated and time-consuming. Nowadays, using high suction tensiometer, the conventional direct shear test could be used with minimal modifications that do not affect the test simplicity and short time advantage. In this chapter, to characterize the shear strength of the Hawaii unsaturated soil, a modified direct shear apparatus was developed and described in detail.

5.2 Modified Oedometer cell

Literature Review

Conventional triaxial test apparatus designed to test saturated soils cannot be directly utilized for triaxial tests on unsaturated soils due to the difficulties in matric suction and volume change measurements. Bishop and Donald (1961) developed the suction-controlled triaxial test apparatus to characterize unsaturated soil behaviors. Since then, suction-controlled triaxial test, which is drained, has been extensively used to characterize unsaturated soil behaviors (Fredlund et al., 1978; Josa et al., 1987; Wheeler, 1988; Sivakumar, 1993; Romero et al., 1995; Ng et al., 2002; and Thu et al., 2006). However, suction-controlled triaxial tests are too laborious, time-consuming, and costly, and cannot be justified for routine engineering projects. Moreover, the SCTX test results are theoretically incorrect as presented in (Zhang 2016). Usually, it took months to years to characterize the stress-strain behavior of one unsaturated soil (Sivakumar 1993).

The one-dimensional oedometer compression test was reported to be utilized for unsaturated soil behavior investigation (Le et al. 2011). However, in this test, due to the unknown confining pressure, the test results cannot be used for soil constitutive behavior characterization. In the present study, a similar one-dimensional oedometer compression test system was presented to characterize unsaturated soil behaviors. The confining pressure generated by the oedometer compression ring was back-calculated based on the assumption that there is no lateral deformation during loading. Compared with the conventional suction-controlled triaxial test, the suction-monitored one-dimensional oedometer compression test significantly reduced the time required to characterize an unsaturated soil behavior from years to days.

The suction-monitored one-dimensional oedometer compression test equipment was modified based upon a conventional oedometer for a one-dimensional oedometer compression

test on saturated soils. Since the one-dimensional oedometer compression test was designed to investigate unsaturated soil behavior, under the undrained condition, soil suction would change due to the applied vertical stress. Thus, it was required to monitor soil suction change during loading. In Le et al. (2011), a high capacity tensiometer was adopted for the matric suction measurement. In this project, a newly designed high-suction tensiometer was utilized for the soil suction measurement.

Suction Measurement using High-Suction Tensiometer

In the past few decades, a great effort has been dedicated to measuring matric suction of unsaturated soils. Reviews of conventional suction measurement methods on unsaturated soil can be found in Fredlund and Rahardjo (1993), Ridley and Burland (1993), Ridley et al. (2003), and Rahardjo and Leong (2006). Based on the literature review on existing high-suction tensiometers, a new high-suction tensiometer, as schematically shown in Figure 5.1a, was developed based upon an EPXO pressure transducer. Similar to previously developed high-suction tensiometers (Ridley and Burland, 1993; Meilani et al., 2002; Lourenço et al., 2006), the tensiometer developed in this project as shown in Figure 5.1b included three parts: a pressure transducer, ceramic disc, and housing. However, unlike the other high-suction tensiometers, the ceramic disc was glued to a stainless steel ring (Figure 5.1b) instead of directly glued to the housing. To reduce the possibility of water cavitation under negative pressure and provide the room for the transducer diaphragm outward deformation, the thickness of the water reservoir was designed to be 0.2 mm. Ceramic disc with an air-entry value of 15 bar was used as a filter to prevent air from entering the water reservoir. The detailed fabrication process is presented in Li and Zhang (2014).

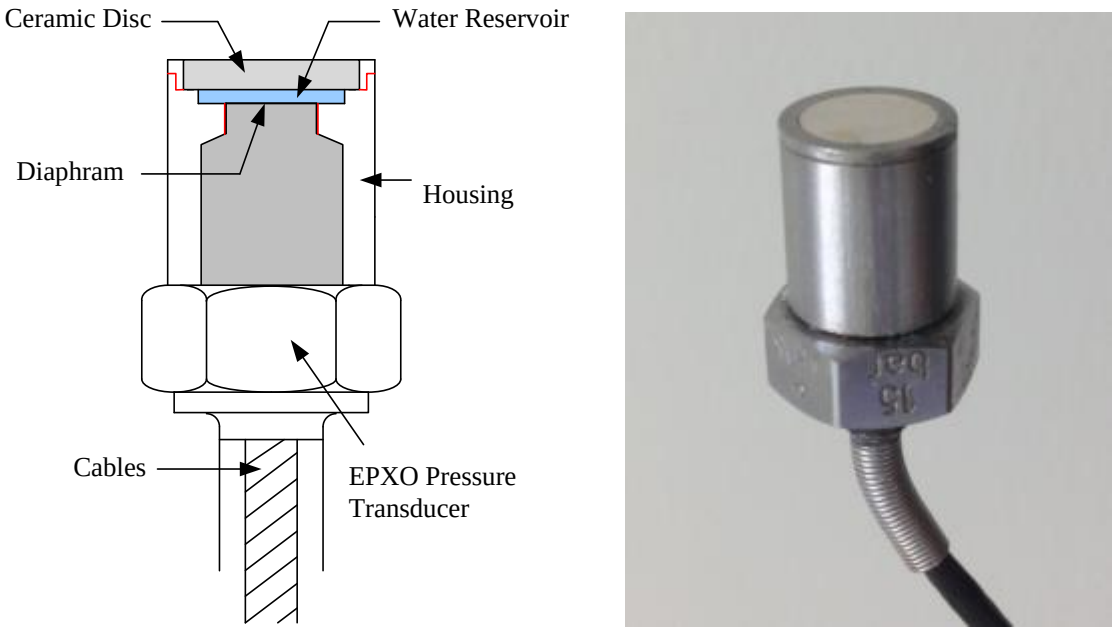

(a) Tensiometer design (b) Tensiometer picture

Figure 5.1 High-suction tensiometer (Li and Zhang 2014).

Oedometer cell modification

Since the one-dimensional oedometer compression test is to be performed on unsaturated soils under the undrained condition, the cell wall mounted on the pedestal of the oedometer is no longer required. Due to the use of high-suction tensiometers for matric suction measurement, a new cell base is required to accommodate the high-suction tensiometers. Oedometer modification is presented in Figure 5.2. A new cell base, the schematic design shown in Figure 5.2, was fabricated with a hole inside to hold the high-suction tensiometer in place. The new cell base has two parts. As shown in Figure 5.2, the tensiometer sits on the lower part. The upper part is in direct contact with the tested soil sample. The tensiometer is well aligned with the upper surface of the cell base to ensure good contact between the tensiometer and soil sample. The upper part of the oedometer is firmly fixed to the cell base through threaded rods as shown in Figure 5.2.

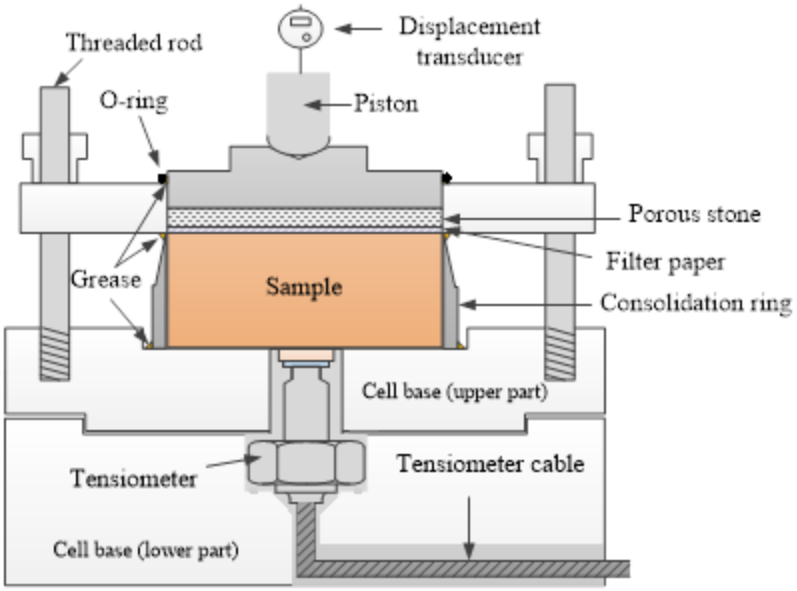

Figure 5.2 Modification on the cell base for a one-dimensional oedometer compression test.

A new cell base was fabricated with a hole inside to hold the high-suction tensiometer (Figure 5.3a) in place. The lower part of the new oedometer cell base is shown in Figure 5.3b. As shown in Figure 5.2, the tensiometer sits on the lower part which is also shown in Figure 5.3c. The upper part of the cell base as shown in Figure 5.3d is in direct contact with the tested soil sample. The tensiometer is designed to be aligned with the upper surface of the cell base as shown in Figure 5.3d to ensure good contact between the tensiometer and soil sample. An unsaturated soil sample inside the oedometer compression ring as typically shown in Figure 5.3e sits on the top of the upper part of the cell base. The upper part of the oedometer, which is the same as the conventional oedometer (2.5 inches fixed ring oedometer compression cell from Humboldt), is then firmly fixed to the cell base through threaded rods as shown in Figure 5.3f. The detailed fabrication process is presented in Li et al. (2015) and Zhang et al. (2016b).

In this project, the used tensiometer was saturated in a triaxial chamber. To achieve an accurate measurement, a high-suction tensiometer was calibrated in a positive pressure range after saturation. Negative pressure range calibration is based on extrapolation which was also

used in Lourenco et al. (2006). The accuracy of the calibration can be checked by the water pressure immediately after cavitation, which should be approximate -100 kPa. After saturation and calibration, the tensiometer was ready for matric suction measurement. The maximum attainable pressure of the high-suction tensiometer was determined to be approximately 1100 kPa through a free evaporation test presented by Guan and Fredlund (1997).

5.3 Modified Direct Shear Apparatus

Literature Review

In geotechnical engineering, the soil shear strength parameters are required for the most man-made earth structures such as highway embankments, earth dams, and foundations. In these man-made earth structures, the compacted unsaturated soils are commonly used. A safe and economic slope or foundation design is highly dependent on an accurate determination of the unsaturated soil shear strength. The water content plays a crucial role in advancing the understanding of unsaturated soil behavior. The influence of water content on the shear strength and constitutive behavior of unsaturated soils is found in many research efforts (e.g. Hilf, 1956; Fredlund and Morgenstern, 1978; Feddes et al., 1988; Fredlund and Rahardjo, 1993; Fredlund et al., 1996; Thu et al., 2006; Li and Zhang 2015a and 2015b). An increase in water content could cause a decrease in shear strength of unsaturated soils, one of the primary reasons for the failure of man-made earth structures and natural slopes (when induced to rainfalls).

(a) High-suction tensiometer

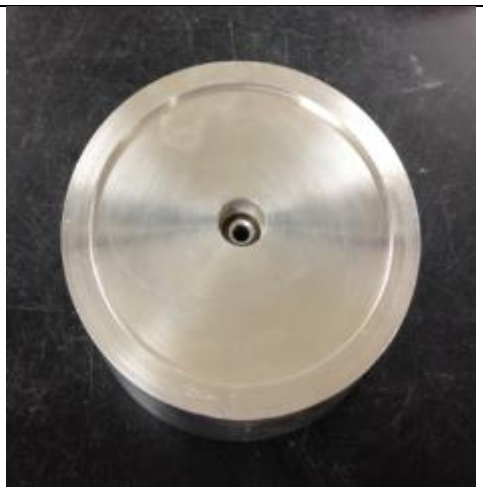

(b) Cell base (lower part)

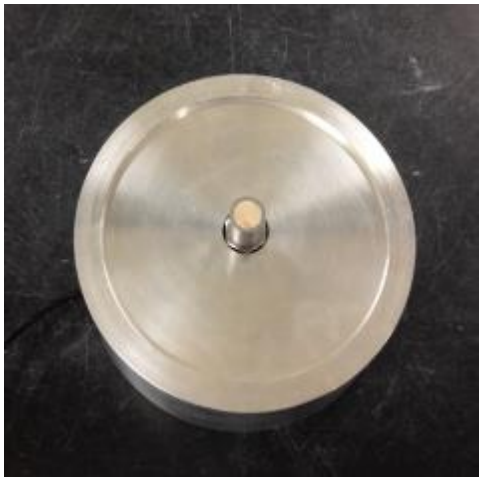

(c) Cell base with tensiometer

(d) Cell base (lower part)

(e) Unsaturated soil in a consolidation ring

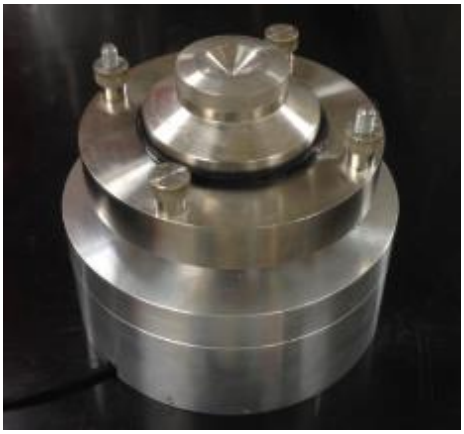

(f) Oedometer cell

Figure 5.3 Assembly for one-dimensional oedometer compression test

In the past, the conservative approach considered unsaturated soils as saturated for the design of man-made earth structures. However, this design (consider unsaturated soils to be saturated) can be over-conservative and wasteful under the following situations: (1) the structure is located in arid areas with limited water access; and (2) the structure is equipped with a well-designed drainage system. On the other hand, studying the stability of natural slopes from unsaturated soils requires precisely determining the unsaturated shear strength and evaluating the strength loss in case of rainfalls or water leakage. To design reliable and economically efficient structures and study natural slopes, the measurement of unsaturated soil shear strength has gained increasing attention in the past few decades (e.g., Bishop and Donald, 1961; Gan and Fredlund, 1988; and Li and Zhang, 2015a and 2015b).

Shear Strength of Unsaturated Soils

According to the Mohr-Coulomb failure criteria for saturated soils, a linear relationship exists between the shear strength and the net normal stress applied to the soil. For unsaturated soils, besides the net normal stress, the soil suction also plays an important role in the shear strength properties and soil failure criterion (Fredlund et al., 1978 and Khalili and Khabbaz, 1998). Fredlund et al. (1978) reported that besides the normal stress, the shear strength of unsaturated soils could be significantly influenced by the soil suction. Subsequently, a new shear strength equation was proposed for unsaturated soils using two independent stress state variables (net normal stress and matric suction) as shown in Equation 5.1.

$$\tau_f = c' + (\sigma - u_a)_f \tan\phi' + (u_a - u_w)_f \tan\phi^b \qquad \text{(Eq. 5.1)}$$

Where ϕ^b= angle indicating the rate of change in shear strength relative to changes in matric suction. Equation 5.1 was well accepted and widely used to model the shear strength of

unsaturated soils (e.g., Escario and Saez, 1986; Gan et al., 1988; Oloo and Fredlund, 1996; Vanapalli et al., 1996, Li and Zhang, 2015a; 2015b; Thu et al., 2006). As stated by Hamid and Miller (2009), the angle ϕ^b is approximately equal to ϕ' while the soil is saturated. However, once the air-entry value is exceeded, ϕ^b tends to decrease with increasing matric suction. As a result, the relationship between matric suction and shear stress becomes nonlinear which cannot be captured by Equation 5.1. To overcome this limitation, Vanapalli et al. (1996) proposed a nonlinear equation to model the shear strength of unsaturated soils (Equation 5.2) as a relation with the volumetric water content. The unsaturated soil shear strength prediction models were summarized in Garven and Vanapalli (2006). However, Equation 5.1 is more famous for practical use because of its simplicity.

$$\tau_f = c' + (\sigma - u_a)\tan\phi' + (u_a - u_w)\left[\tan\phi'\left(\frac{\theta - \theta_r}{\theta_s - \theta_r}\right)\right] \quad \text{(Eq. 5.2)}$$

Where θ is the soil volumetric water content, θ_r is the residual volumetric water content, and θ_s is the saturated volumetric water content.

Existing Tests to Characterize Shear strength of Unsaturated Soils

There are several well-established tests available for the determination of shear strength for a saturated soil in both laboratory and field such as direct shear, triaxial, unconfined compression, and vane shear. However, all these conventional methods cannot be directly used to determine the shear strength for unsaturated soil due to the difficulties of soil suction measurement. Bishop and Donald (1961) proposed the use of a double wall triaxial cell for measuring the shear strength of unsaturated soils in which the suction was controlled using axis-translation technique proposed by Hilf (1956). However, as discussed previously, the suction-controlled triaxial test is very laborious and time-consuming due to the low permeability of

unsaturated soils. Li and Zhang (2015a) proposed a modified unconfined compression system that was developed and used to characterize the shear strength behavior of unsaturated soils under low net confining stresses through constant water content triaxial tests. In this system, the confining load was applied through vacuum pressure. During testing, the soil suction was measured through two high-suction tensiometers mounted at the middle height of the unsaturated soil sample. The adoption of a constant water content test significantly reduced the time required for the unsaturated soil shear strength characterization when compared with the suction-controlled triaxial test. However, the major disadvantage of this system is that the applied confining stress was limited to 100 kPa due to water cavitation when applying confining stress through vacuum pressure. Besides using the unconfined compression system, several researchers utilized the constant water content triaxial test to characterize the shear strength for unsaturated soils (e.g., Thu et al., 2006 and Li and Zhang, 2015b). With this system, the constitutive behavior and shear strength of unsaturated soils can both be characterized by the constant water content triaxial tests on unsaturated soils with different initial soil suction and confining pressure conditions. Besides the triaxial test as discussed above, similar to saturated soils, the shear strength properties of unsaturated soils can also be determined through direct shear tests. Theoretically, as long as the soil suction at failure is known, both suction-controlled and constant water content direct shear tests can be used to characterize the shear strength of unsaturated soils. However, the stress paths for two tests are different, both tests are discussed in detail in the following sections.

Suction-Controlled Direct Shear Test

Gan et al. (1988) developed a suction-controlled direct shear test, as schematically shown in Figure 5.4, to characterize the shear strength of unsaturated soils. Similar to the suction-

controlled triaxial test, the axis-translation technique was also used to control soil suction during shearing. An additional chamber was added to the direct shear cell to facilitate the adoption of the axis-translation technique. Using this system, the shear strength properties of a glacial till were successfully determined. This system was later adopted by Miller and Hamid (2006) and Hamid and Miller (2009) for shear strength characterization on different unsaturated soils. The soil specimens used in the direct shear tests were thin when compared to those used in the triaxial tests. As a result, the time required for direct shear testing was reduced when compared with the suction-controlled triaxial test. However, as presented in Gan et al. (1988), this testing apparatus required significant modifications to the conventional direct shear apparatus for the suction control purpose and was complicated to operate. Besides the experimental methods as discussed above, the shear strength properties of unsaturated soils can be predicted theoretically by combining the soil shear strength parameters at saturated status with the soil water retention curve as proposed by Fredlund et al. (1996). However, this method suffers a significant limitation related to the effect of the hysteresis behavior as well as the influence of specific volume and loading history.

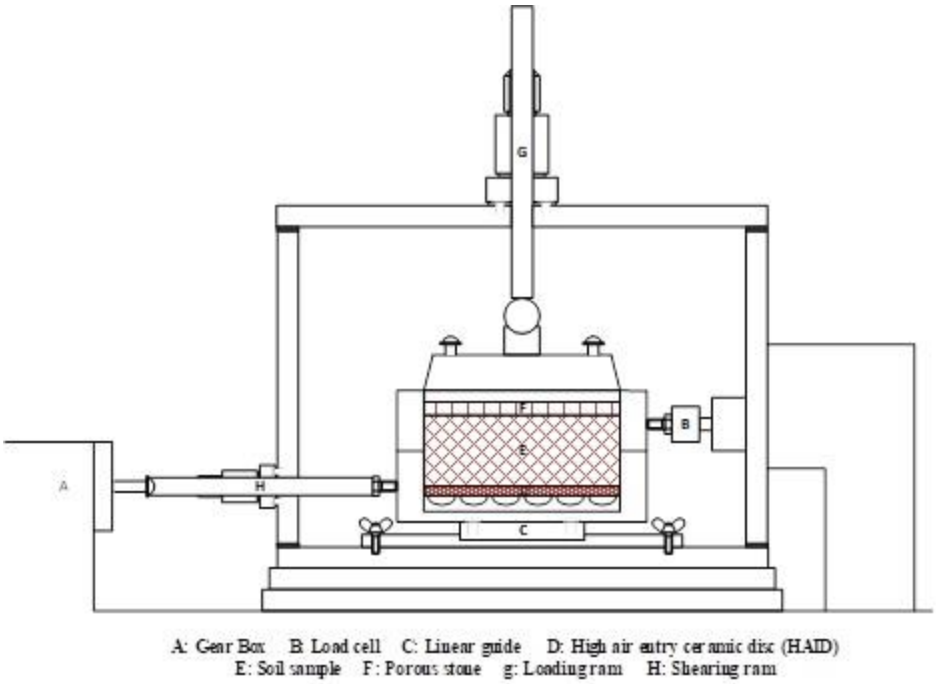

Figure 5.4 Suction-controlled direct shear tests apparatus.

In a typical suction-controlled direct shear test, the soil specimen was required to be saturated in the direct shear chamber first as presented in Gan et al. (1988). Then, the specimen was conditioned to different target suction levels through the axis-translation technique. After this, the direct shear test could be performed. Using the failure plane defined by Equation 5.1 as an example, Figure 5.4a shows the stress paths of unsaturated soils during suction-controlled direct shear testing. Point A represents a soil specimen with zero all-around stress and suction of s_1 at the start of a direct shear test. The application of the normal stress, σ_n, caused the stress state to move from A to B on the σ - s plane at a constant suction of s_1. Then, the direct shear load was applied which caused the movement of stress state from B to C and continuous increase of the Mohr Circle diameter until touched the failure plane at F_1 as shown in Figure 5.4a. The failure plane is tangential to the Mohr Circle at the suction of s_1. However, only point F_1 is not sufficient to define a plane. At least two more direct shear tests for soils with different suction (s_2 and s_3)

and normal stress (σ_{n2} and σ_{n3}) levels are required to be performed to define the failure plane. With these tests, the corresponding failure points F_2, and F_3 can then be determined. To increase the accuracy of the shear strength parameters (i.e. c', ϕ', and ϕ^b), more direct shear tests are encouraged to be performed. With these test results, a linear regression can be easily performed to find the best combination of the shear strength parameters through best-fit the failure points with a plane represented by Equation 5.1. Once the failure plane is defined (i.e., specified c', ϕ', and ϕ^b), the shear strength of the unsaturated soil at any combination of stress and suction can be predicted using Equation 5.1. The above process is straightforward. However, suction controlled tests are drained tests. As mentioned previously, due to the extremely low permeability of unsaturated soils, suction-controlled tests could be time-consuming.

Constant Water Content Direct Shear Test

For a constant water content direct shear test, before shearing, the soil specimens were conditioned to different water content levels (i.e., suction levels). Different from the suction-controlled direct shear test, the suction of an unsaturated soil during constant water content test is continuously changing with normal and shear load application. Using the failure plane defined by Equation 5.1 as an example, Figure 5.4b shows the stress paths during constant water content direct shearing testing. Point A represents a soil specimen with zero all-around stress and suction of s_0 at the initial conditions. The application of the normal stress, σ_n, caused the movement of stress state from A to B on the σ - s plane during which the soil suction decreased from s_0 to s_1. Then, the direct shear load was applied, which caused the continuous movement of stress state from B to C and then to F_1 at the constant normal stress of σ_n. Meanwhile, the Mohr Circle diameter continuously increased until touched the failure plane at F_1 as shown in Figure 5.4b. Different from the suction-controlled direct shear test, the soil suction continuously varied from

s_1 to s_2 and then to s_{1F} during shear loading. With the results from more direct shear tests at different soil suction (s_{2F} and s_{3F}) and normal stress levels (σ_{n2} and σ_{n3}), more failure points such as F_2 and F_3 can be obtained. Then, the shear strength parameters can then be determined through the best-fit linear regression on Equation 5.1. As discussed above, the principle for unsaturated soil strength measurement using the constant water content direct shear test is very simple. However, till now, the constant water content direct shear test has never been reported to characterize unsaturated soil shear strength due to lack of a proper sensor for soil suction measurement during shearing.

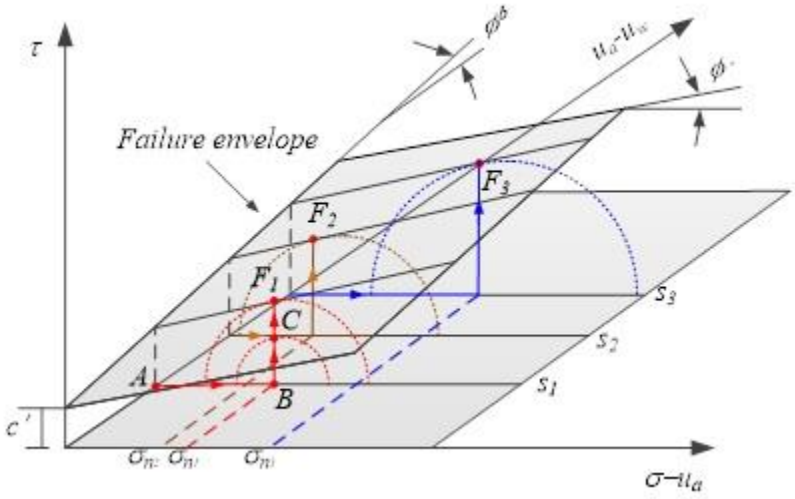

(a) Suction-controlled direct shear test

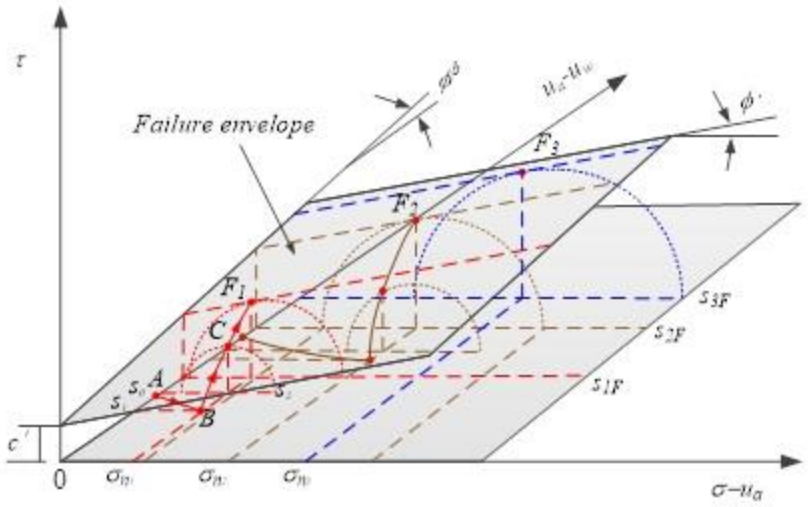

(b) Constant water content direct shear test

Figure 5.5 Stress paths for direct shear tests on unsaturated soils.

5.4 A Miniature High-Suction Tensiometer

The high-suction tensiometer used in the oedometer cell was too big for the direct shear cell. As a result, a miniature high-suction tensiometer was developed as shown in Figure 5.5a. This high-suction tensiometer comprised (1) a miniature EPB-PW pressure transducer for pressure measurement, (2) a 15 Bar high air-entry disc (6.5 mm in diameter and 1 mm in thickness) as a filter to prevent the tensiometer from cavitation at low pressures (< -100 kPa), and (3) a water reservoir to facilitate the generation of a negative water pressure which is detected by the pressure transducer. For the developed miniature high-suction tensiometer, the clearance between transducer diaphragm and ceramic disk, where the water reservoir was located, was approximately 0.1 mm. Figure 5.5b shows a picture of the miniature high-suction tensiometer developed in this project. After fabrication, the miniature high-suction tensiometer was saturated in a triaxial chamber through repeatedly applied water pressure of 600 kPa. The first saturation usually takes time (approximately a week for the tensiometer developed). The time for first saturation can be reduced by applying a higher chamber pressure and more

pressurizing cycles. In addition, the saturation method using CO2 presented in Acikel and Mancuso (2010) can be used to shorten the saturation process. To prevent any possible damage from impact, the miniature high-suction tensiometer was protected by a silicone rubber grommet as shown in Figure 5.5b. After saturation, the miniature high-suction tensiometer was calibrated in a positive pressure range. Negative pressure range calibration was based on extrapolation, which was also used by Li and Zhang (2014) and Lourenço et al. (2006). The accuracy of the calibration was examined by the water pressure immediately after cavitation, which should be approximate -100 kPa. After calibration, to evaluate tensiometer response time under a pressure change, a loading-unloading process was performed for the saturated tensiometer in the triaxial cell filled with water applying precise pressures. The scanning interval for the used data logger was set to be 2 seconds during data acquisition. Figure 5.5c shows the responses of the high suction tensiometer. It can be seen that the pressure measured by the miniature high-suction tensiometer was consistent with cell pressure variation with no delay, which means the response of the tensiometer was less than 2 seconds or nearly instantaneous. Free evaporation tests as suggested by Guan and Fredlund (1997) were also performed to evaluate the maximum attainable suction of the new miniature high-suction tensiometer. Figure 5.5d shows the response of the tensiometer during the free evaporation test. The maximum attainable suction of the used tensiometer was found to be 1235 kPa. After cavitation, the tensiometer pressure quickly reduced to nearly -100 kPa as shown in Figure 5.5d which verified that the tensiometer calibration was accurate.

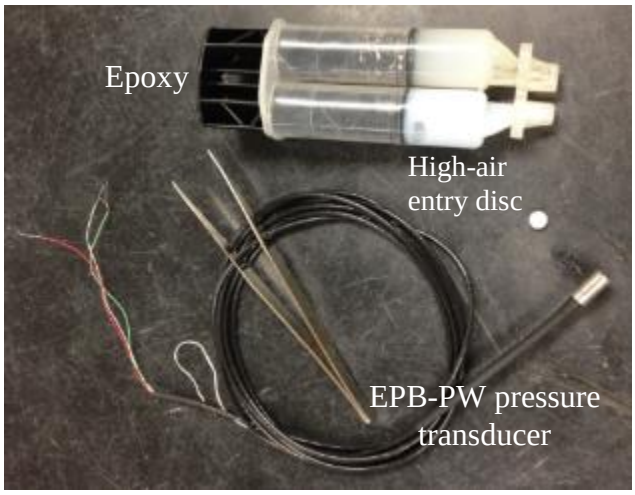

(a) Fabrication

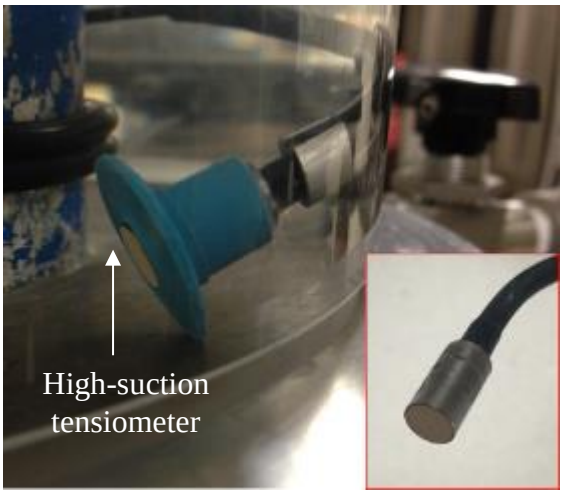

(b) Saturation

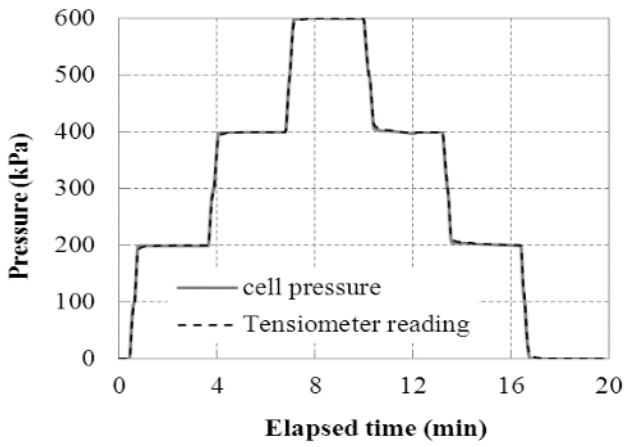

(c) Response time

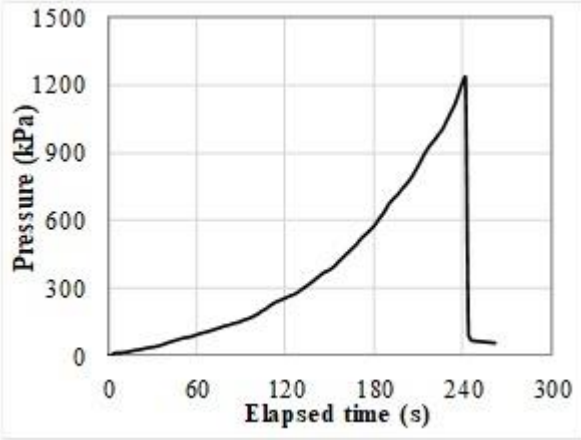

(d) Maximum attainable pressure

Figure 5.6 A miniature high-suction tensiometer.

5.5 Direct Shear Apparatus Modification

In this project, a direct shear cell was modified for a direct shear test on unsaturated soils. As shown in Figure 5.6, this new cell comprised three components: (1) a miniature high-suction tensiometer for soil suction measurement during direct shearing under the undrained condition, (2) a top cap for the application of the normal stress during testing, and (3) two separate stainless steel rings to hold the unsaturated soil specimen and create the shear plane. Figure 5.6 shows a schematic plot of the new cell for the constant water content direct shear test on unsaturated

soils. To achieve more representative soil suction measurement results, the miniature high-suction tensiometer tip should be located on the failure plane. However, for a real direct shear test, the failure plane is usually rough due to the non-uniformity of the soil specimen. As a result, in this new cell, the high-suction tensiometer tip was set to be approximately 1 mm above the failure plane as shown in Figure 5.6a. The miniature high-suction tensiometer tip should not be placed "far" away from the failure plane. Otherwise, the measured soil suction would be less representative. The presence of the spring ensured good contact between the soil and the high-suction tensiometer. This new cell was designed to accommodate the conventional direct shear cell. To characterize the shear strength properties of unsaturated soils, this new cell was placed in the conventional direct shear cell as shown in Figure 5.6b. With this new cell, the conventional direct shear test apparatus could then be performed.

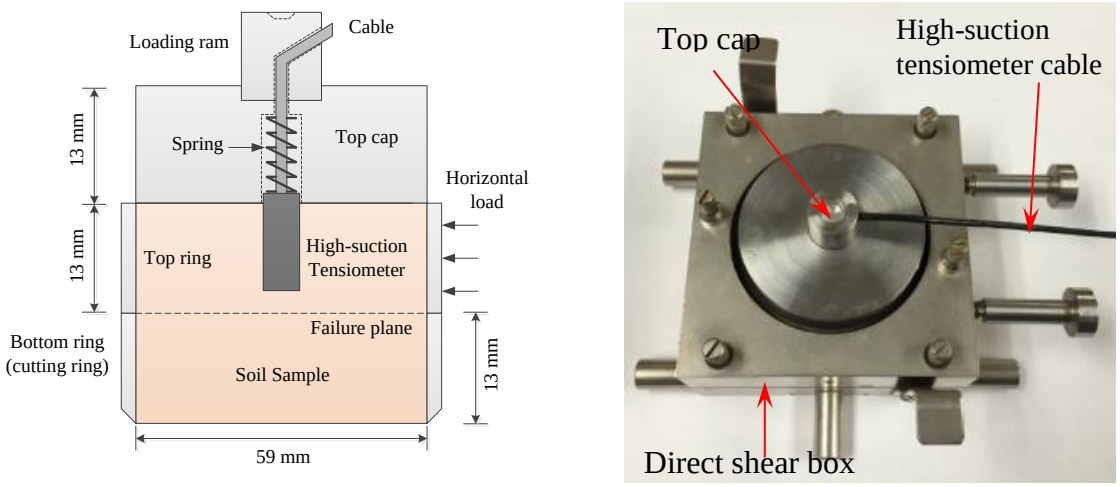

(a) Schematic design (b) New cell in a direct shear box

Figure 5.7 A new constant water content direct shear test apparatus.

CHAPTER 6: EXPERIMENTAL PROGRAM AND RESULTS

6.1 Introduction

As mentioned earlier, half of the soil samples were tested at MST, and the other half were tested in UHM (Detailed description for UHM testing program and results can be found at Iwamoto, 2018). The MST team used the modified oedometer and direct shear test apparatuses discussed in the previous chapter to perform constant water content testing for the unsaturated soils. The team at UHM ran isotropic compression and constant water content triaxial tests. The results from each team were used to simultaneously and independently calibrate the BBM parameters. Later, the calibrated parameters from both approaches were calibrated and discussed.

6.2 MST Team

Soil Sampling

The samples were stored in metal or plastic tubes as shown in Figure 6.1. The original soil samples were not in good shape especially at both ends as typically shown in Figure 6.1. Before testing, the samples were extracted using a hydraulic extruder. To minimize the disturbance during extraction, the soil specimens were directly extracted to the rings for oedometer compression and direct shear test as shown in Figures 6.2a and 6.2b. Next, the soil specimen was cut off from the tube as shown in Figure 6.2c. No obvious disturbance on the sample surface was observed after this extraction. Figure 6.2d shows a picture of the soil specimen in the ring before the oedometer compression or direct shear test. After extraction, the soil specimens were stored in air-tight plastic bags for suction equilibrium or conditioning. The soil specimens were conditioned to different moisture contents by controlling the number of

exposures to the atmosphere for about 15 min/day. Finally, the soil specimens were sealed in plastic bags and stored in a moist room for at least one week to ensure suction equilibrium in the entire specimen.

Oedometer Test

After suction equilibrium in the unsaturated soil specimen, the constant water content oedometer test was then performed. Before testing, the weights of the oedometer compression ring and the soil specimen inside, as shown in Figure 6.2d, were accurately determined. Then, the saturated high-suction tensiometer was mounted to the oedometer cell base. To avoid cavitation during test preparation, the porous ceramic disc of the tensiometer was covered with a thin layer of kaolin paste, which was recommended by other researchers (e.g. Ridley, 2002 and Le et al., 2011). The unsaturated soil specimen was mounted to the cell base after tensiometer installation. Due to the self-weight of the upper part of the modified oedometer and the soil specimen, good contact between the tensiometer and the bottom surface of the specimen was established. The system setup for the one-dimensional oedometer compression test is shown in Figure 6.3. The loading device is exactly the same as the conventional oedometer. Since the testing process for the one-dimensional oedometer compression test lasted several hours, water evaporation during testing is critical. After system assembling as shown in Figure 6.3, vacuum grease was smeared to the places needed to avoid water evaporation during testing. Also, an O-ring was placed around the loading piston to prevent water evaporation from the top surface of the specimen. Then, the displacement transducer and tensiometer used were connected to a Datalogger. A computer was required to monitor the soil volume and suction change during testing as shown in Figure 6.3.

Figure 6.1 Soil samples.

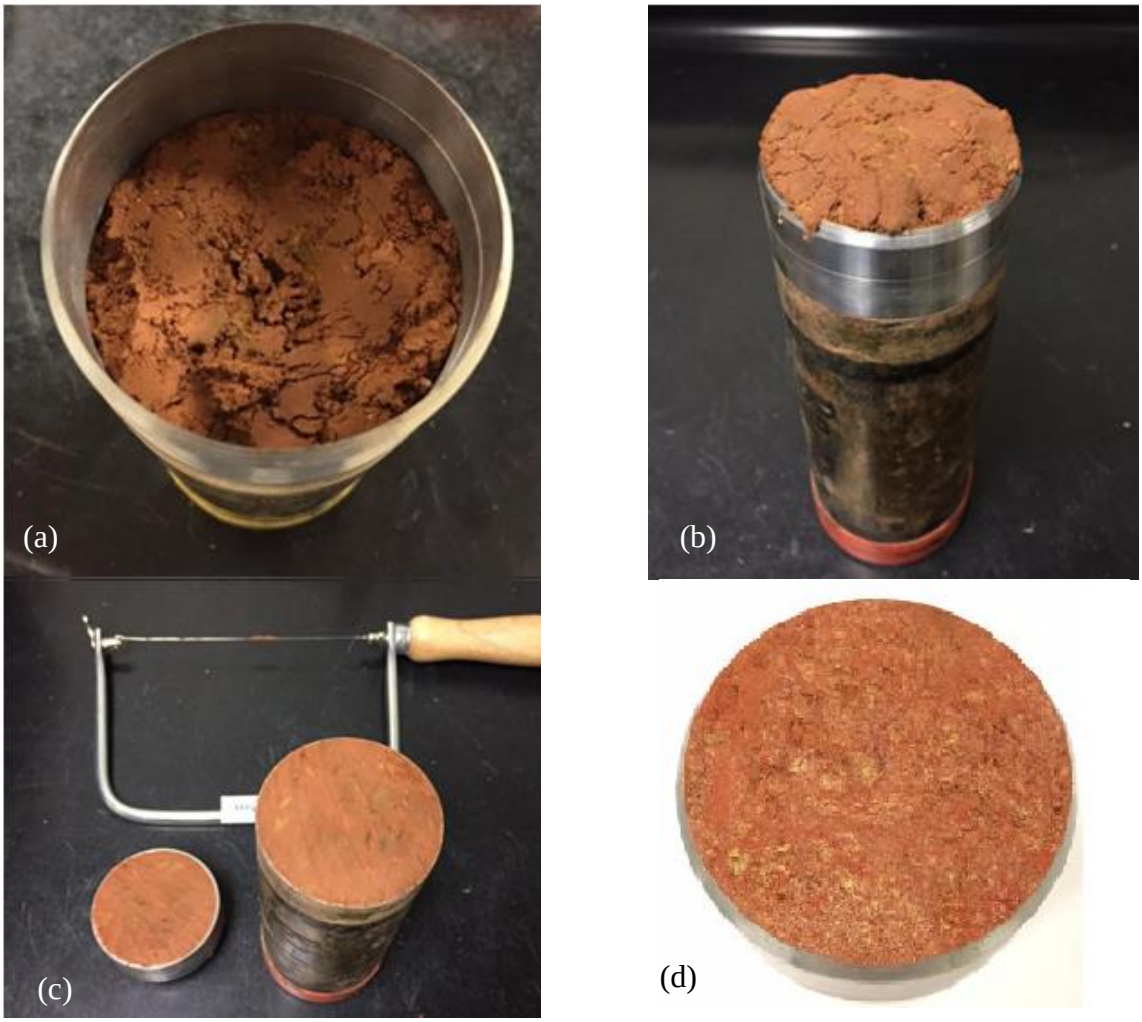

Figure 6.2 Sampling process.

Usually, before loading, several minutes were required for the high-suction tensiometer readings to reach equilibrium. Then, the vertical load was applied to the unsaturated soil

specimen through deadweight come with the oedometer compression system. After each loading step, the applied vertical stress was maintained to be constant for a certain time. This is because the matric suction in the soil specimen would change due to the applied load and this suction change required some time to reach a new equilibrium (Le et al. 2011). The higher the soil suction, the more time required for suction equilibrium (Oliveira and Marinho 2007). The applied vertical stress gently increased or decreased to a target value and followed by another equilibrium period. After reaching equilibrium, the readings of the tensiometer and the local displacement transducer were recorded. In this project, the tested soil specimen was gradually loaded to vertical stress of 800 kPa and then unloaded to 25 kPa. After testing, the weight of the oedometer compression ring, as well as the soil specimen inside after testing, was double-checked to make sure that there was no water loss during testing.

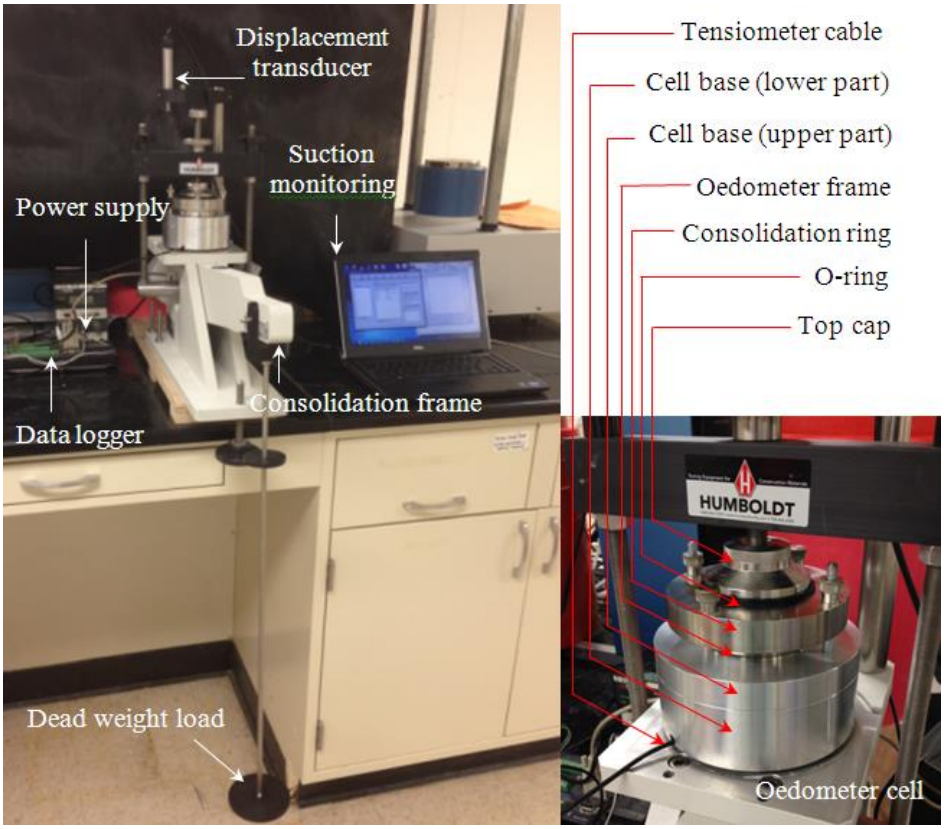

Figure 6.3 One-dimensional oedometer test on an unsaturated soil.

Oedometer Test Results

The matric suction, water content, and specific volume of the tested soil specimens before the oedometer compression test are summarized in Table 6.1.

Table 6.1 Summary of specimens' initial conditions for oedometer tests

Water content	v=1+e	Initial suction (kPa) at 25 kPa normal load
35.81%	2.28	386.3
46.04%	2.485	56.3
34.23%	2.145	136.4
29.84%	2.081	325.7
33.56%	2.116	106.5
30.09%	2.026	224.9
26.19%	2.085	353.6
34.64%	2.153	98.2

For the constant water content oedometer tests, matric suction and vertical displacement were recorded during testing using the high-suction tensiometer and the local displacement transducer, respectively. In this project, soil suctions after equalizations were used as the representative suctions for soil at different loading steps. Based on soil displacement at different loading steps, soil volumes at different loading steps were calculated. Figures 6.4a and 6.4b presented the soil volume and suction variations at different loading steps, respectively. Detailed oedometer compression test results are summarized in Appendix A.

As can be seen in Figure 6.4a, soil volume decreased with increasing vertical stress. This volume decrease had a mild slope until reaching specific stress (i.e., pre-consolidation stress) then the slope became stepper indicating a virgin compression line. During unloading, soil volume increased with a decreasing vertical load. This kind of behavior could be attributed to the elastoplastic behavior of unsaturated soils. When comparing the soil volume at vertical stress of 25 kPa at loading and unloading stages, it could be found the unsaturated soil specimens experienced a significant volume decrease as shown in Figure 6.3a. During vertical testing, as can be seen in Figure 6.3b, soil suction decreased with the increase of vertical stress. It is clear from Figure 6.3 that both matric suction and specific volume simultaneously decreased as the normal stress increased. During unloading, soil suction increased with decreasing vertical stress. However, soil suction was not fully recovered at 25 kPa after unloading due to the plastic volumetric deformation.

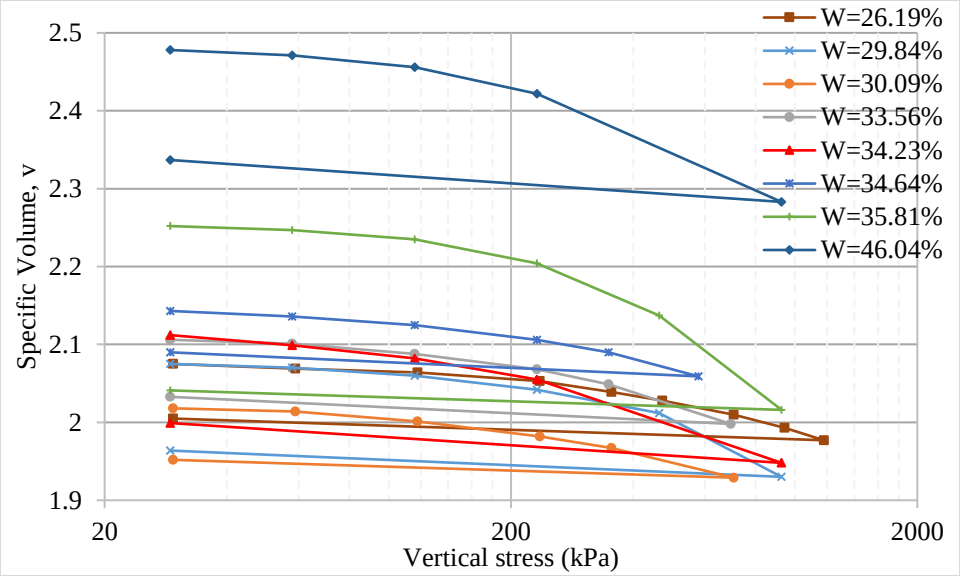

(a)

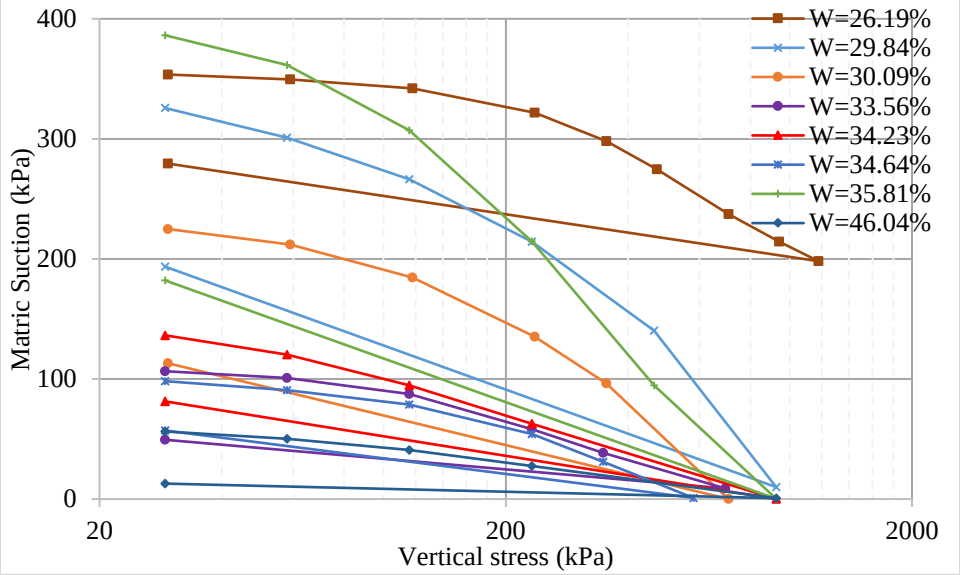

(b)

Figure 6.4 Soil volume and suction changes versus applied vertical stress during oedometer testing.

Direct Shear Test

After conditioning, the specimens were then used for the direct shear test. The rings for the direct shear test, as shown in Figure 6.5a, were 59 mm in diameter and 26 mm in height. Also, the saturated miniature high-suction tensiometer was assembled with the top cap as shown

in Figure 6.5b. Before the installation of the high-suction tensiometer, a 6.5 mm in diameter and 12 mm in depth hole was required to be made at the center of the specimen as shown in Figure 6.5c. To prevent tensiometer cavitation during installation and maintain good contact between the high-suction tensiometer and the soil, similar to the oedometer compression test, a thin layer of saturated kaolin was also smeared on the surface of the ceramic disk. The analysis of shear strength data would not be complete without the volume change behavior during testing. In this direct shear test, the soil volume change was monitored through a linear variable differential transformer (LVDT) mounted at the top of the soil as shown in Figure 6.5d. After installation of soil specimen, high suction tensiometer, and LVDT, deadweight was placed on the yoke to apply the normal load on the soil specimen. When the tensiometer reading stabilized, the direct shear load could then be applied at a constant loading rate of 0.05 mm/min. The shearing process was stopped after the soil specimen reached the failure stage. The soil specimen after the direct shear test was then used for moisture content measurement. Figure 6.5e shows a soil specimen after the direct shear test. It was found that the tensiometer was exactly located the failure plane. In other words, the measured soil suction was representative of the unsaturated soil shear strength characterization.

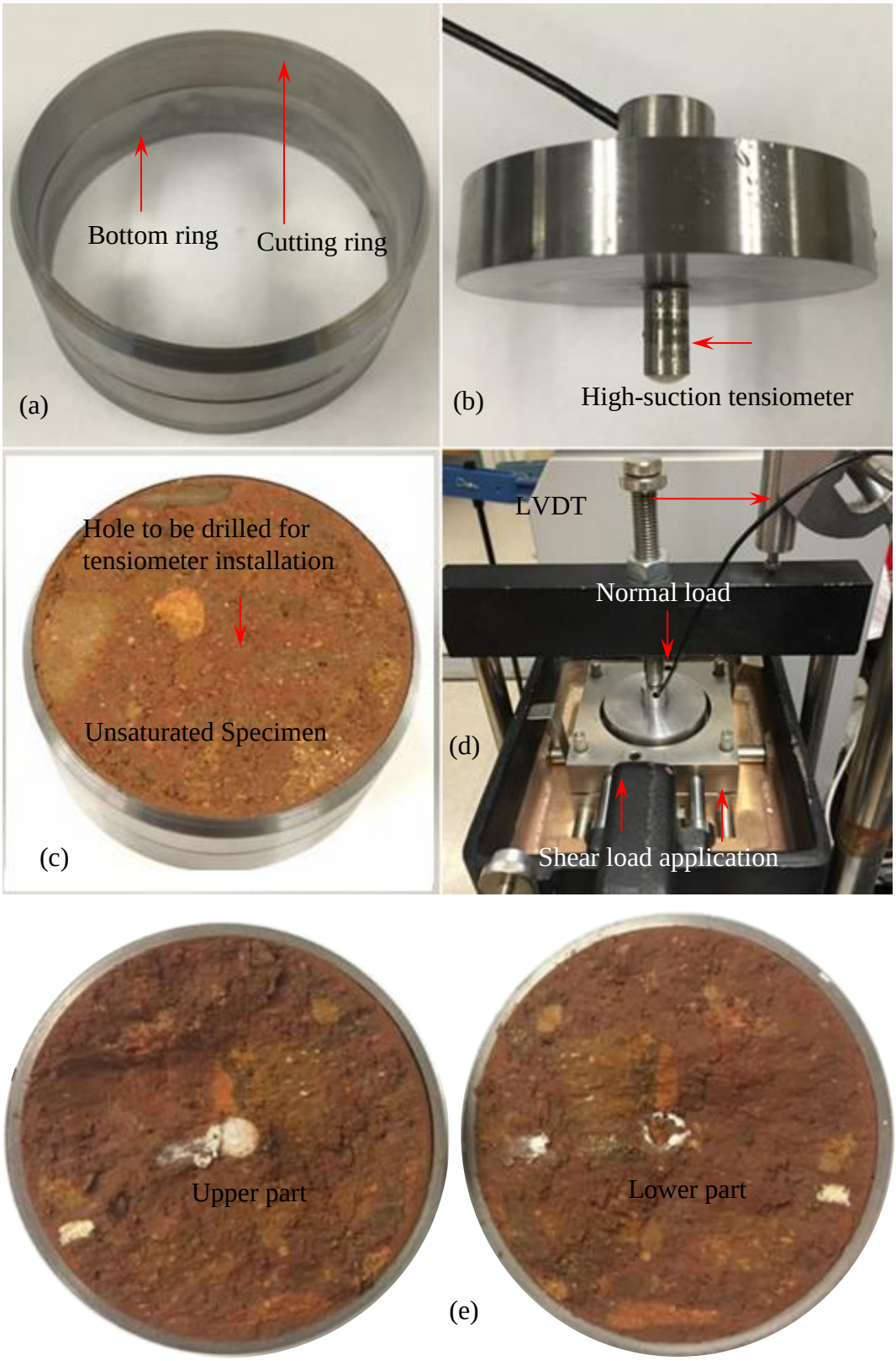

Figure 6.5 Constant water content direct shear test on an unsaturated soil.

Direct Shear Test Results

The soil information before the direct shear test and at-failure during shearing are summarized in Table 6.2. Direct shear test number (3) was excluded from the direct shear test results because of negative suction value. Negative suction value means positive pore water pressure was generated which is not expected for unsaturated soil samples.

Table 6.2 Summary of specimens' initial and final conditions for direct shear tests

Test No.	***Initial condition***			***Final conditions at failure during shearing***		
	W_c	$v=1+e$	*s (kPa)*	*Matric suction (kPa)*	*Shear strength (kPa)*	*Normal stress(kPa)*
1	30.21%	2.191	58.7	235	310	463
2	29.10%	2.209	403	224.70	171.06	139
3	35.81%	2.132	83.4	-7.0	255.96	463
4	38.34%	2.204	428.7	128.9	185.59	236
5	41.38%	2.228	47.9	18.6	80.87	116
6	41.23%	2.235	87	62.60	79.774	58
7	44.23%	2.313	18.9	24.2	173	232
8	32.00%	1.991	649.4	282	356.8	463
9	32.43%	1.973	81.5	84	132.188	116
10	33.72%	2.006	144.4	110.80	99.708	58

During the direct shear test, matric suction and soil volume changes of the tested specimens during testing were recorded using the miniature high-suction tensiometer and the local displacement transducer, respectively. Detailed direct shear test results are summarized in Appendix B. The shear stress variations in the soil specimens with different water contents during loading under different normal stresses are presented in Figure 6.6. It is clear that as the horizontal displacement increased, the shear stress increased until a peak was reached and then stabilized or decreased. It could be found that the ultimate shear stresses generally increased with increasing normal stress. Besides the shear stress, soil suction, and volume variations versus

horizontal displacement during shearing were also extracted and presented in Figures 6.7a and 6.7b, respectively.

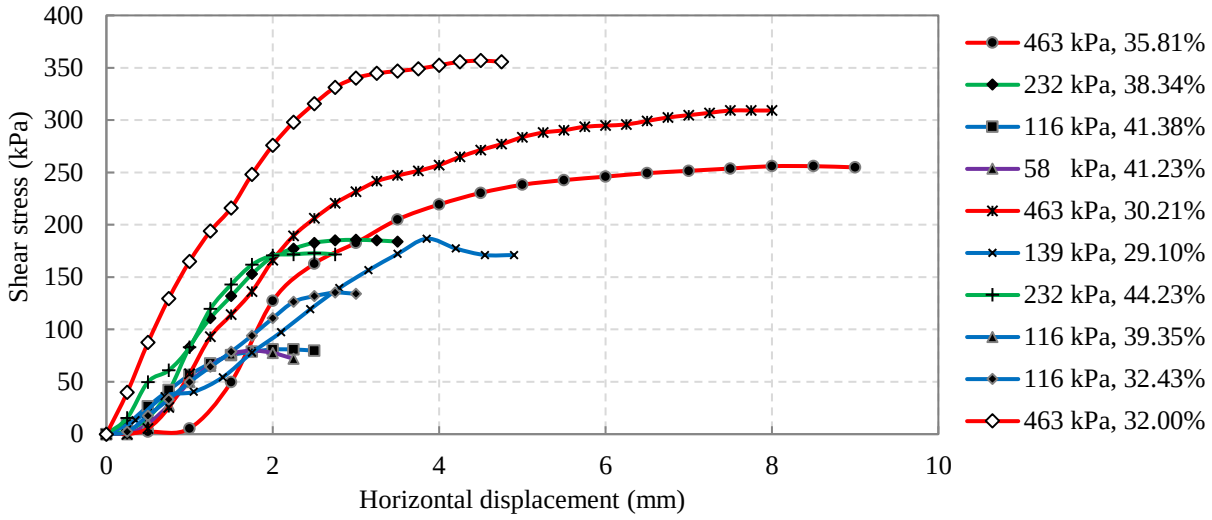

Figure 6.6 Shear stress versus horizontal displacement for samples with different water contents.

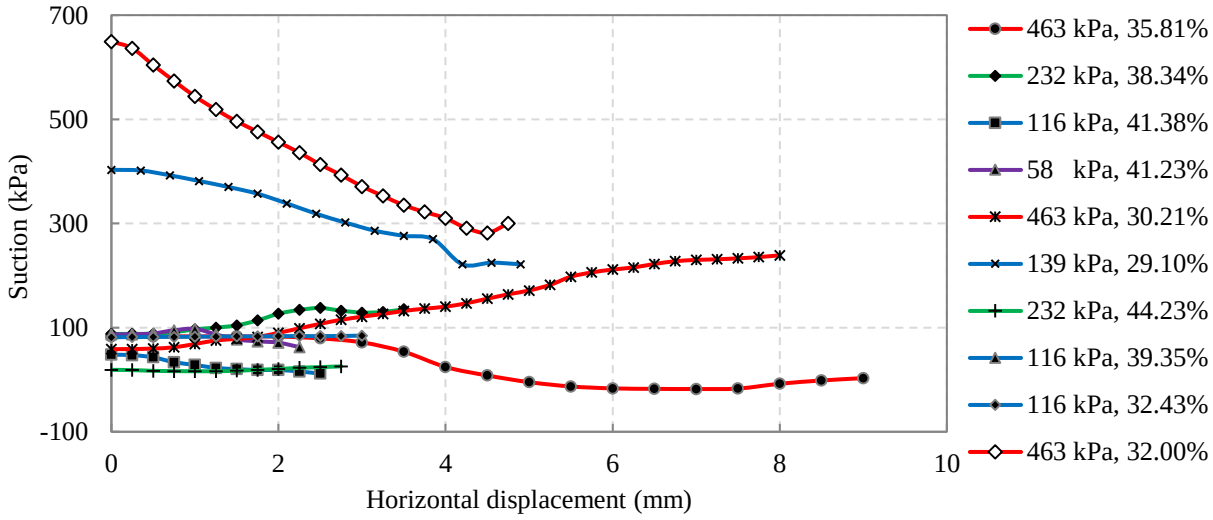

(a)

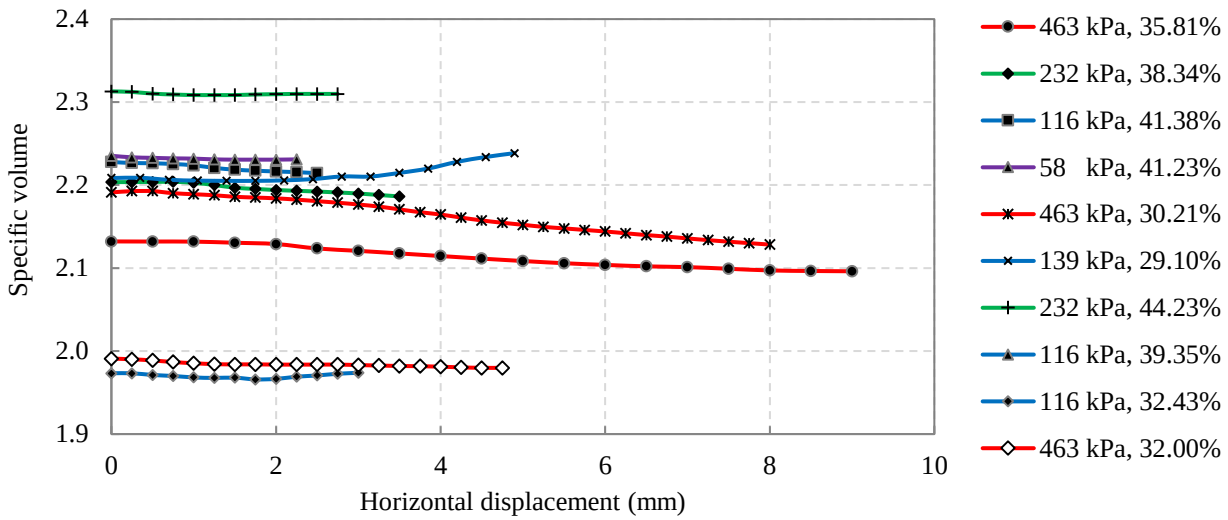

(b)

Figure 6.7 Soil volume and suction variations during testing.

As shown in Figure 6.7a, at high initial soil suction levels, the soil suction usually decreased with increasing shear load/displacement. In contrast, for soil specimens with initial soil suction less than 100 kPa, with increasing shear load/displacement, the soil suctions variations were different under different normal stress and water content conditions. At different normal stress conditions, most of the soil volumes slightly decreased with horizontal displacement indicating a contractive behavior. On the contrary, volumes for specimens with a water content of 29.1% and 32.43 were increased indicating a dilative behavior.

6.3 UHM Team

Approximately half of the soil samples were provided to the University of Hawaii at Manoa for laboratory testing and characterization. Several lab tests were performed at UHM including index testing, saturated consolidation test, saturated triaxial test, SWCC, and hydraulic conductivity tests, and unsaturated triaxial tests. Detailed description and discussion for the

experimental results were provided by Melia K. Iwamoto in her Ph.D. thesis (Iwamoto, 2018). In this section a brief summary of experimental results is provided.

Index Testing

Index tests performed include grain size distribution, Atterberg limits, natural water content, and specific gravity, results of which are summarized as follows.

Grain size Analysis

The grain size distribution curves (Figure 6.8) indicated that the soil is fine-grained.

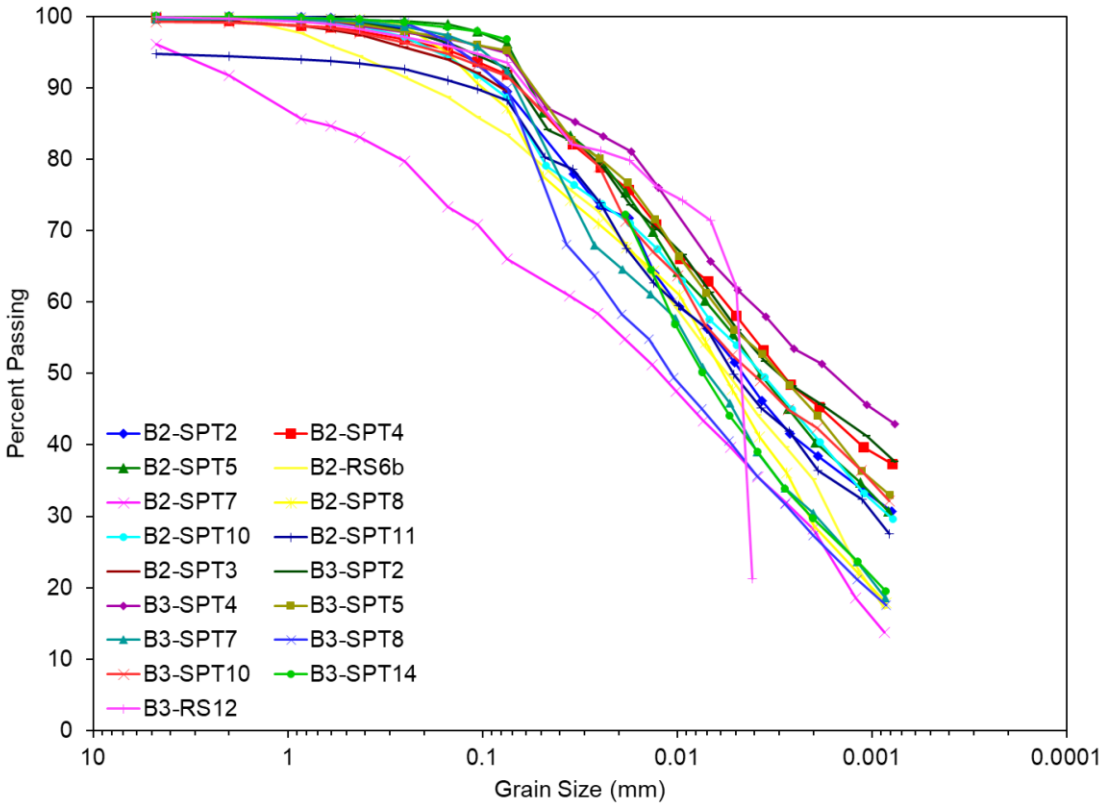

Figure 6.8 Grain size distribution curves (Iwamoto, 2018).

Atterberg Limits and Natural Water Content

Atterberg limits were performed on almost 18 samples from the two boreholes at different depths. When plotted on a plasticity chart, it indicated that the soil is high plasticity silt (MH) based on the Unified Classification System. The natural water contents were also determined for these samples. An average liquidity index ($LI = (w - PL)/PI$) was found to be -0.70 that indicated less sensitive soil, and the soil consistency may be relatively stiff, which agreed with the SPT blow counts. The natural water content was relatively constant with depth and averaged approximately 41%.

Specific Gravity

The soil specific gravity was determined in accordance with ASTM D84-89 using a pycnometer. The average specific gravity was about 2.90 for all the tested samples.

Saturated Consolidation Test

One 1 D consolidation test was conducted on a soil sample (0.30 to 0.76 m) in its saturated state to estimate the saturated permeability, preconsolidation pressure, and compressibility parameters. Results indicated that the soil has a preconsolidation pressure of 160 kPa corresponding to an over-consolidation ratio (OCR) of 2.0. The coefficient of vertical consolidation (c_v) was estimated using both Taylor (1948) and Casagrande and Fadum's 1940 methods. The soil saturated hydraulic conductivity was back-calculated from c_v and was about 10e-6 cm/s.

Multi-Stage Consolidated Drained Triaxial Test on Saturated Sample

Due to the limited number of samples, multi-stage consolidated drained triaxial test was performed on one sample to obtain the saturated shear strength parameters. The sample was first

saturated by increasing the confining pressure until a B-value (Skempton's pore pressure parameter) of 0.98 was reached. The confining pressure was then increased to 15 kPa, 30 kPa, and 50 kPa, and the sample was sheared at each confining pressure in a drained fashion. At confining stresses of 15 and 30 kPa, the axial strain was limited to 2.5% before increasing the confining stress to the next stage. At the last stage (50 kPa), the sample was sheared until failure. Figure 6.9 shows the multistage triaxial test results.

Since the sample was consolidated to 3 different values of confining stress prior shearing, this implies that the OCRs are different at each confining stress. Therefore, Hvorslev (1937) shear strength theory was utilized to identify meaningful shear strength parameters for the soil. The calibrated shear strength parameters for this soil are shown in Table 6.3. Based on the saturated water content for the soil in field that was 46.5%, shear strength parameters of 28^{o} and 18 kPa could be recommended for the angle of internal friction and cohesion respectively.

Table 6.3 Summary of calibrated shear strength at different confining stress.

Confining stress (kPa)	**Void ratio, e**	**Water content (%)**	**Angle of internal friction, ϕ' (degree)**	**Cohesion, c' (kPa)**
15	1.345	46.5	28	19.2
30	1.343	46.4	8	22.4
50	1.341	46.3	28	25.1

Soil-Water Characteristic Curve and Hydraulic Conductivity Function For Unsaturated State

The soil-water characteristic curve (SWCC) was estimated by running a pressure plate (PP) test and Decagon Devices' Aqua Lab Vapor Sorption Analyzer (VSA). The Pressure plate apparatus was used to test a specimen obtained from a modified California sampler to determine the SWCC at low suction levels (0 to 500 kPa). The VSA was used to extend the SWCC to

higher suction levels (6,000 to 600,000 kPa). Unlike the PP, the sample used for VSA doesn't have to be undisturbed. Wetting and drying cycles were considered in the pressure plate test. Figure 6.10 shows the SWCC results from both PP and VSA. It worth notice that the SWCC is pressure dependent and the curves are shown in Figure 6.10 were tested under very low pressure and are valid only for surficial layers.

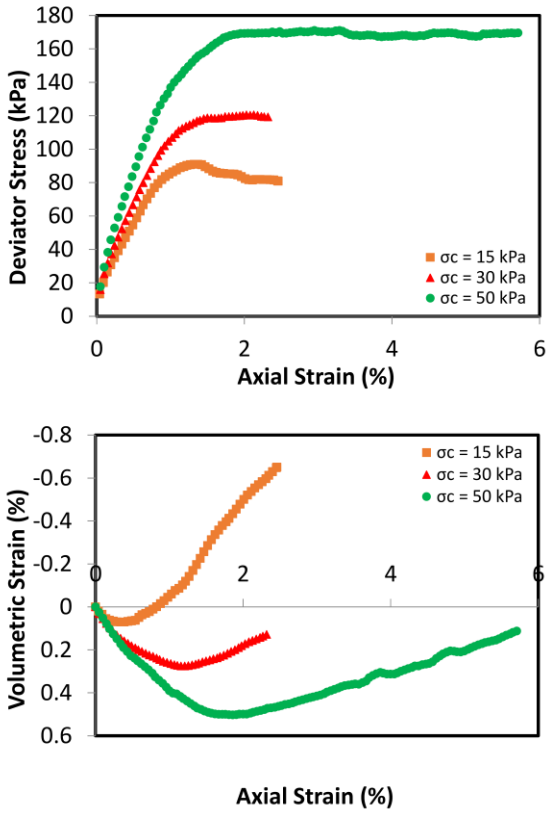

Figure 6.9 Multi-stage triaxial test results: (a) deviator stress vs axial strain and (b) volume strain vs axial strain curves (Iwamoto, 2018).

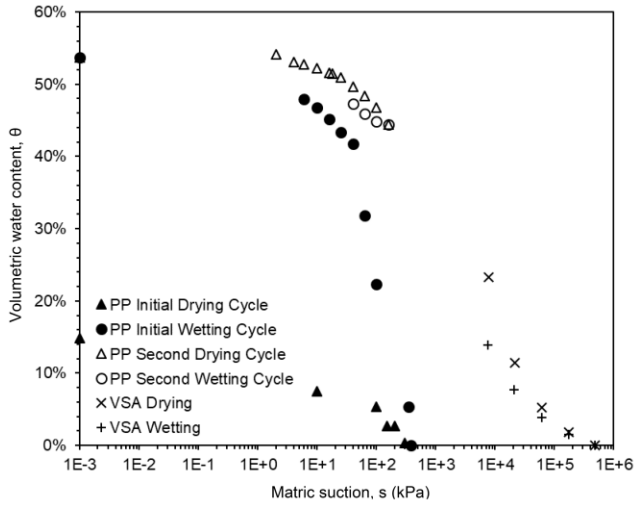

Figure 6.10 Laboratory measured the soil-water characteristic curve (Iwamoto, 2018).

It is well known that the unsaturated soil permeability significantly decreases with decreasing saturation degree. Measuring the unsaturated soil permeability at different degrees of saturation is a very laborious and time-consuming proposition. The variation of unsaturated soil permeability with suction, known as hydraulic conductivity function (HCF), can be alternatively obtained using the SWCC data together with a statistical approach proposed by Kunze et al. (1968). The resulting HCF is shown in Figure 6.11 in terms of relative permeability as a function of suction. The relative permeability defined as the permeability at a given degree of saturation divided by the saturation permeability.

Constant Water Content Isotropic Compression Test for Unsaturated Soils

Triaxial tests were performed on three unsaturated soil samples extruded from modified California sampler using a GDS automated system. The used GDS equipment uses a Hong Kong University of Science and Technology (HKUST) double wall system to measure the unsaturated soil volume change (for more details about the system refer to Ng et al., 2007). Figure 6.12 shows a schematic plot for the HKUST double wall system.

Each sample was subjected to constant water content isotropic compression (CWIC) up to targeted stress value, then a constant water content shear (CWS) was applied up to failure. Table 6.4 shows the initial conditions for each of the three samples used for CWIC test. Figure 6.13 shows the obtained test results for the three samples.

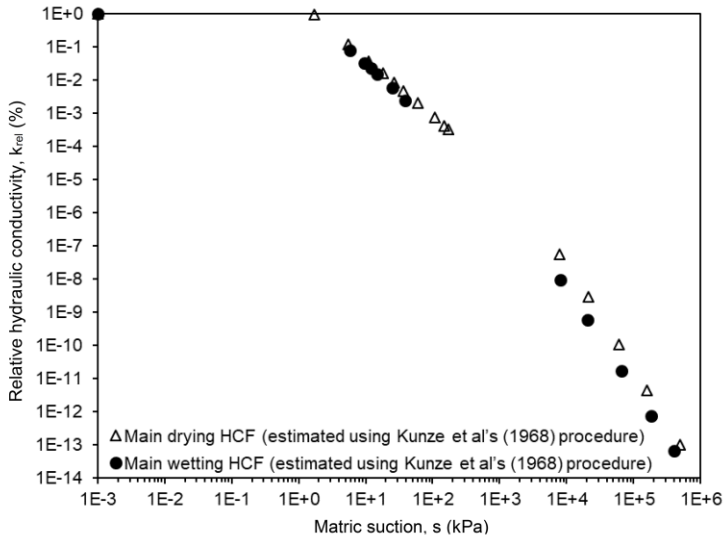

Figure 6.11 Hydraulic conductivity function derived from SWCC (Iwamoto, 2018).

Table 6.4 Initial specimen conditions for the CWIC samples.

Test	Sample	D_0 (mm)	H_0 (mm)	S_0 (kPa)	e_0	S_0	Water content (%)
CWIC-1	B3-1-B	58.35	136.90	15.70	1.286	86.0%	34.4%
CWIC-2	B3-6-M	61.13	127.70	25.70	1.365	91.5%	44.3%
CWIC-3	B3-3-M	61.00	126.70	42.90	1.348	89.7%	43.7%

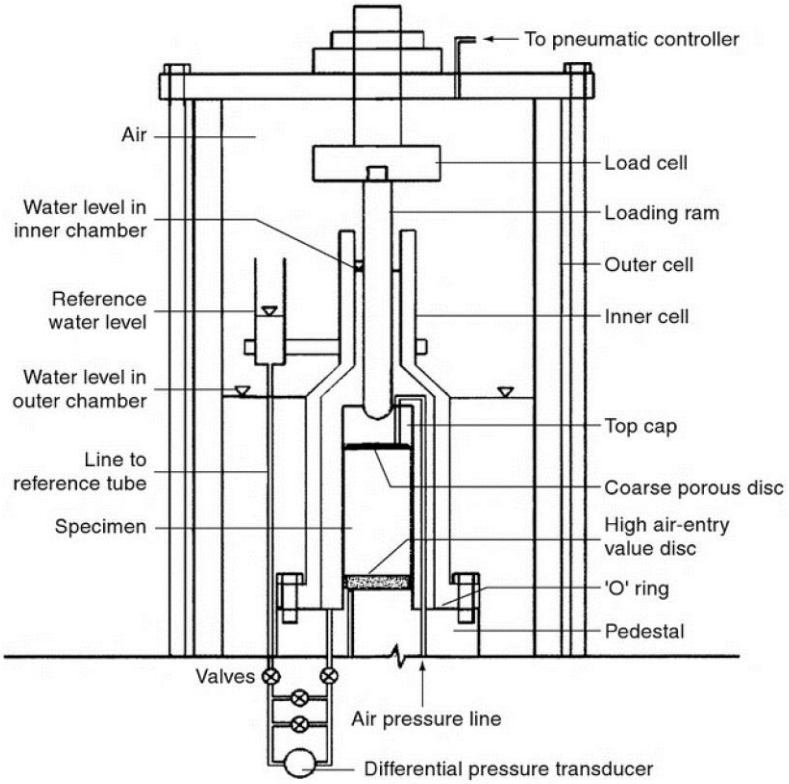

Figure 6.12 Schematic plot for the HKUST double-wall volume change system (From Ng et al., 2007).

Constant Water Content Triaxial Shear Test for Unsaturated Soils

Constant water content triaxial test have been performed by several researchers (Bishop et al., 1960; Bishop and Donald, 1961; Satija, 1978; Georgetti and Vilar, 2011; Ma et al., 2013; Rahardjo et al., 2004; Thu et al., 2006b). Rahardjo et al. (2004) performed consolidated drained and constant water content triaxial shear tests on reconstituted residual silt and found that shear strength obtained both tests show good agreement. Georgetti and Vilar (2011) observed that CWC deviator stress-strain curves more closely resembled saturated CD deviator stress-strain curves than those obtained from saturated CU triaxial shear tests. Table 6.5 shows the initial conditions for each sample before testing.

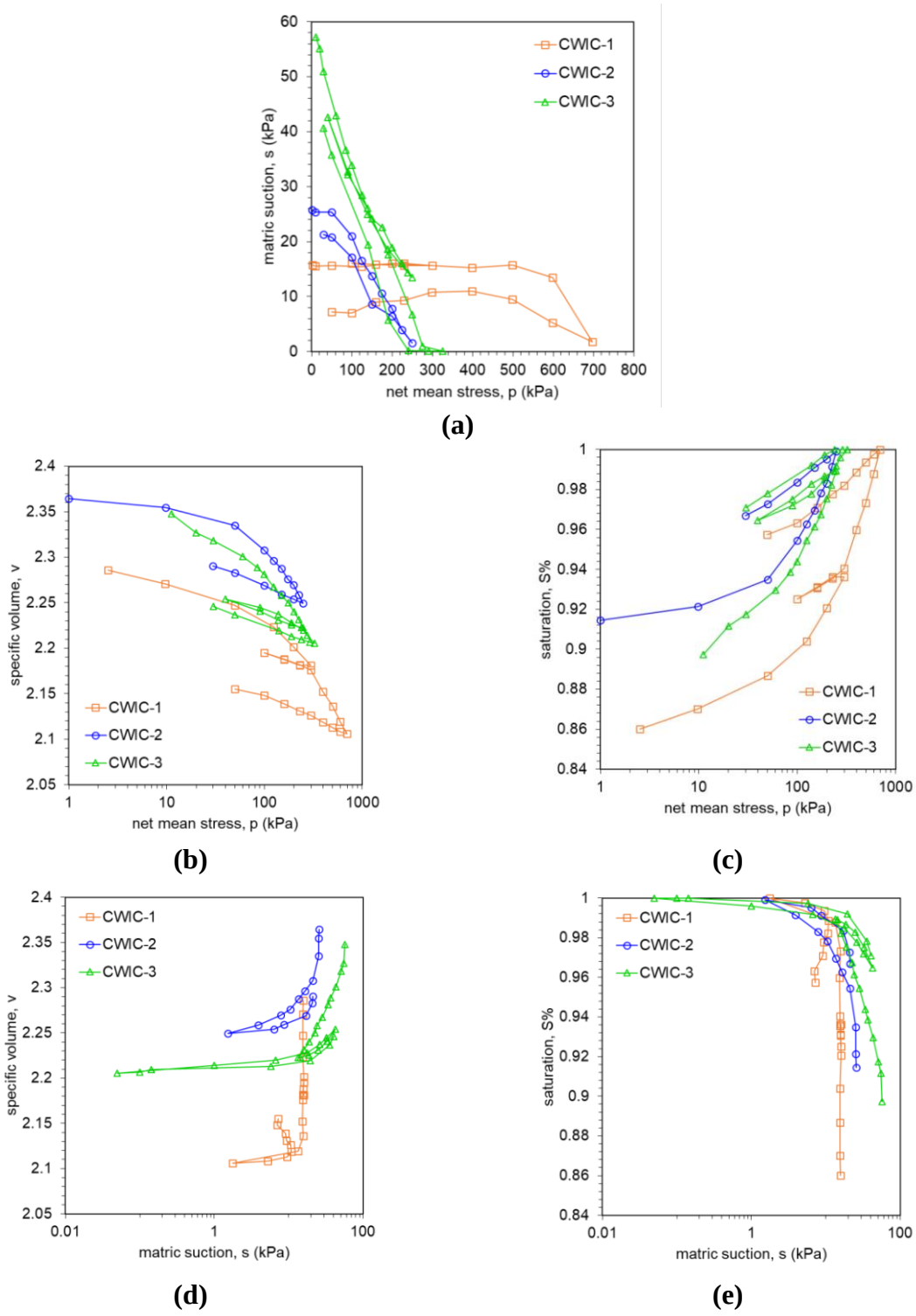

Figure 6.13 Constant water content compression test results of (a) measured stress paths, (b) specific volume vs net mean stress, (c) saturation vs net mean stress, (d) specific volume vs matric suction, and (e) saturation degree vs matric suction (Iwamoto, 2018).

The triaxial shear test results for unsaturated soils were compared with that of saturated soils to investigate the effect of suction on the shear strength of soils. Table 6.6 summarizes the results of the CWC tests. Deviatoric stress versus axial strain plots are shown in Figure 6.14a. All tests exhibited post-peak strain softening. The peak deviatoric stress for tests 1, 2, and 3 were 411 kPa, 236 kPa, and 269 kPa at axial strains of 2.6%, 6.2%, and 3.29%, respectively. For saturated and unsaturated tests conducted at the same confining stress, the peak deviatoric stress increased with increasing suction.

The samples were loaded to large strains to reach the critical state. The critical state deviatoric stress for CWC tests 1, 2, and 3 were 142 kPa, 163 kPa, and 134.5 kPa at axial strains of 13.3%, 17.4%, and 21.2%, respectively. For saturated and unsaturated tests conducted at the same confining stress of 50 kPa, the deviatoric stress at critical state decreased with increasing suction. This indicates that one or both of the tests have not yet reached critical state. Volume change curves are shown in Figure 6.14b. For unsaturated CWC tests, the amount of dilation increased with increasing suction and OCR. Suction versus axial strain curves are shown in Figure 6.14c. Suctions did not change significantly during shearing. The maximum suction difference during tests 1, 2, and 3 were 3.5 kPa, 1.3 kPa, and 6.9 kPa, respectively. The suction response during shear was different for all tests. During CWC-1, suctions initially increased to a peak of 45.1 kPa then decreased until the peak deviator stress was reached. The suction then gradually increased for the remainder of the test. During test CWC-2, there was no significant change in suction during shear despite there being two unload-reload cycles. During test CWC-3, the suction initially decreased during shear and increased during the unload-reload cycle. During reloading, the suction decreased until the peak deviatoric stress was reached and then gradually increased for the remainder of the test. Thu et al. (2006b) performed constant water content and

drained triaxial shear tests on an MH Malaysian silt and found that the suction response decreased as the initial suction value decreased. Our findings agree well with those results.

Table 6.5 Initial conditions of the specimen before shearing.

Test	Sample	D_0 (mm)	H_0 (mm)	Water content (%)	Preconsolidation pressure (kPa)	S_0 (kPa)	OCR
CWC-1	B3-1-B	57.3	136.6	38.4	50	44	14
CWC-2	B3-6-M	60.2	127.7	44.3	30	21	5
CWC-3	B3-3-M	59.3	125.8	43.7	30	40	11
CD-15	B2-1-B	59.4	124.6	Sat	15	0	6
CD-30	B2-1-B	58.9	126.6	Sat	30	0	3
CD-50	B2-1-B	58.7	128.4	sat	50	0	2

Table 6.6 Triaxial shear test results.

Test	Peak				Critical state			
	p (kPa)	s (kPa)	q (kPa)	ε_a (%)	p (kPa)	s (kPa)	q (kPa)	ε_a (%)
CWC-1	189	42	411	2.6	99	42.6	142	13.3
CWC-2	108	21.5	236	6.2	84	21	163	17.4
CWC-3	120	40	269	3.3	76	42	135.5	21.2
CD-15	45	0	91	1.4	1	1	1	1
CD-30	70	0	120.5	2.1	1	1	1	1
CD-50	135	0	170	5.7	106	0	170	5.7

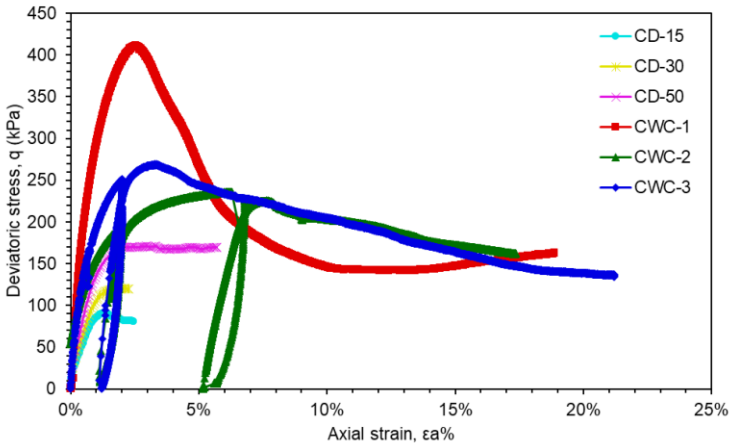

(a)

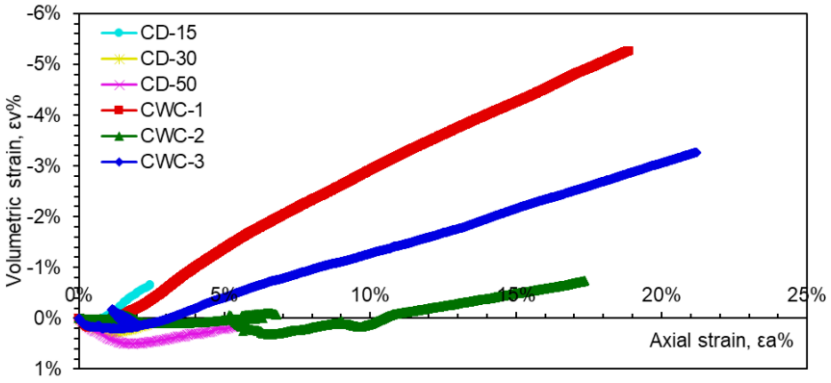

(b)

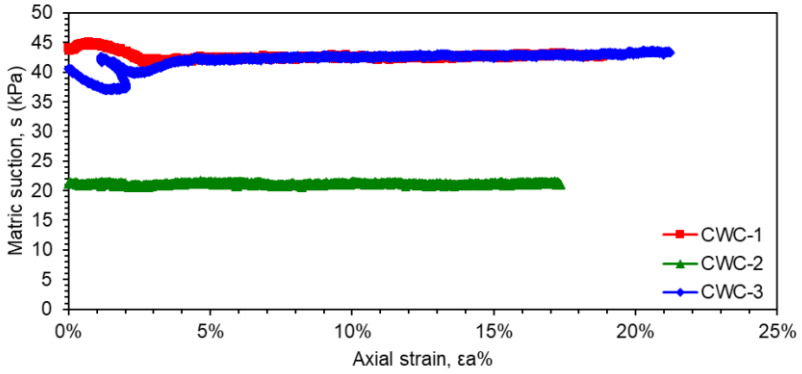

(c)

Figure 6.14 Constant water content triaxial test results of (a) deviatoric stress vs axial strain, (b) volumetric vs axial strain, and (c) matric suction vs axial strain (Iwamoto, 2018).

CHAPTER 7: MECHANICAL CONSTITUTIVE MODEL

7.1 Introduction

In this chapter two approaches were used independently to calibrate the BBM parameter. The first approach was proposed by the MST team using the constant water content oedometer and direct shear test results. The second approach, however, was followed by the UHM team using the constant water content isotropic and triaxial shear test results (Iwamoto, 2018). These two approaches are demonstrated in detail. Later, the calibrated model parameters are compared and critically discussed.

7.2 MST Team

Introduction

Zhang et al. (2016a) derived an explicit formulation for the at-rest coefficient of earth pressure, K0, based on the basic definition of the at-rest condition without any assumptions. In addition, a procedure was provided to calibrate the BBM parameters under triaxial stress conditions using results from the oedometer test only. Later, the same procedure was used Zhang et al. (2016b) to successfully calibrate the BBM parameters using constant water content oedometer test results. It is worth notice that, since oedometer is not a failure test, Zhang et al. (2016a and 2016b) recommended calibrating the BBM shear strength parameters from a soil failure test (e.g., direct shear test). In the Hawaii project, the procedure described by Zhang et al. (2016a) was used to calibrate BBM stiffness parameters. The BBM strength parameters are calibrated using the constant water content direct shear test results. Procedure and calculation steps are explained in detail in the following sections.

Fredlund's Shear Strength Parameters

The shear strength equation proposed by Fredlund et al. (1978), shown in Equation [7.1], was utilized in this section to study the stress state at failure (i.e., $(\sigma_1 - u_a)_f$, $(\sigma_3 - u_a)_f$, and $s_f = (u_a - u_w)_f$) and to further calibrate saturated and unsaturated strength parameters.

$$\tau_f = \left[c' + (u_a - u_w)_f \tan\phi^b \right] + (\sigma - u_a)_f \tan\phi' \qquad \text{(Eq. 7.1)}$$

Linear regression was performed on the test results to find the best estimation of the shear strength parameters. To find out the suitable combination of shear strength parameters c', ϕ', and ϕ^b, the below procedure could be followed:

(a) Assume arbitrary values for the shear strength parameters (i.e., c', ϕ', and ϕ^b).

(b) Using Equation [7.1], calculate the shear strength based on the assumed values in step (a).

(c) Calculate the square of differences between the measured and predicted shear strength based on the eq. [7.2]. The predicted values and the squared errors are presented in Table 7.1.

$$F(x) = \sum_{i=1}^{n} w_i \left[(\tau_{fm})_i - (\tau_{fp})_i \right]^2 \qquad \text{(Eq. 7.2)}$$

where w_i is a weight factor that is equal to one in this case, τ_{fm} and τ_{fp} is the measured and predicted shear strength respectively.

(d) SOLVER add-in in Microsoft Excel could be used to guess the best-fit parameters to get the minimum error.

Table 7.1 Predicted shear strength and errors.

Initial condition			At failure during shearing			Predicted	Error[2]
W_c (%)	v	s (kPa)	s_f (kPa)	*Shear stress* (kPa)	*Normal stress* (kPa)	*Shear stress* (kPa)	
30.21	2.191	58.7	235	310	463	329.75	390.08
29.10	2.209	403	224.7	171.06	139	169.78	1.64
38.34	2.204	428.7	128.9	185.59	236	188.19	6.75
41.38	2.228	47.9	18.6	80.87	116	97.19	266.35
41.23	2.235	87	62.6	70	58	82.22	149.40
44.23	2.313	18.9	24.2	173	232	155.03	322.80
32.00	1.991	649.4	282	356.8	463	343.76	169.93
32.43	1.973	81.5	84	132.188	116	116.69	240.17
33.72	2.006	144.4	110.8	99.708	58	96.59	9.69
Sum of errors =							1556.81

BBM Shear Strength Parameters

In this section, the BBM shear strength parameters (i.e. *M* and *K*) are calibrated from the constant water content direct shear test results (CWDS). Moreover, derivations are provided to calculate *M* and *K* from the unsaturated soil shear strength properties (i.e. c', ϕ', and ϕ^b) based on *c'*=0.0 which is assumed by the first author of modified Cam-Clay model (Roscoe and Burland 1968) and addressed by Alonso et al., (1990). In the CWDS, the suction at failure was measured using miniature HST equipped in the conventional direct shear cell.

Starting from Fredlund et al. (1978) shear strength Equation [7.1], the suction effect may be considered as a cohesion effect and can be added to the saturated cohesion as follows:

$$\tau_f = \left[c' + \left(u_a - u_w\right)_f \tan\phi^b\right] + \left(\sigma - u_a\right)_f \tan\phi' \qquad \text{(Eq. 7.3)}$$

Denoting both suction and cohesion as C, one has

$$\tau_f = C + \left(\sigma - u_a\right)_f \tan\phi' \qquad \text{(Eq. 7.4)}$$

The soil shear strength can, also, be derived as a function of the major and minor principal stresses as follows:

$$(\sigma_1 - u_a)_f = (\sigma_3 - u_a)_f \tan^2\left[\frac{\pi}{4} + \frac{\phi'}{2}\right] + 2C\tan\left[\frac{\pi}{4} + \frac{\phi'}{2}\right] \quad \text{(Eq. 7.5)}$$

The deviatoric and mean net stresses are defined as follows:

$$q = (\sigma_1 - u_a) - (\sigma_3 - u_a) \quad \text{(Eq. 7.6)}$$

$$p = \frac{(\sigma_1 - u_a) + 2(\sigma_3 - u_a)}{3} \quad \text{(Eq. 7.7)}$$

Rearranging Equations [7.6] and [7.7], one has

$$(\sigma_1 - u_a) = \frac{3p + 2q}{3} = p + \frac{2q}{3} \quad \text{(Eq. 7.8)}$$

$$(\sigma_3 - u_a) = \frac{3p - q}{3} = p - \frac{q}{3} \quad \text{(Eq. 7.9)}$$

Substituting Equations [7.8] and [7.9] into Eq. [7.5],

$$\left(p + \frac{2q}{3}\right)_f = \left(p - \frac{q}{3}\right)_f \tan^2\left[\frac{\pi}{4} + \frac{\phi'}{2}\right] + 2C\tan\left[\frac{\pi}{4} + \frac{\phi'}{2}\right] \quad \text{(Eq. 7.10)}$$

Inserting $C = c' + (u_a - u_w)_f \tan\phi^b$ into Eq. [7.10]

$$\left(p + \frac{2q}{3}\right)_f = \left(p - \frac{q}{3}\right)_f K_p + 2\left[c' + (u_a - u_w)_f \tan\phi^b\right]\sqrt{K_p} \quad \text{(Eq. 7.11)}$$

where $K_p = \tan^2\left[\frac{\pi}{4} + \frac{\phi'}{2}\right]$

Equation [7.11] can be rearranged as follows:

$$q = \frac{3\left(K_p - 1\right)}{2 + K_p} p + \frac{6\left[c' + \left(u_a - u_w\right)_f \tan\phi^b\right]\sqrt{K_p}}{2 + K_p}$$

$$= \frac{3\left(K_p - 1\right)}{2 + K_p} p + \frac{3\left(K_p - 1\right)}{2 + K_p} \frac{2\left[c' + \left(u_a - u_w\right)_f \tan\phi^b\right]\sqrt{K_p}}{K_p - 1}$$

$$= \frac{3\left(K_p - 1\right)}{2 + K_p} \left[p + \frac{2\left[c' + \left(u_a - u_w\right)_f \tan\phi^b\right]\sqrt{K_p}}{K_p - 1} \right] \qquad \text{(Eq. 7.12)}$$

$$= M\left[p + \frac{2\left[c' + \left(u_a - u_w\right)_f \tan\phi^b\right]\sqrt{K_p}}{K_p - 1} \right] = M\left[p + \frac{2\left[c' + \left(u_a - u_w\right)_f \tan\phi^b\right]\sqrt{K_p}}{K_p - 1} \right]$$

$$= M\left[p + \frac{2\tan\phi^b\sqrt{K_p}}{K_p - 1}\left(u_a - u_w\right)_f + \frac{2c'\sqrt{K_p}}{K_p - 1} \right]$$

where $M = \frac{3\left(K_p - 1\right)}{2 + K_p} = \frac{3\left\{\tan^2\left[\frac{\pi}{4} + \frac{\phi'}{2}\right] - 1\right\}}{2 + \tan^2\left[\frac{\pi}{4} + \frac{\phi'}{2}\right]}$. The soil cohesion is assumed to be zero as suggested by Roscoe and Burland (1968). Equation [7.12] can be simplified as follows:

$$q = M\left[p + \frac{2\tan\phi^b\sqrt{K_p}}{K_p - 1}\left(u_a - u_w\right)_f \right] \qquad \text{(Eq. 7.13)}$$

By comparing Equation [7.13] with the BBM failure equation ($q = M(p + ks)$), the BBM shear strength parameters can be related to the conventional shear properties as follows:

$$M = \frac{3\left(K_p - 1\right)}{2 + K_p} = \frac{3\left\{\tan^2\left[\frac{\pi}{4} + \frac{\phi'}{2}\right] - 1\right\}}{2 + \tan^2\left[\frac{\pi}{4} + \frac{\phi'}{2}\right]} \qquad \text{(Eq. 7.14)}$$

$$k = \frac{2\tan\phi^b\sqrt{K_p}}{K_p - 1} \qquad \text{(Eq. 7.15)}$$

Using the same criterion described in the previous section (Fredlund's Shear Strength Parameters), the shear strength parameters were re-guessed forcing c' to be zero. The corresponding shear strength properties, ϕ' and ϕ^b, were 28.13 and 22.26 degrees, respectively.

Based on these shear strength parameters, the BBM strength parameters *k* and *M* were calculated using Equations [7.14] and [7.15] and were 0.74 and 1.13, respectively. The coefficient of determination (R-squared) between the measured and predicted shear strength was 94% which indicated an acceptable match.

BBM Stiffness Parameters

As previously mentioned, Zhang et al. (2016a) proposed an explicit formulation for at-rest earth pressure coefficient. Later, the procedure was successfully used by Zhang et al. (2016b) to calibrate the BBM parameters from a set of six constant water content oedometer test. This was achieved by combining a modified state surface approach, recently proposed to model the elastoplastic behavior of unsaturated soils under isotropic stress conditions, with the Newton or quasi-Newton method to simultaneously determine the BBM parameters.

Zhang and Lytton (2009a and 2009b) proposed the MSSA to study the mechanical behavior of unsaturated soils. In the MSSA, the void ratio was divided into an elastic and a plastic surface. The plastic surface is a unique constant surface, but the elastic surface is moveable depending on the occurrence of plastic deformations. Zhang and Lytton (2009a) derived mathematical expressions for the elastic and plastic surfaces for the BBM and successfully used the MSSA to represent many features related to unsaturated soils behavior. The BBM surfaces included an elastic surface and a plastic surface. The elastic surface is expressed by Equation [7.16]. The mathematical expression for the plastic surface is presented in Equations [7.17]. While the elastic surface is easy to determine, the major challenge is to determine the eight parameters related to soil plastic behavior, which are $N(0)$, $\lambda(0)$, β, r, p^c, M, K and α. It worth note, Alonso et al. (1990) suggested that α is chosen in such a way that the flow rule predicts zero lateral strain for K_0 stress state that is corresponding to Jaky's equation (Jaky, 1944)

$K_0 = 1 - \sin\varphi' = (6 - 2M)/(6 + M)$. Two assumptions are made to derive α: (a) the elastic shear strains are small and negligible and (b) for saturated and unsaturated conditions, the K_0 consolidation line shares the same slope and is constant. Zhang et al. (2016) found that neither assumptions holds true for unsaturated soils and suggested that α be used as an additional constant for the BBM.

$$v = C_1 - \kappa \ln p - \kappa_s \ln(s + p_{at}) \quad \text{(Eq. 7.16)}$$

$$v = N(0) - \kappa \ln \frac{p}{p^c} - \kappa_s \ln\left(\frac{s + p_{at}}{p_{at}}\right) - (\lambda(s) - \kappa)\left[\ln\left(p + \frac{q^2}{M^2(p + ks)}\right) - \ln p^c\right] \quad \text{(Eq. 7.17)}$$

Where ν= specific volume, p= mean net stress, q= deviatoric stress, s= suction, C_1= Constant related to initial specific volume of the soil, κ = slope of unloading reloading line in the p-e space, κ_s = slope of unloading reloading line associated with soil suction, p_{at} = atmospheric pressure, p^c= reference stress, M= slope of theoretical critical state line, k= parameter describing increase in cohesion with suction, $\lambda(s)$ = slope of virgin expansion line at different suction values associated with mean net stress, and $N(0)$ = constant representing virgin specific volume at zero suction value and mechanical stress.

Mathematically, the calibration problem can be described as follows: the calibration of the BBM parameters under K_0 condition is to find the appropriate combination of $N(0), \lambda(0), \beta, r, p^c, M, K$ and α, which can minimize the overall difference between the measured and predicted specific volumes. The eight CWOD tests (water content of 26.19%, 29.84%, 30.09%, 33.56%, 34.23%, 34.64%, 35.81%, and 46.06%) are used to calibrate the BBM model parameters. The procedure proposed by Zhang et al. (2016a) utilized here. The only difference is that the shear strength parameters were predefined from the CW direct shear tests

results as shown in the previous section. As previously explained in the chapter (6) the samples seem to have some disturbance during transportation. This made the initial conditions of different samples inconsistent. Therefore, $N(0)$ had a different value for each test. Practically, this is not going to make any significant difference, since the BBM incremental approach is going to be used for any further numerical simulations. However, this might make some difficulties when the MSSA surfaces need to be generated. Table 7.2 shows the calibrated BBM parameters. In order to verify the calibrated parameters, the predicted and measured specific volumes for each test are plotted and compared as shown in Figure 7.1. A coefficient of determination (R-squared) of 99.70% was reached that indicates a very good match.

Table 7.2 Calibrated BBM parameters by MST team.

Parameter	**Unit**	**Best Fit BBM Parameters**							
Test (Wc, %)		26.19%	29.84%	30.09%	33.56%	34.23%	34.64%	35.81%	46.04%
N(0)	---	2.119	2.131	2.097	2.182	2.155	2.224	2.249	2.507
κ_s	---	0.0066							
κ	---	0.0147							
$\lambda(0)$	---	0.075							
r	---	0.158							
β	MPa-1	3.182							
p^c	MPa	0.046							
α	---	0.802							
M	---	1.130							
k	---	0.740							
μ	---	0.350							

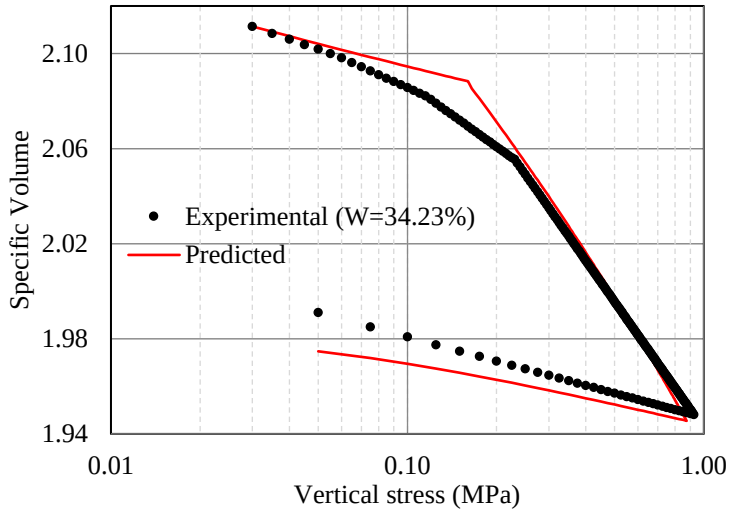

(a) Water content= 34.23%

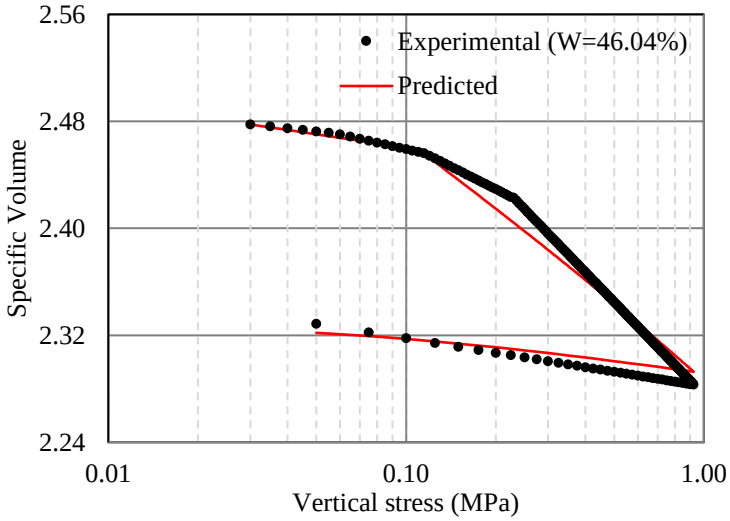

(b) Water content= 46.04%

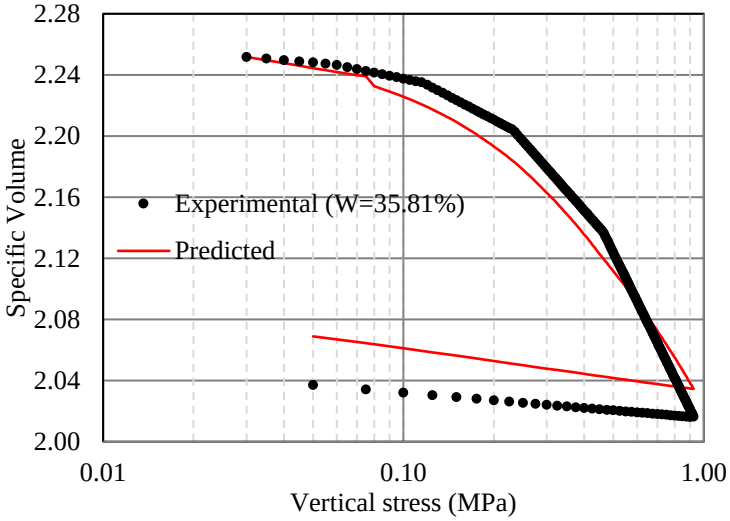

(c) Water content= 35.81%

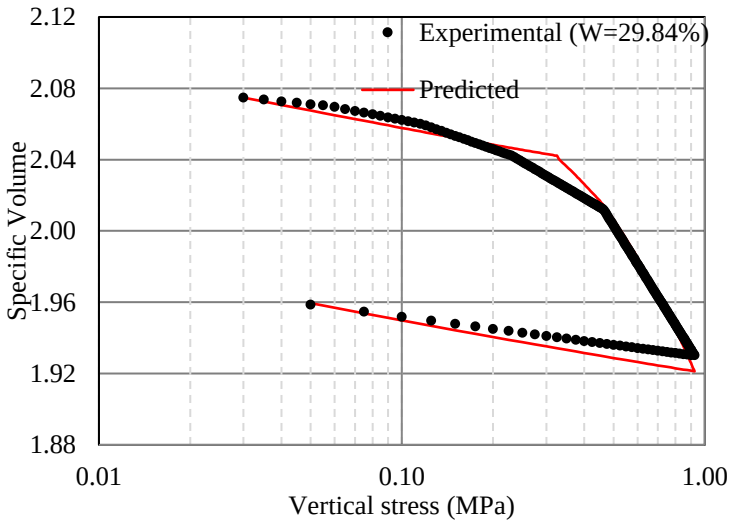

(d) Water content= 29.84%

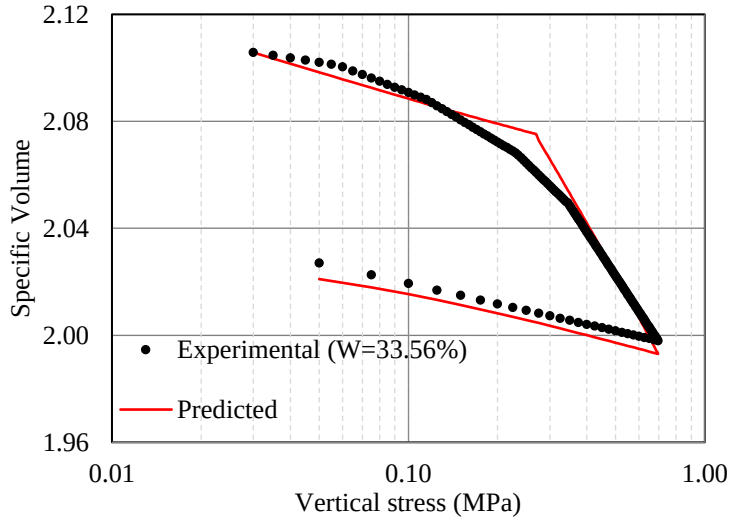

(e) Water content= 33.56%

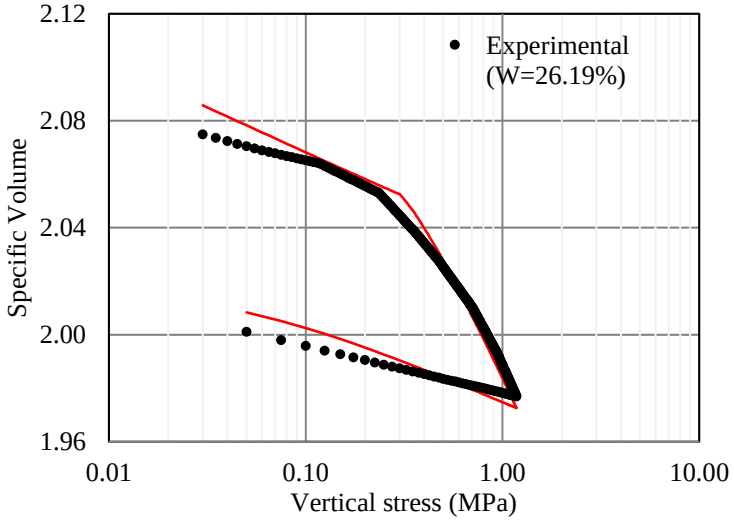

(f) Water content= 26.19%

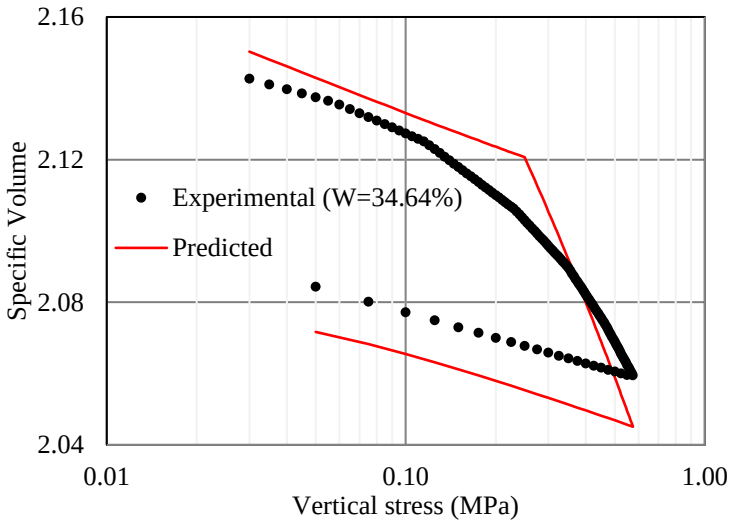

(g) Water content= 34.64%

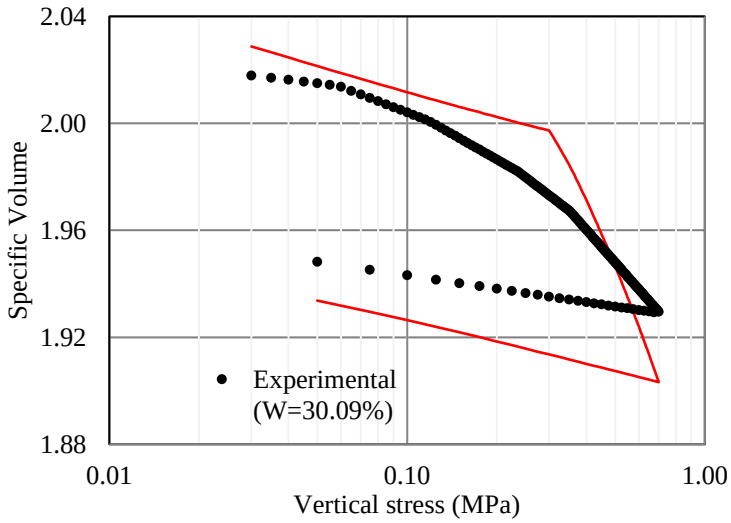

(h) Water content= 30.09%

Figure 7.1 Comparison between predicted and experimental results for oedometer tests at different water contents.

Based on the MSSA, the intercept between elastic and plastic surfaces in the *v-p-q-s* space is the yield hypersurface. By letting Equation [7.16] equal to Equation [7.17], the yield surface expression can be obtained as follows:

$$p_0 = p + \frac{q^2}{M^2(p+ks)} = P^C \exp\left(\frac{N(0) - C_1 + \kappa \ln(P^C) + \kappa_s \ln\left(p_{at}\right)}{\lambda(s) - \kappa}\right) \qquad \text{(Eq. 7.18)}$$

The size of the yield surface is controlled by the value of $C1$ constant that is changing continuously during plastic loading and causes a yield surface to revolution. Figure 7.2 shows the

initial shapes of the yield curves for each oedometer test. Deep investigation into Figure 7.2 indicated that when the mean net stress is greater than 0.1 MPa, suction increases with the increase of mean net stress on the yield curves, which is similar to the original BBM assumption (Alonso et al. 1990). This behavior explained by Zhang and Lytton (2009b) as a collapsible behavior when the mean net stress is greater than 100 kPa

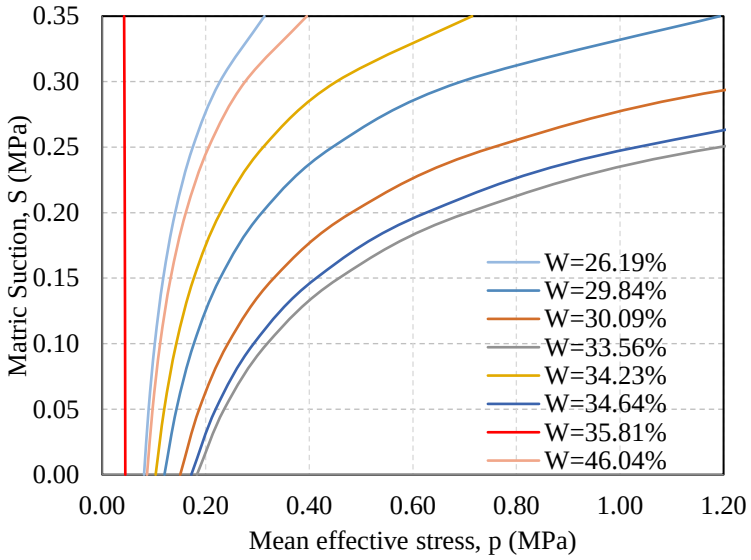

Figure 7.2 Initial yield curves for different samples.

7.3 University of Hawaii at Manoa Team

Introduction

The team at University of Hawaii at Manoa used a combined approach to define the BBM parameters (refer to Iwamoto, 2018). The BBM stiffness parameters were calibrated by fitting the MSSA elastic and plastic surface equations (Equations [7.16] and [7.17]). On the other hand, the BBM strength parameters were calibrated separately by fitting the strength equation, $q = M\left(p + ks\right)$, proposed by Alonso et al. (1990).

BBM Shear Strength Parameters

The elastic shear modulus, *G*, was calculated from the unload-reload portion of CWC-2 and 3 and the elastic regions of CD-15, -30, -50, and CWC-1. The shear modulus was estimated to be 6812 kPa. However, in reality, the shear modulus is pressure dependent as shown in the following expression

$$G = \frac{3p(1-2\mu)(1+e_0)}{2\kappa(1+\mu)} \qquad \text{(Eq. 7.19)}$$

where μ = Poisson's ratio, e_0 = initial void ratio, κ = slope of saturated unloading-reloading line, and p = mean net pressure.

Figure 7.3 shows the CWC and CD test results in $p-q$ space. From this plot, the BBM shear parameters (*M* and *k*) were determined. A limitation of the multi-stage CD triaxial test performed on the saturated sample is that post-peak strains are small for all stages except the final stage. Therefore, the CD test results for tests at confining pressures 15 kPa and 30 kPa could not be used to obtain the BBM shear parameters. The critical states of the test at 50 kPa multi-stage CD triaxial test on the saturated sample (henceforth denoted as CD50), and the three CWC tests were used to obtain the BBM parameters *M* and *k*.

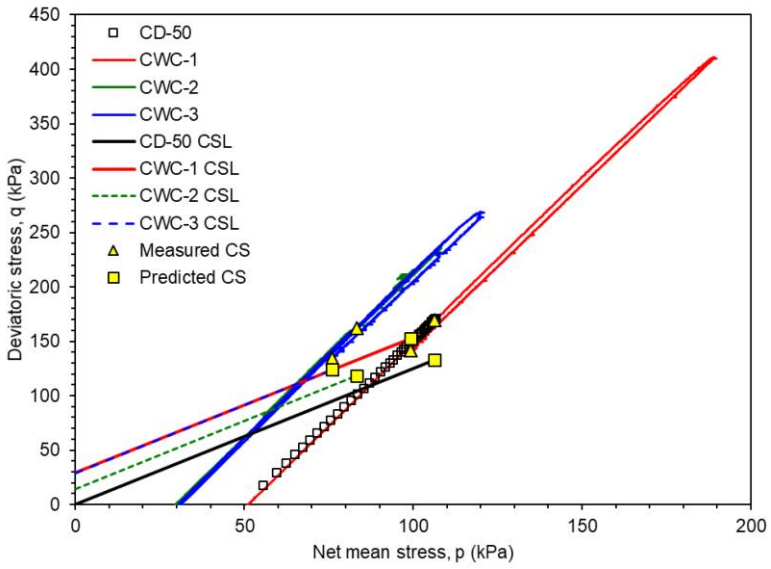

Figure 7.3 Stress paths and measured critical states for different triaxial tests (Iwamoto, 2018).

An ordinary least-square regression was used to fit the data at critical state of tests CD-50, CWC-1, CWC-2, CWC-3 to fit the BBM failure plane expressed by the following equation:

$$q = M\left(p + ks\right) \qquad \text{(Eq. 7.20)}$$

Where M and k are the BBM shear strength parameters estimated to be 1.34 and 0.34, respectively. A coefficient of determination of 87.2% was obtained between the measured and predicted deviatoric stresses. The critical state angle of internal friction is related to the *M* parameter by Equation 7.21 and was calculated to be 33.65º.

$$M = \frac{6\sin\phi_{cs}^{'}}{3-\sin\phi_{cs}^{'}} \qquad \text{(Eq. 7.20)}$$

BBM Stiffness Parameters

BBM stiffness parameters were calibrated using ordinary least square regression of the predicted specific volumes (using the MSSA expressions: Equation [7.16] and Equation [7.17])

and the measured values. The calibrated parameters are displayed in Table 7.3. The coefficient of determination between measured and predicted specific volumes was 97.80%.

Table 7.3 Calibrated BBM parameters by UHM team (Iwamoto, 2018).

Parameter	Unit	Best Fit
N(0)	---	1.90
κ_s	---	0.0039
κ	---	0.0181
$\lambda(0)$	---	0.13
r	---	0.01
β	MPa-1	6.22
p^c	MPa	3.33
R^2	---	97.90%

Figure 7.4 presents the LC yield curves for CWIC test and the 1D consolidation test calculated using the following expression:

$$p_0 = p^c \left(\frac{p_0^*}{p^c} \right)^{\frac{\lambda(0)-\kappa}{\lambda(s)-\kappa}} \qquad \text{(Eq. 7.20)}$$

Where p_0 is the yield stress at different suctions, p_0^* is the pre-consolidation pressure at saturation state, p^c, $\lambda(0)$, and κ are BBM parameters previously defined. The shape of the LC yodel curve can be classified as a type-3 based on Zhang (2015). These yield curve shapes were first deemed illogical by Alonso et al. (1990). However, Zhang and Lytton (2009b) theoretically proved that they are applicable for expansive soils.

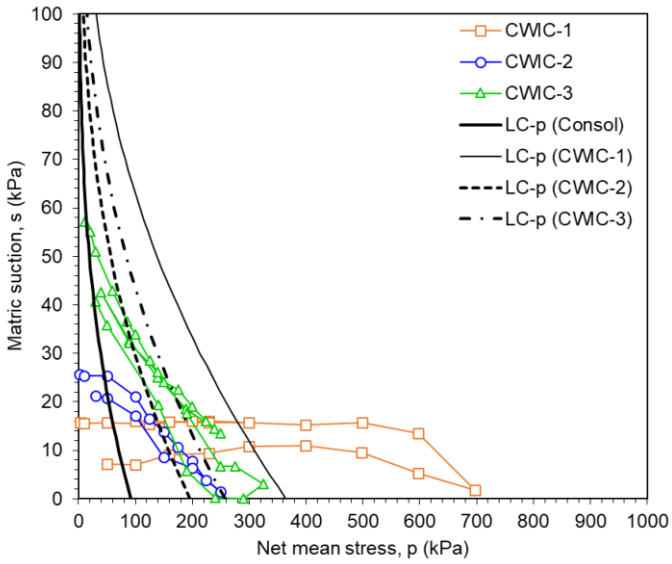

Figure 7.4 Predicted LC yield curves for different experimental tests (Iwamoto, 2018).

7.4 Comparison of BBM Parameters Obtained by MST and UHM Teams

Introduction

In the previous sections, two sets of parameters for the Barcelona Basic Model (Alonso et al., 1990) were calibrated independently by two teams (i.e., MST and UHM) using different experimental results. The MST team used the results from constant water content oedometer and direct shear tests. On the other hand, the UHM team used results from consolidated drained tests for saturated samples and constant water content triaxial tests for unsaturated samples. In this section, the calibrated stets of parameters are compared and critically discussed.

Stiffness Parameters

Table 7.3 presents the calibrated parameters from both teams. The constants $C1$ and $N(0)$ are not applicable when using incremental form, therefore the MST team provided values for each test rather than a single value. However, to model the field situations a single $N(0)$

shall be used. The LC yield curves provided by MST team (Figure 7.2) is type 1 based on Zhang (2015). Type 1 LC yield curve indicates a collapsible soil behavior. In contrary, the LC yield curves obtained by UHM team (Iwamoto, 2018) indicated a swelling soil behavior (discussed earlier, Figure 7.4). For the first glance, these two LC yield curves seem contradictory. Noting that Alonso et al. (1990) mentioned that a potentially collapsible soil subjected to a suction reduction from a relatively high value have been reported to experience first an expansion and then compressive strain (Escario and Saez, 1973; Cox, 1978; Josa et al., 1987). Considering the limited range of suction change (less than 100 kPa) applied by team UHM during testing and high range of suction changes (around 3500 kPa) applied by MST team during testing. These two LC yield curve, in fact, could be complementary not contradictory. To better calibrate the model parameters it is recommended to use the experimental results from both teams to determine one set of parameters.

Table 7.4 Calibrated BBM parameters by MST and UHM teams.

Parameter	Unit	Best Fit MST	Best Fit UHM
$N(0)$	---	Varies	1.90
κ_s	---	0.0066	0.0039
κ	---	0.0147	0.0181
$\lambda(0)$	---	0.075	0.13
r	---	0.158	0.01
β	MPa-1	3.812	6.22
p^c	MPa	3.812	3.33
G	MPa	Changes with pressure	7.85
μ	----	0.35 (assumed)	0.329
α	----	0.802	0.458
M	----	1.13	1.25
k	----	0.74	0.55

Shear Strength Parameters

The BBM contains 10 parameters to model unsaturated soil behavior. Three of those, *G*, *M*, and *k* are for modelling the soil behavior during shear (Table 7.2). MST team did not report the elastic shear modulus, *G*, as a BBM parameter. They assumed a Poisson's ratio of 0.35, which theoretically can be used to estimate a pressure dependent *G* using Equation [7.19]. In general, the calibrated strength parameters (*M*, and *k*) by both teams match very well as shown in Table 7.2.

CHAPTER 8: TRANSIENT HYDROLOGICAL FLOW MODEL

8.1 Introduction

The team at UHM calibrated a hydraulic flow model for saturated and unsaturated soils (for more details refer to Iwamoto, 2018). A saturated-unsaturated transient hydrological flow model was developed and calibrated for the purpose of estimating the suctions/pore water pressures in the soil slope during the design storm. As explained in Chapter 1, this model is an integral part of the landslide warning system. It has to be first calibrated to determine the appropriate parameters to use. Calibration is achieved by adjusting the hydraulic model parameters to match the laboratory measured and calculated SWCC and HCF, and to match calculated and field-measured suctions and water contents. Once the model is calibrated, then it can be used to predict the pore pressures during a storm with a prescribed design return period. Return period in transportation infrastructure design is typically based on a 100-year event. However, the return period can be justifiably increased depending on the importance of structure and consequence of failure. This slope has been in existence for many decades and may have already survived a 100-year if not higher storm. In fact, during the approximately three years of monitoring, the slope experienced a 200-year return period, 60-day duration storm in from 8/16/15 – 10/15/15. Since this slope abuts Kalanianaole Highway and the consequence of failure is “high”, it was decided to investigate the effects of a storm with a 500-year return period (= 1/500 or 0.2% annual probability of occurrence) to facilitate selection of threshold values for use in the development of a landslide warning system. Elements of this model are presented below.

8.2 Hydraulic Model

Pressure dependency of SWCC curves has been well documented in the literature. Much work has been expended to incorporate pressure dependent SWCC in coupled hydro-mechanical models either by expressing individual SWCC parameters such as the air entry suction as a function of confining stress (Gallipoli et al., 2003b; Huang et al., 1998; Nuth and Laloui, 2008; Cabarkapa and Cuccovillo, 2005; Hu et al., 2013; and UPC, 2017), or by expressing the SWCC as a function of the soil stress state (Sun et al., 2007b; Masin, 2010; Mbonimpa et al., 2006; and Zhou et al., 2012). In HYDRUS, the software used for the transient hydrological flow model, hysteretic behavior is only available for the Van Genuchten (1980) model. Therefore, only hydraulic models that express the van Genuchten parameters as functions of the stress state of the soil are considered. Hu et al., (2013) derived a relationship between the air entry suction and void ratio by considering changes in void ratio as a function of pressure. D'onza et al., 2011 and UPC (2017) introduced a similar equation to describe the van Genuchten parameters, P and λ, as a function of void ratio.

$$S_e = \frac{S - S_r}{S_l - S_r} = \left[1 + \left(\frac{s}{p} \right)^{\frac{\lambda}{1-\lambda}} \right]^{-\lambda} \qquad \text{(Eq. 8.1)}$$

$$p = p_0 \exp\left[a\left(\Phi_0 - \Phi \right) \right] \qquad \text{(Eq. 8.2)}$$

where S_r is the residual saturation, S_l is the maximum saturation, s is the matric suction (kPa), p and λ are the van Genuchten parameters, Φ is the porosity, and p_0 and λ_0 are the van Genuchten parameters at a reference porosity, Φ_0. D'onza et al. (2011) and

UPC (2017) expressed the van Genuchten equation in terms of p and λ which can be related to the van Genuchten parameters α and n, as follows:

$$p = \frac{g}{\alpha} \quad \text{(Eq. 8.3)}$$

$$\lambda = m = 1 - \frac{1}{n} \quad \text{(Eq. 8.4)}$$

where g is the gravity acceleration.

Data points during the loading stage were used to calibrate the main wetting branch of the pressure-dependent SWCC since suction decreases during compression. Conversely, data points during the unloading stage were used to calibrate the main drying branch of the pressure-dependent SWCC. The parameters, λ_0, b, and λ_0, were taken to be equal for both drying and wetting. The model parameters (a_d, a_w, p_0^d, p_0^w, b, λ_0, and Φ_0) were calibrated by performing ordinary least squares regression of the measured and predicted saturation and are presented in Table 8.1. The resulting coefficient of determination was 0.958 based on CWCIC tests 2 and 3 data. Using the parameters in Table 8.1 and Equation [8.1], the pressure dependent SWCCs are plotted in Figure 8.1.

Table 8.1 Calibrated pressure-dependent van Genuchten parameters.

Parameter	Unit	Drying Branch	Wetting Branch
Φ_0	---	80.13%	80.13%
p_0	kPa	3.32	0.003
λ_0	---	0.13	0.13
a	---	14.4	41.36
b	---	-0.01	-0.01

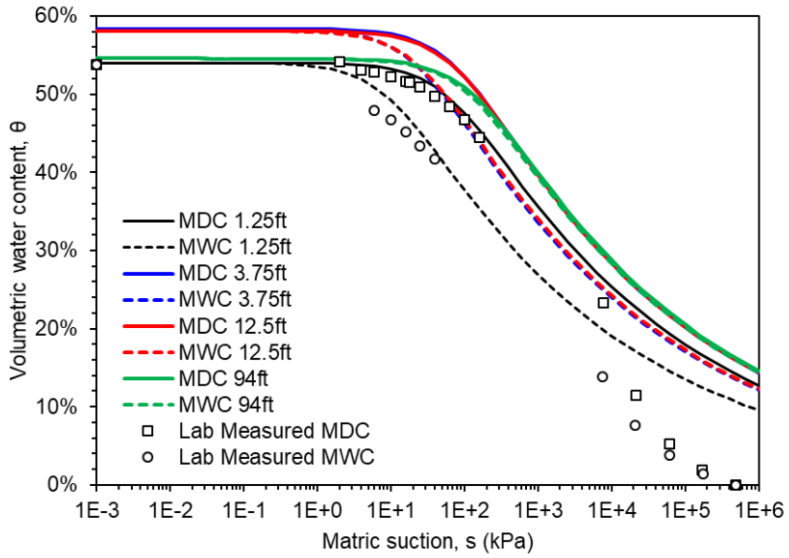

Figure 8.1 Predicted pressure-dependent SWCC (Iwamoto, 2018).

8.3 Calibration of the Infiltration-Evapotranspiration Model and Implementation

A soil's shear strength is governed by the shear strength parameters and the pore water pressure in the soil. The pore water pressure can be positive if the soil is below the ground water table or negative if it is above the ground water table. Since the ground water table at this site is purportedly more than 40 m below the slope crest, the slope is not subject to ground water recharge from below, and water can only enter the slope naturally in the form of precipitation. A systems analysis of the water balance at the site requires that the precipitation (P), runoff (R), evapotranspiration (ET) and surface infiltration (SI) satisfy the following:

$$P = R + ET + SI \qquad \text{(Eq. 8.5)}$$

It worth notice that the slope is relatively barren and for all intents and purposes, transpiration can be deemed negligible; i.e.; $ET \approx PE$ = potential evaporation. Thus, only the effects of precipitation and potential evaporation need be applied to the top boundaries (ground

surface) of the model. The method adopted for estimating PE is explained in the following section.

Potential Evaporation

While the precipitation is directly measured, potential evaporation at the site can be estimated with the aid of the following climatic parameters:

1. global solar radiation;

2. wind speed;

3. air temperature;

4. relative humidity;

5. cloud factor; and

6. albedo (from Giambelluca et al.; 2014),

Using these parameters, the PE could be estimated by utilizing Kohler and Parmele's (1967) modification of Penman's (1948) equation. After a process of trial and error involving several other methods of estimating PE, it was found that this method worked best for this site and their expression for PE is as follows:

$$PE = \frac{\Delta\left(J + L' - G\right) + \gamma' K_E \rho_w v_a e_e^* \left(1 - W_a\right)}{\rho_w \lambda_v \left(\Delta + \gamma'\right)} \qquad \text{(Eq. 8.5)}$$

where Δ=slope of saturation vapor-temperature curve= $\frac{2508.3}{\left(T_a + 237.3\right)^2} \exp\left(\frac{17.3 T_a}{T_a + 237.3}\right) \left[kPaK^{-1}\right]$, K=net shortwave radiation=$\left(1-a\right) K_{global}$, L' =adjusted net longwave radiation=$\varepsilon_s \sigma \left(1 - \varepsilon_{at}\right)\left(T_a + 273.2\right)^4$ (after Kohler and Parmele, 1967),

G=soil heat flux=$0.2(K+L')$ (after Fuchs and Hadas, 1972, Idso et al., 1975; and Novak and Black, 1983), γ'=adjusted psychrometric constant=$\frac{c_a p_a}{0.622\lambda_v}+\frac{2\varepsilon_s\sigma(T_a+273.2)^3}{K_E\rho_w\lambda_v v_a}$ (after Kohler and Parmele, 1967), K_E=atmospheric constant=$\frac{0.622\rho_a}{p_a\rho_w}\frac{V^2}{\left[\ln\left(\frac{z_m}{z_0}\right)\right]^2}$, ρ_w=mass density of water $\left[kgm^{-3}\right]$, v_a=measured wind speed $\left[ms^{-1}\right]$, e_a^*=saturated vapor pressure $[kPa]$=$0.611\exp\left(\frac{17.3T_a}{T_a+237.3}\right)$ (after Monteith and Unsworth, 2008), W_a=measured relative humidity, λ_v=latent heat of vaporization $\left[Jkg^{-1}\right]=2.5x10^{-6}-237T_a$, T_a=measured air temperature $\left[^oC\right]$, a=albedo (site-specific monthly values taken from Giambelluca et al., 2014), K_{global}=measured global solar radiation $\left[Wm^{-2}\right]$, ε_s=soil emissivity=$\min(0.9+0.18\theta;1)$ (after Van Bavel and Hillel, 1976), σ=Stefan-Boltzmann constant=5.67X10^{-8} $Wm^{-2}K^{-4}$, ε_{at}=atmospheric emissivity=$1.27\left(\frac{W_a e_a^*}{T_a+273.2}\right)^{1/7}$ (after Brutsaert, 1975), c_a=heat capacity of air=1x10^{-3} $MJKg^{-1}K^{-1}$, $p_a(z)$=atmospheric air pressure at elevation, z [kPa]= $101.32\left(\frac{293.0065z}{293}\right)^{5.26}$ (after Burman et al., 1987), ρ_a=mass density of air=$\frac{p_a}{0.288T_a}$ kgm^{-3}, V=von Karman constant typically=0.4 (after Dingman, 2008), z_m=height at which air temperature, relative humidity, and wind speed were measured=2.0 m, z_0=roughness height=1.1x10^{-3}m for bare soil (after Chow et al., 1988), and θ=measured volumetric water content near the surface. The calculated PE was plotted versus time and shown in Figure 8.2.

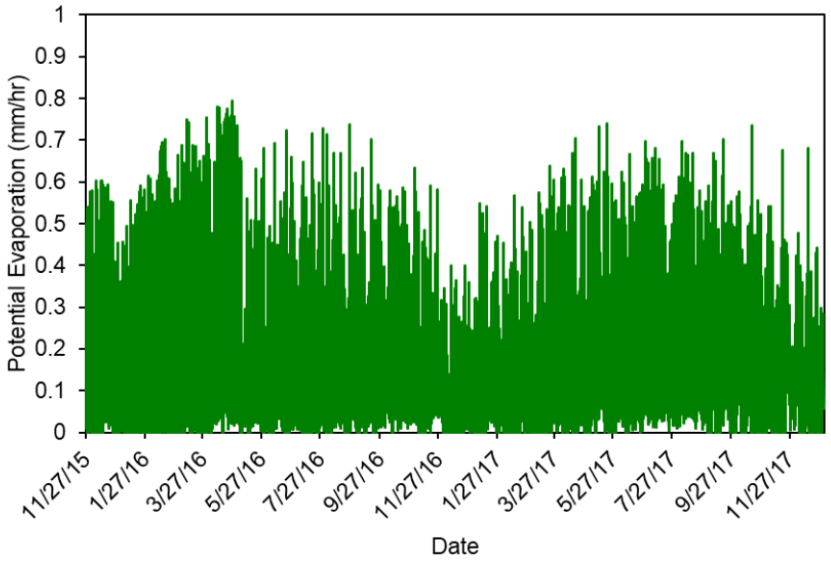

Figure 8.2 Potential evaporation estimated using Kohler and Parmele's (1967) modification of Penman's (1948) equation at the slope site.

It should be noted that global solar radiation, wind speed, air temperature and relative humidity were obtained from Hihara and Sugamoto (2017), who are with the University of Hawaii's Department of Mechanical Engineering, and their data cannot be readily accessible by the general public. Alternatively, a similar set of such data can be downloaded from a weather station on Coconut Island (Hawaii Institute of Marine Biology). However, it was found that for the period of this research, the Coconut Island data is sporadic with missing gaps. This is why, the Hihara and Sugamoto (2017) data was adopted for this study.

8.4 Transient Hydrological Flow Model

Iwamoto (2018) utilized HYDRUS software to simulate the transient hydrological flow. This could be justified that HYDRUS is the only software that considers the hydraulic scanning behavior for soils. The parameters calibrate for the wetting and drying branches for the pressure dependent SWCC in section 8.2 used along with the PE as a boundary condition for a 2D model

in HYDRUS software. Figure 8.3 shows the 2D finite element mesh for the flow model. The model results were compared against the field suction (from tensiometers) and water content (from water content sensors) measurements at different depths as shown in Figures from 8.3 to 8.6. The model fits the field measurements in a reasonably good manner. This is the best that can be obtained with the limited time and resources available, and this model and parameters in Table 8.1 was then utilized to determine the pore water pressure/suction profile in the slope after a design storm, which is taken to be a 500-year storm.

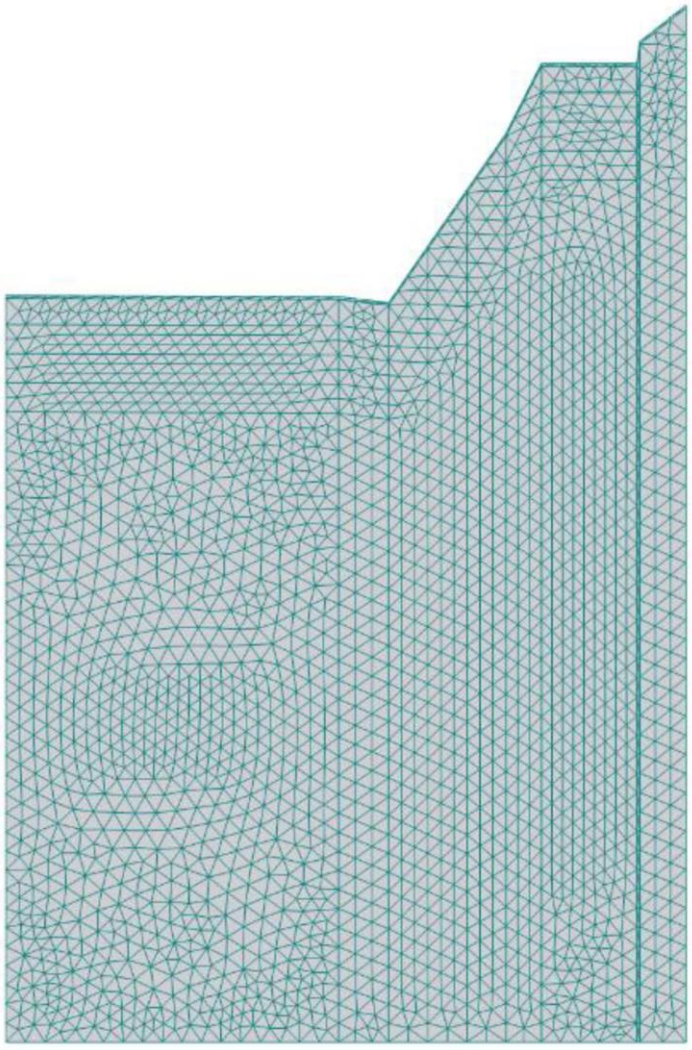

Figure 8.3 2D HYDRUS finite element mesh (Iwamoto, 2018).

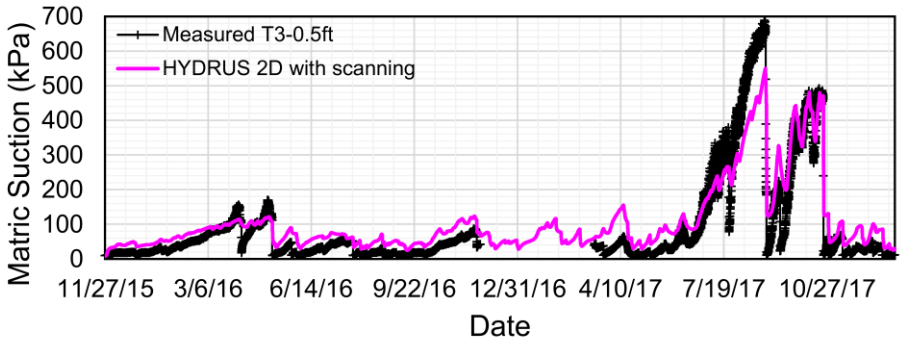

(a) Matric suction versus time

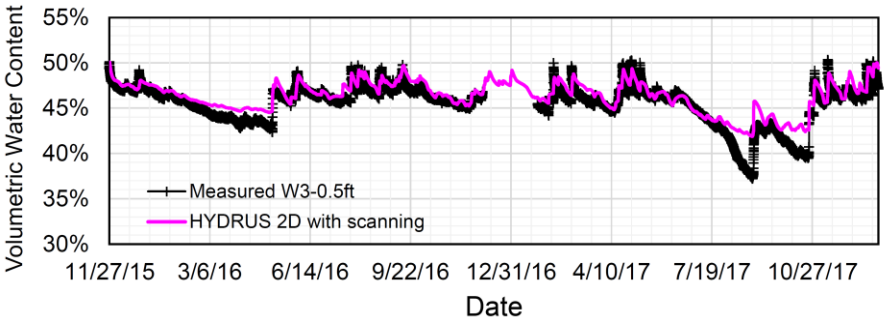

(b) Volumetric water content versus time

Figure 8.4 2D HYDRUS model predictions versus field measurements at depth 0.15m (Iwamoto, 2018).

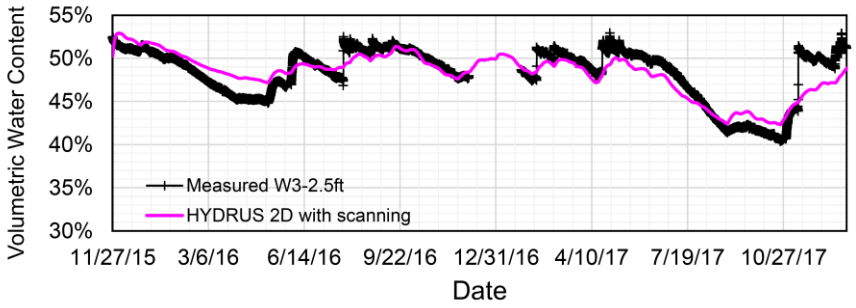

Figure 8.5 2D HYDRUS model water content predictions versus field measurements at depth 0.76m (Iwamoto, 2018).

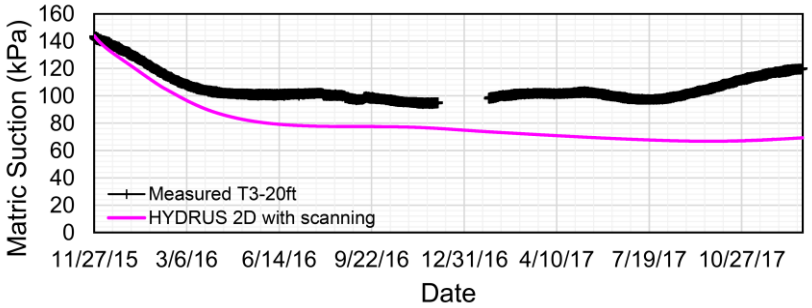

Figure 8.6 2D HYDRUS model matric suction predictions versus field measurements at depth 6.10m (Iwamoto, 2018).

8.5 Transient Hydrological Flow Model during A Storm With A 500-Year Return Period

The 500-year-return period precipitation intensity vs duration frequency curve (IDF) for the site was downloaded from NOAA's National Weather Service precipitation frequency data server (2018) and used for the slope site. The 500-year return period storm revealed tow critical precipitation duration or intensity values. The critical values are 5-minute (622 mm/hr) and 60-day (1.25 mm/hr) that were used for the 2D HYDRUS analysis. It was found that the longer duration low intensity storms are most critical when analyzing slope stability. Two initial conditions were considered; one starting at a relatively dry time (May 2, 2015 19:00) and the other at a relatively wet time (November 27, 2015 05:00) of the monitoring period.

The 500-year design storm could occur when the ground is already saturated to begin with or when the ground is dry. When the initial conditions are wet to begin with, it would mean that the design storm's actual return period is higher than 500-years. Nevertheless, both sets of initial conditions are indeed possible and were utilized to provide good insight into what may occur in the field. The HYDRUS analyses were extended for another 60 days beyond the end of the 500-year storm as the moisture was still making its way into the soil after the rain event. During the 60-day extension, it was assumed that the precipitation ceased and there was no evaporation (conservative). Figures 8.7 and 8.8 represent the suction contours at the end of the storm and 60 days after the storm. The suction contour plots were then utilized to perform stability analyses of the slope, as described in Chapter 9.

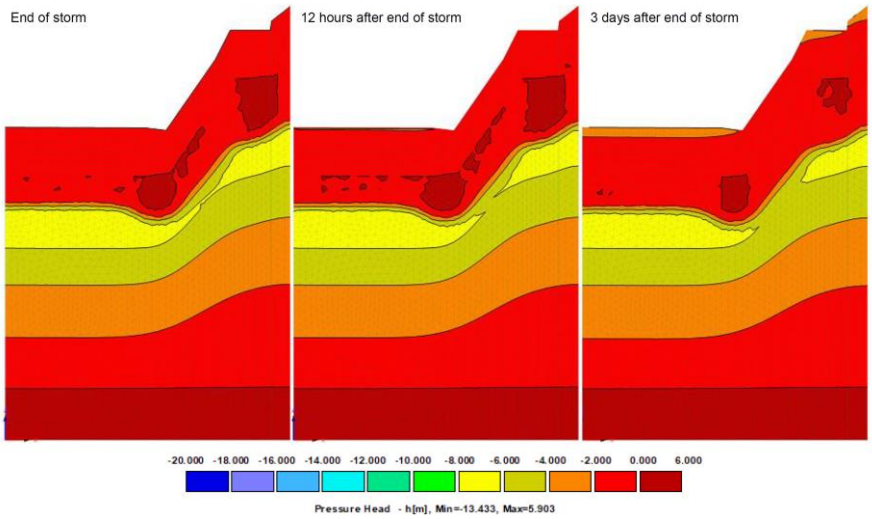

Figure 8.7 Suction contours for an initially dry slope during 60-day duration 500-year return period storm (Iwamoto, 2018).

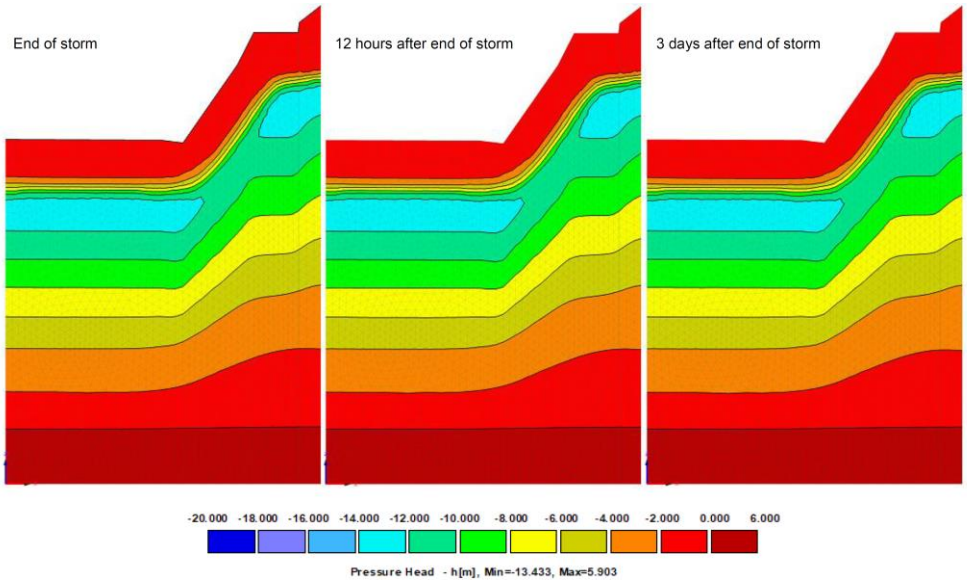

Figure 8.8 Suction contours for an initially wet slope during 60-day duration 500-year return period storm (Iwamoto, 2018).

CHAPTER 9: SLOPE STABILITY ANALYSIS

9.1 Introduction

The slope stability analysis was also performed by Melia K. Iwamoto and results are presented in detail in her PhD thesis (Iwamoto 2018). A 2D slope stability analysis for the actual slope geometry assuming full saturation was performed as a first step to justify the slope stability when fully saturated. This was followed by a 2D slope utilizing the suctions estimated for the 500-year storm. The software used for this analysis was SLOPE/W (Geo-slope International, Ltd., 2012) that is typically used for slope stability analysis in routine geotechnical projects. The SLOPE/W has an advantage over most of the existing slope stability software that it allows to study unsaturated soils slopes.

9.2 2D Slope Stability Analysis Assuming Full Saturation

In this analysis, the calibrated shear strength parameters (Chapter 7) along with the slope geometry (Chapter 3) were utilized. The 2D factor of safety for the slope when entirely saturated was calculated using the method of slices with the aid of the search routines in SLOPE/W. The factors of safety using Bishop's simplified (1955), Price and Morgenstern's (1965), Spencer's (1967) and Sarma's (1973) methods were calculated to be 0.520, 0.530, 0.493 and 0.522, respectively. Bishop’s simplified method satisfies overall moment equilibrium and force equilibrium only in the vertical direction. Even though it does not satisfy force equilibrium in the horizontal direction, it is commonly used in the geotechnical profession because it is known to be reasonable if the limitations are recognized and overcome. The last three methods satisfy all conditions of equilibrium and therefore, should provide factors of safety accurate to within ±5%

for any condition (Duncan and Wrigth, 2005). When entirely saturated, the factors of safety indicate that the slope is unstable. However in reality, the slope is still standing and is unsaturated. This demonstrates the importance of suction in keeping this slope stable since suction increases the soil shear strength and also the factor of safety of the slope under normal ambient unsaturated soil conditions.

9.3 2D Slope Stability Analysis during 500-Year Storm

Suction values from HYDRUS can be imported into SLOPE/W to perform 2D slope stability analyses for the 500-year storm. SLOPE/W interpolates between suction values to generate equal suction contours, which are then used to estimate the shear strength of the soil. When the slope is unsaturated, SLOPE/W estimates the shear strength of the soil at the bottom of each slice in accordance with the following equation proposed by Vanapalli et al. (1996b):

$$\tau = c' + (\sigma - u_a)\tan\phi' + (u_a - u_w) S_e \tan\phi' \qquad \text{(Eq. 9.1)}$$

where S_e is the degree of saturation and can be expressed in terms of suction using van Genuchten (1980) model, therefore the shear strength equation becomes:

$$\tau = \left[c' + (\sigma - u_a) + \frac{(u_a - u_w)}{\left[1 + (\alpha (u_a - u_w))^n\right]^{(n-1)/n}} \right] \tan\phi' \qquad \text{(Eq. 9.1)}$$

Equation [9.1] implies that the shear strength is expressed in terms of suction stress as follows:

$$\tau = \left[c' + (\sigma - u_a) + \sigma^s \right] \tan\phi' \qquad \text{(Eq. 9.1)}$$

To study the slope stability foe unsaturated soil slope, the suction values along with the α and n parameters shall be used. The calibrated parameters in Chapter 8 are valid only for wetting or drying SWCC branches. However, the soil in field is following a scanning curve. To fix this problem, Iwamoto (2018).came up with a solution to calculate the suction stress manually as follows: (a) use values of $(u_a - u_w)$ and θ from HYDROUS to manually calculate the suction stress $\sigma^s = \left[\theta / \theta_s\right](u_a - u_w)$, (b) input the calculated σ^s throughout the slope geometry as the soil suction , $(u_a - u_w)$, and assign $\alpha = n = 1$, and (c) calculate the slope factor of safety.

The same four methods of analyses used for the saturated case (Bishop's simplified, Morgenstern-Price's, Spencer's and Sarma's methods) were utilized to analyse the unsaturated case during the 500-year storm. Summarized in Table 9.1, the results indicate that:

(a) The 60-day low-intensity storm on an initially dry slope yielded the lowest factors of safety. The factors of safety increased as the storms trend toward the shorter duration higher-intensity variety.

(b) Overall, the factors of safety are greater than 1.19 suggesting that the slope will survive a 500-year storm. For the 60-day low-intensity storm, the lowest factors of safety occur at the end of the storm under initially dry conditions.

(c) There was a delayed response for the initially wet slope. The minimum factor of safety occurred three days after the end of the storm.

(d) The 60-day duration storm is severe enough to decrease the suctions in the deeper layers to values lower than at shallower depths. This has never been observed in the field at the time of monitoring.

Table 9.1 500-year duration storm 2D factor of safety.

Analysis method	Factor of safety		
	End of storm	3 days after storm	30 days after storm
Simplified Bishop	2.28	2.23	2.21
Morgenstern-Price	2.58	2.40	2.62
Spencer	2.61	2.40	2.65
Sarma	2.34	2.24	2.23

9.4 Threshold Values

A rainfall-induced landslide warning system essentially involves using the observational method (OM) to identify if a slope is rapidly deteriorating. For this particular slope, the "cause" of the rapid deterioration is extreme rainfall and the "symptoms" may include elevated volumetric water content, reduced suction and/or increasing slope movement. According to Nicholson et al. (1999), the observational method is only applicable if the soil behaves in a ductile fashion; i.e.; significant displacement is required to mobilize the peak strength. If the soil is brittle (i.e.; small displacement to mobilize peak strength which is true for the stiff silt in this slope), then Nicholson et al. (1999) stated that the OM is not applicable. With this slope however, it can be argued that because the permeability of the soil, k, is quite low ($k < ksat = 10^{-6}$ cm/s), there will be ample lead time to forecast whether a slide is impending provided continuous monitoring data of suction/volumetric water content is available. Nicholson et al. (1999) proposed a traffic-light-based trigger criterion that is useful for establishing instrument thresholds as follows:

(a) Green = safe site condition

(b) Amber = decision stage

(c) Red = implement planned modifications

Iwamoto (2018) followed the same traffic light approach to provide a threshold values for this project. For an instrument to be considered a good candidate for use as a threshold indicator,

the response has to be in the correct direction. After deeply investigating the instrumentation readings it was found that Tensiometer (T3) and water content sensor W3 are the most suitable candidates to be a threshold indicators. Realistically, the tensiometer cannot read suctions less than 9 kPa due to the limitation of the sensor. The threshold values have to be selected with awareness of this sensor limitation. The HYDRUS analysis for the 500-year, 60-day duration low intensity storm tends to under-predict suctions at this depth, and the field measured suctions which averaged 115 kPa and with minimum and maximum readings of 94 and 193 kPa. Therefore the proposed amber and red thresholds are 70 and 50 kPa accompanied by at least 14 days of rainfall averaging about 1 inch/day (0.043 inches/hr). Table 9.2 shows the proposed threshold values for the various monitoring instruments in the light of the hydraulic and mechanical (failure) analysis performed using HYDRUS and SLOPE/W software respectively.

Table 9.2 500-year duration storm 2D factor of safety.

Instrument	**Amber Threshold value**	**Red Threshold value**	**Accompanying event for threshold**
W3 at 0.15 m	0.51	0.53	2 day rain averaging about 1 in/day
W3 at 0.76 m	0.54	0.55	14 days rain averaging 1 in/day
T3 at 0.15 m	10 kPa	---	2 day rain averaging about 1 in/day
T3 at 6.1 m	70 kPa	50 kPa	14 days rain averaging 1 in/day

Planned modifications for the amber trigger can consist of placing tarp or geomembrane on the slope crest to minimize infiltration into the slope. For the red trigger, closing the lane closest to the slope may be prudent until the suctions increase and the water contents decrease.

CHAPTER 10: FEM ANALYSIS

10.1 Introduction

The original intention for this project was to develop threshold values based on another measured symptom, lateral deflection, in addition to suction and volumetric water content. However, due to the limitations of the software utilized in this research, it was decided that any threshold values of lateral deflection developed based on finite element analyses would be difficult to justify with a great deal of confidence. The reasons can be explained by identifying the software limitations below. The Team at Missouri University of Science and Technology ran several tentative models using CODE-BRIGHT software to justify the software capabilities.

10.2 CODE_BRIGHT FEM Software

Introduction

Code-Bright has been developed at the Department of Geotechnical engineering and Geosciences, University of the Polytechnic University of Catalonia (UPC). This code has been developed to carry out a simulation of Coupled Deformation Brine, Gas and Heat Transport. Code-Bright could be used to solve load-displacement, gas pressure, liquid pressure, and inclusion content problems. The code was first developed on the basis of a new general theory for saline media (Olivella et al. 1996). After that, the code was generalized for modeling coupled thermos-hydro-mechanical processes in geological media.

The code uses the finite element to discretize the space (geometry) and finite deference for time discretization for the partial differential equations. For non-linear iterative scheme, the Newton-Raphson method is used. The mass and energy balance equations are used for flow-type

problems, while the stress equilibrium equations are used for equilibrium-type problems. The program is designed for a wide range of problems from simple uncoupled cases to more complicated cases.

One of the main advantages of Code-Bright is the wide range of material constitutive laws included. The constitutive laws in Code-Bright are categorized as hydraulic and thermal constitutive models and mechanical models. The hydraulic and thermal constitutive models include retention curve intrinsic permeability, liquid and gas phase relative permeability, diffusive fluxes of mass, diffusive fluxes of mass and energy constitutive flux of heat. The mechanical constitutive models include Elasticity, non-linear elasticity, visco-plasticity for saline and granular materials, visco-plasticity for unsaturated soils based on BBM, damage-elasto-plastic model for argillaceous rocks, a thermo-elasto-plastic model for soils, and CASM's family models. One additional powerful option in the material constitutive models is the new material command. The new material command gives the ability to create a new material taking an existing material as a base material. The new material will have the same fields as the base material. Moreover, the properties of materials could be changed each interval. This gives the ability to define any material with time-dependent properties using Code-Bright. The thermos-hydro-mechanical (THM) ability coupled with material constitutive laws and interval dependent material properties make Code-Bright a very powerful tool for numerical simulation of unsaturated collapsible and expansive soils as well as frost-heave problems.

Many researchers used Code-Bright to study and investigate the behavior of unsaturated soils and frost heave-problems. Rutqvist et al. (2005) used Code-Bright for coupled thermal-hydrological-mechanical-chemical analysis. In this research, a multiyear large-scale underground heating test was performed to investigate the coupled-thermal-hydrological-chemical behavior of

unsaturated fractured and welded tuff in Yucca Mountains, Nevada, USA. Afterwards, the experimental results were compared against four different numerical models performed by different research teams. In this study, the capability of Code-Bright to perform such complicated coupled problems was investigated and verified. Code-Bright was used successfully to investigate and study the behavior of expansive unsaturated soils based on the coupling between micro and macro structures of the soil (Sánchez et al. 2005). In this study, Code-Bright was used to simulate three application cases. Of particular interest is the simulation of an accidental overheat took place in a large-scale heating test for 0.64 m thick engineered barrier made up of compacted bentonite.

Code-Bright has the capability to consider the dynamic Evapotranspiration (ET) boundary condition coupled with THM analysis. This capability was used by Rodríguez et al. (2007) to analysis and study the desiccation of a mining waste. In this test a set of experimental results to characterize the mining waste hydraulically and mechanically. Afterwards, a theoretical formulation was developed based on the experimental results. Finally, Code-Bright was successfully used to simulate the some of the experimental tests considering the ET process to predict the time and location of crack initiation.

Hydro-Mechanical Slope Stability Analysis

Barcelona Basic Model (BBM) (Alonso et al., 1990) coupled with van Genuchten (1980) equation were used to study the hydro-mechanical behavior. Both models are already implemented in CODE_BRIGHT. The BBM (Alonso et al., 1990) used for studying the mechanical behavior is coupled with a modified form of the van Genuchten (1980) equation proposed by Universitat Politecnica de Catalunya (UPC, 2017) for the hydraulic behavior. The BBM is an elasto-plastic model that can be considered as state-of-the-art for unsaturated soils at

the time of writing. The model was formulated for isotropic and triaxial compression stress states. It can model both collapse and expansive responses of unsaturated soils upon wetting. When the soil reaches saturation, the BBM defaults to the modified Cam-clay model. The Calibrated parameters the BBM by MST team (Chapter 7) along with the calibrated parameters for van Genuchten by UHM team (Chapter 8) are used. A significant limitation for the CODE_BRIGHT is that it doesn't consider the hydraulic hysteresis behavior for the SWCC. In reality, all the wetting and drying paths in the field are following the scanning curve. Neglecting the hydraulic hysteresis behavior, CODE_BRIFGT was used to simulate the soil initial condition and to check the suction distribution. Figure 10.1 shows the FEM mesh for CODE_BRIGHT simulation. The ground water table was assigned at 30 m depth from the slope crest. A time interval for 1 day was utilized for the soil to reach equilibrium. The pore water pressure distribution is presented in Figure 10.2. The pore water pressure at the slope crest is negative (i.e., suction) and equal to -0.314 MPa. Figure 10.3 shows the initial conditions for the second stage in which the slope surface was subjected to a phase of 30 days continuous raining and the slope behavior was further investigated. Figure 10.4 shows the liquid pressure distribution at the end of the 30 days. Figure 10.5 shows the slope lateral displacement at the end of 30 days. It is clear that the maximum slope displacement was 5.23 cm. The lateral movement distribution can be used as an additional threshold value when compared with the inclinometer field reading. However, it was noticed that the inclinometer readings were very minimal and within the device accuracy. Moreover, again, CODE_BROGHT neglects the hydraulic hysteresis and cannot be used for these kind of cycles of wetting and drying. This preliminary FEM was just to investigate the software capabilities. After extensive use of this software to solve just hydro- or seepage problems for the unsaturated slope, it was discovered that agreement between the calculated and measured values of suction and volumetric water content was difficult to achieve. When the field

suction paths were superimposed on the SWCC, it was realized that the field values of suction and water content do not follow the wetting or drying curves in most instances. Instead, they scan. Since CODE_BRIGHT does not allow scanning, it was recognized as a major limitation that precluded its use to evaluate the slope deformation behavior.

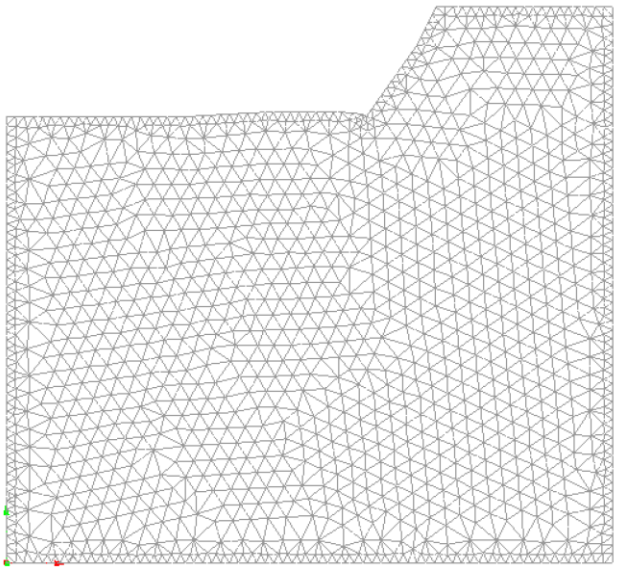

Figure 10.1 FEM mesh for CODE_BRIGHT.

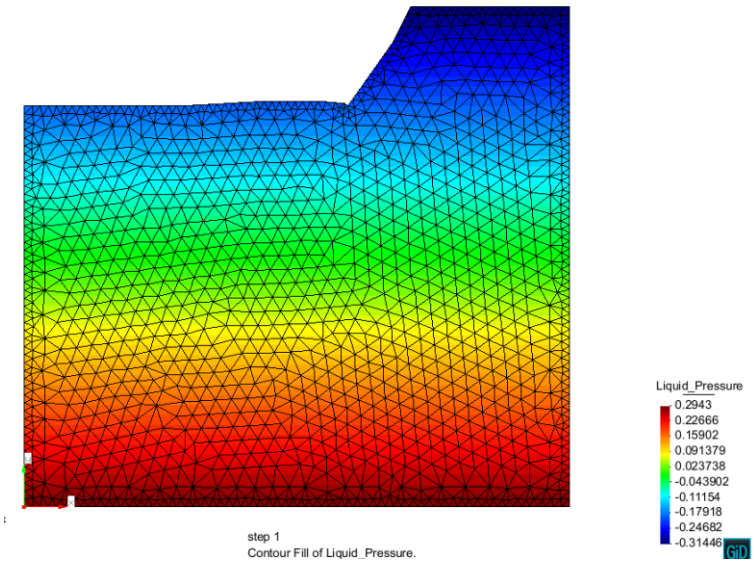

Figure 10.2 Pore water pressure distribution at the initial stage.

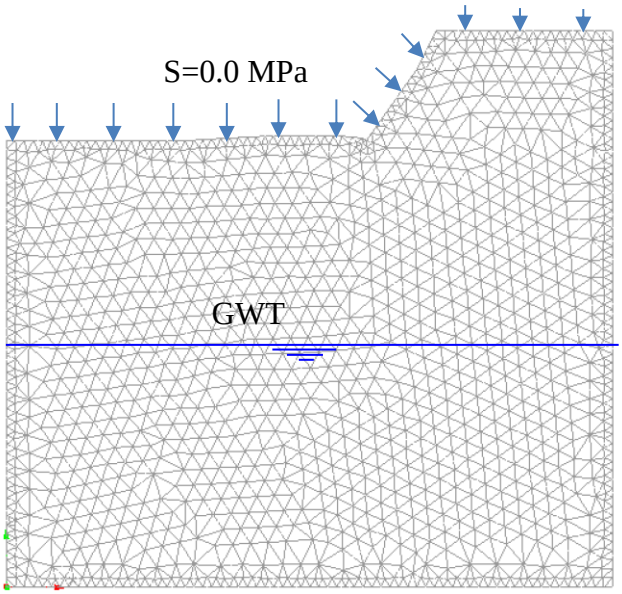

Figure 10.3 Second stage conditions.

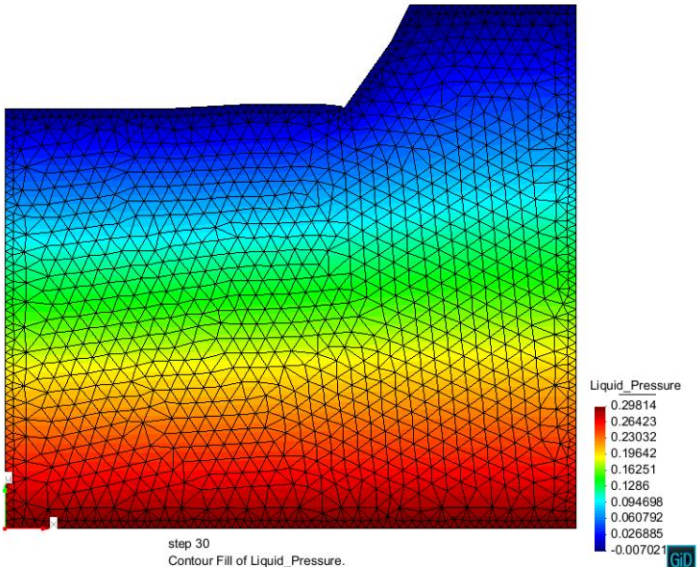

Figure 10.4 Pore water distribution at the end of 30 days.

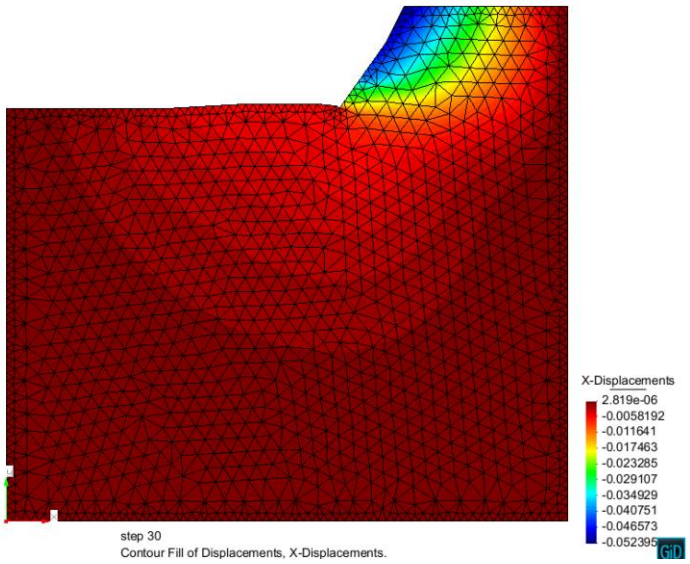

Figure 10.5 Later displacement at the end of 30 days.

CHAPTER 11: SUMMARIES, CONCLUSIONS AND SUGGESTION FOR FUTURE RESEARCH

11.1 Summary and Conclusion

A landslide warning system was developed for a cut slope along Kalanianaole Highway. The project was divided into several phases. The first phase performed a subsurface investigation, collected soil samples, and performed laboratory tests and unsaturated soil characterization. The second phase related to filed monitoring and collecting data related to soil suction, water content, deformation, and climatic changes. The last phase studied the slope stability analysis. The stability analysis was done by: (a) developing and calibration a saturated-unsaturated transient hydraulic model using HYDRUS software, (b) validating HYDRUS model by comparing its predictions for pre water pressure with the filed measurements, and (c) transferring the pore water pressure to SLOPE/W software for slope stability analysis.

The collected soil samples were shipped to two different laboratories for testing. The testing program at UHM consisted of: (1) consolidated drained triaxial testing for saturated soil samples, (2) one oedometer test for saturated sample, (3) pressure plate and Vapor Sorption Analyzer device testing for unsaturated soils to define the soil water characteristic curve and HCF, and (4) constant water content triaxial and isotropic compression testing for unsaturated samples. While the testing program at MST consisted of: (1) constant water content oedometer testing, and (2) constant water content direct shear testing. In order to perform constant water testing, the MST team developed their own apparatuses. They fabricated large size and miniature high-suction tensiometers (HST) to be used for suction measurement. Moreover, they modified

the conventional direct shear and oedometer cells. The fabricated HSTs were mounted to the modified cells.

The experimental index tests showed that the soil was a uniform stiff to very stiff high plasticity silt. Both UHM and MST teams used different approaches to, independently and separately, calibrate two sets of parameters for Barcelona Basic Model. Later, the calibrated sets were compared and discussed. The discussion indicated that the calibrated strength parameters agreed very well. However, the calibrated stiffness parameters seemed to reveal contradictory conclusions. After deeply discussing the parameters in the light of Alonso et al. (1990) it was found that, considering the suction change ranges subjected by each team, the two conclusions are complementary. The soil may sustain, first, expansive behavior and, later, collapsible behavior during wetting from higher suction levels.

Field instruments installed included tensiometers to measure in situ suction, water content sensors to measure volumetric water content, in-place inclinometers to measure lateral ground deflections and a rain gage to measure precipitation at the slope site. A saturated-unsaturated transient hydrological flow model was developed and calibrated using the field data and the lab test data. Calibration was achieved by adjusting the model parameters to match the laboratory measured and calculated SWCC and HCF, and to match calculated and field-measured suctions and water contents. The following conclusions can be made from this research.

(1) The field suction path usually runs along a scanning curve except during periods of heavy rain or extreme drought when the field suction path could join up and run along the wetting or drying branches, respectively. Therefore, it is important for a saturated-unsaturated transient flow model to allow for scanning in order to predict field behavior reliably;

(2) If scanning is not allowed, the calculated field suction path will run along the main drying or main wetting branches only, depending on which is specified. Doing so will result in over-estimated suctions and water contents when the SWCC and HCF are specified for the drying branch only. Conversely, use of the wetting branch only will yield under-predicted suctions and water contents;

(3) To the author's knowledge, HYDRUS (Simunek et al. 2006) is the only commercial software that allows scanning. HYDRUS requires the analysis to begin on either the main drying branch (i.e.; during a period of extreme drought) or the main wetting branch (i.e.; during a period of extreme rain). It doesn't allow an analysis to begin on a scanning curve. This limitation governs/pre-determines the initial conditions to use in an analysis;

(4) Using pressure dependent SWCC is more reliable and provides good match with the field measurements;

(5) When HYDRUS was rerun using pressure-dependent SWCCs, the calculated water contents and suctions matched better with the measured values especially deeper;

(6) HYDRUS was used to estimate suction and volumetric water contents within the slope during and after a 500-year storm. These suctions and water contents were transfer to SLOPE/W software to run a 2D slope stability analysis.

(7) Based on 2D slope stability analyses, the calculated factors of safety suggest that the slope shall survive the 5-minute-duration, high intensity 500-year storm where the lowest factor of safety (> 2.0) occurred about 3 to 30 days after the end of the storm. For the 60-day-duration, low-intensity 500-year storm, the factors of safety were lower than the 5-minute, high intensity variety. The lowest factor of safety was 1.3, which occurred at the end of the storm;

(8) Instrument thresholds were established using a traffic-light-based trigger criterion proposed by Nicholson et al. (1999);

(9) Instrument threshold values were selected in light of whether the HYDRUS prediction was trending in the right direction during a storm, in light of sensor limitation (e.g.; tensiometers cannot read below 9 kPa), in light of the agreement between calculated and predicted sensor responses during calibration, and in light of the field measured average, minimum and maximum values. Instrument threshold values could be established for 2 water content sensors and 2 tensiometers with confidence;

(10) Instrument threshold values were not established for the inclinometers due to the limitations of the software utilized in this research. For instance, CODE_BRIGHT does not consider the hydraulic hysteresis behavior. Therefore, it was decided that any threshold values for lateral deflection developed based on finite element analyses would be difficult to justify with a great deal of confidence.

11.2 Suggestion for Future Research

The following are suggestions for future research or suggestions if additional research work were to be conducted for this or similar slope site:

1. "Undisturbed" soil samples were collected using modified California samplers. To decrease sample disturbance, Pitcher samplers should be used to collect samples if the soils are stiff and where use of Shelby tubes is precluded.
2. Pressure-dependent SWCC tests should be conducted to validate the UPC (2017) porosity-based model used in conjunction with BBM parameters derived from isotropic compression test data.

3. A fully coupled hydro-mechanical unsaturated soil model that considers both the hydraulic and mechanical hysteresis behaviors should be able to better simulate the slope behavior. Progress towards this model was done by the team at MST. MST team developed a new fully coupled hydro-mechanical model that considers both hydraulic and mechanical hysteresis of unsaturated soils. The paper title is "A Modified State Surface Approach to Study the Unsaturated Soil Hysteresis Behavior". The model development was submitted to the TRB 2020 conference and it was tentatively accepted for journal publication. The paper in the review phase now.
4. The model mentioned in the above item shall be implemented to any of the available Finite Element Modeling software (e.g., CODE_BRIGHT or COMSOL) and used to study the slope behavior.
5. The variation of permeability with water content of the unsaturated soil should be experimentally derived to verify the HCF computed using the method of Kunze et al. (1968).

REFERENCES

Acikel, A. S., and Mancuso, C. (2010). "*Use of CO2 gas to improve saturation of high capacity tensiometer (HCT).*"

Alonso, E. E., Gens, A., and Delahaye, C. H. (2003). "Influence of rainfall on the deformation and stability of a slope in overconsolidated clays: a case study." *Hydrogeology journal*, 11(1): 174–192.

Alonso, E. E., Gens, A., and Josa, A. (1990). "A constitutive model for partially saturated soils." *Géotechnique*, 40(3): 405–430.

Au, S. W. C. (1998). "Rain-induced slope instability in Hong Kong." *Engineering Geology*, 51(1): 1–36.

Baum, R. L., and Godt, J. W. (2010). "Early warning of rainfall-induced shallow landslides and debris flows in the USA." *Landslides*, 7(3): 259–272.

Van Bavel, C. H. M., and Hillel, D. I. (1976). "Calculating potential and actual evaporation from a bare soil surface by simulation of concurrent flow of water and heat." *Agricultural Meteorology*, 17(6): 453–476.

Bishop, A. W. (1955). "The use of the slip circle in the stability analysis of slopes." *Geotechnique*, 5(1): 7–17.

Bishop, A. W., Alpan, I., Blight, G. E., and Donald, I. B. (1960). "Factors controlling the strength of partly saturated cohesive soils." Transportation Research Record: Journal of the Transportation Research Board.

Bishop, A. W., and Blight, G. E. (1963). "Some aspects of effective stress in saturated and partly saturated soils." *Géotechnique*, 13(3): 177–197.

Bishop, A. W., and Donald, I. B. (1961). "The experimental study of partly saturated soil in the triaxial apparatus." *Proceedings of the 5th international conference on soil mechanics and foundation engineering, Paris*, 13–21.

Brutsaert, W. (1975). “On a derivable formula for long-wave radiation from clear skies.” *Water resources research*, 11(5): 742–744.

Buisson, M. S. R. and Wheeler, S. J. (2000). “Inclusion of hydraulic hysteresis in a new elasto-plastic framework for unsaturated soils.” *Experimental evidence and theoretical approaches in unsaturated soils*, (2000):109– 119.

Burman, R. D., Jensen, M., and Allen, R. G. (1987). “Thermodynamic factors in evapotranspiration.” *Irrigation Systems for the 21st Century*, 140–148.

Cabarkapa, Z., and Cuccovillo, T. (2005). “Automated triaxial apparatus for testing unsaturated soils.” *Geotechnical Testing Journal*, 29(1): 21–29.

Cai, F., and Ugai, K. (2004). “Numerical analysis of rainfall effects on slope stability.” *International Journal of Geomechanics*, 4(2): 69–78.

De Campos, T. M. P., and Carrillo, C. W. (1995). “Direct shear testing on an unsaturated soil from Rio de Janeiro.” *Proceeding of thr 1st international conference on unsaturated soils (USAT95), Paris, France*, 1995:1.

Capparelli, G., and Tiranti, D. (2010). “Application of the MoniFLaIR early warning system for rainfall-induced landslides in Piedmont region (Italy).” *Landslides*, 7(4): 401–410.

Carlquist, S. (1970). “Hawaii: A Natural History: Geology.” *Climate, Native Flora and Fauna Above the Shoreline*.

Casagrande, A., and Fadum, R. E. (1940). “Notes on soil testing for engineering purposes.”

Cascini, L., Cuomo, S., Pastor, M., and Sorbino, G. (2009). “Modeling of rainfall-induced shallow landslides of the flow-type.” *Journal of Geotechnical and Geoenvironmental Engineering*, 136(1): 85–98.

Chen, H., Dadson, S., and Chi, Y.-G. (2006). “Recent rainfall-induced landslides and debris flow in northern Taiwan.” *Geomorphology*, 77(1–2): 112–125.

Chen, W. F. (2013). *Limit analysis and soil plasticity*.

Chow, V. T., Maidment, D. R., and Mays, L. W. (1988). *Applied hydrology*.

Cox, D. W. (1978). "Volume change of compacted clay fill. Clay fills." *Proceedings of the conference held at the institution of Civil Engineers*, (1978): 14–15.

D'onza, F., Gallipoli, D., Wheeler, S., Casini, F., Vaunat, J., Khalili, N., Laloui, L., Mancuso, C., Masin, D., Nuth, M., Pereira, J. M., and Vassallo, R. (2011). "Benchmark of constitutive models for unsaturated soils." *Géotechnique*, 61(4): 283–302.

Deb, S. K., and El-Kadi, A. I. (2009). "Susceptibility assessment of shallow landslides on Oahu, Hawaii, under extreme-rainfall events." *Geomorphology*, 108(3–4): 219–233.

Dineen, K., and Burland, J. B. (1995). "A new approach to osmotically controlled oedometer testing." *Proceedings f the 1st international conference on unsaturated soils (UNSAT95), Paris, France*, 1995: 2.

Dingman, S. L. (2008). *Physical Hydrology*, (reissued).

Duncan, J. M., and Wrigth, S. G. (2005). *Soil strength and slope stability*.

Eckel, E. B. (1958). *Landslides and engineering practice*.

Eichenberger, J., Ferrari, A., and Laloui, L. (2013). "Early warning thresholds for partially saturated slopes in volcanic ashes." *Computers and Geotechnics*, 49: 79–89.

Engott, J. A., Johnson, A. G., Bassiouni, M., Izuka, S. K., and Rotzoll, K. (2017). *Spatially distributed groundwater recharge for 2010 land cover estimated using a water-budget model for the Island of O 'ahu, Hawai 'i*. US Geological Survey.

Escario, V. (1980). "Suction controlled penetration and shear tests." *Expansive Soils*, ASCE: 781–797.

Escario, V., Juca, J. F. T., and Coppe, M. S. (1989). "Proceeding of the 12th International Conference on Soil Mechanics and Foundation Engineering."

Escario, V., and Saez, J. (1973). "Measurement of the properties of swelling and collapsing soils

under controlled suction." *Proceeding of the 3rd international conference on expansive soils, Haifa*, 195–200.

Escario, V., and Saez, J. (1986). "The shear strength of partly saturated soils." *Géotechnique*, 36(3).

Feddes, R. A., Kabat, P., Van Bakel, Pjt., Bronswijk, J. J. B., and Halbertsma, J. (1988). "Modelling soil water dynamics in the unsaturated zone-state of the art." *Journal of Hydrology*, 100(1–3): 69–111.

Fredlund, D. G. (1979). "Second Canadian Geotechnical Colloquium: Appropriate concepts and technology for unsaturated soils." *Canadian Geotechnical Journal*, 16(1): 121–139.

Fredlund, D. G., and Morgenstern, N. R. (1976). "Constitutive relations for volume change in unsaturated soils." *Canadian Geotechnical Journal*, 13(3): 261–276.

Fredlund, D. G., and Morgenstern, N. R. (1977). "Stress state variables for unsaturated soils." *Journal of Geotechnical and Geoenvironmental Engineering*, 1977(103): 12919.

Fredlund, D. G., and Morgenstern, N. R. (1978). "Stress state variables for unsaturated soils." *Journal of Geotechnical and Geoenvironmental Engineering*, 1978(104): 14170.

Fredlund, D. G., Morgenstern, N. R., and Widger, R. A. (1978). "The shear strength of unsaturated soils." *Canadian Geotechnical Journal*, 15(3): 313–321.

Fredlund, D. G., and Rahardjo, H. (1993). *Soil mechanics for unsaturated soils*.

Fredlund, D. G., and Xing, A. (1994). "Equations for the soil-water characteristic curve." *Canadian geotechnical journal*, 31(4): 521–532.

Fredlund, D. G., Xing, A., Fredlund, M. D., and Barbour, S. L. (1996). "The relationship of the unsaturated soil shear to the soil-water characteristic curve." *Canadian Geotechnical Journal*, 33(3): 440–448.

Fuchs, M., and Hadas, A. (1972). "The heat flux density in a non-homogeneous bare loessial soil." *Boundary-layer meteorology*, 3(2): 191–200.

Gallage, C., and Uchimura, T. (2010). “Investigation on parameters used in warning systems for rain-induced embankment instability.” *Proceedings from the 63rd Canadian Geotechnical Conference (GEO2010),* Calgary, 1025–1031.

Gallipoli, D., Gens, A., Sharma, R., and Vaunat, J. (2003a). “An elasto-plastic model for unsaturated soil incorporating the effects of suction and degree of saturation on mechanical behaviour.” *Géotechnique.*, 53(1): 123–136.

Gallipoli, D., Wheeler, S. J., and Karstunen, M. (2003b). “Modelling the variation of degree of saturation in a deformable unsaturated soil.” *Géotechnique.,* 53(1): 105–112.

Gan, J. K. M., Fredlund, D. G., and Rahardjo, H. (1988). “Determination of the shear strength parameters of an unsaturated soil using the direct shear test.” *Canadian Geotechnical Journal,* 25(3): 500–510.

Gan, K. J., and Fredlund, D. G. (1988). “Multistage Direct Shear Testing of Unsaturated Soils.” *Geotechnical Testing Journal,* 11(2): 132–138.

Garven, E. A., and Vanapalli, S. K. (2006). “Evaluation of empirical procedures for predicting the shear strength of unsaturated soils.” *Unsaturated Soils 2006*: 2570–2592.

Gasmo, J. M., Rahardjo, H., and Leong, E. C. (2000). “Infiltration effects on stability of a residual soil slope.” *Computers and geotechnics,* 26(2): 145–165.

Gens, A. (1996). “Constitutive modelling: application to compacted soils.” *Proceedings f the 1st international conference on unsaturated soils (UNSAT95), Paris, France,* 1995: 3.

Gens, A., Sánchez, M., and Sheng, D. (2006). “On constitutive modelling of unsaturated soils.” *Acta Geotechnica,* 1(3): 137.

Georgetti, G. B., and Vilar, O. M. (2011). “Constant water content triaxial compression tests with a compacted soil.” *Proceedings of the international conference on unsaturated soils* .

Giambelluca, T. W., Shuai, X., Barnes, M. L., Alliss, R. J., Longman, R. J., Miura, T., Chen, Q., Frazier, A. G., Mudd, R. G., and Cuo, L. (2014). “Evapotranspiration of Hawai ‘i.” *Final*

report submitted to the US Army Corps of Engineers—Honolulu District, and the Commission on Water Resource Management, State of Hawai ʻi.

Greco, R., Giorgio, M., Capparelli, G., and Versace, P. (2013). "Early warning of rainfall-induced landslides based on empirical mobility function predictor." *Engineering geology*, 153: 68–79.

Griffiths, D. V, and Lu, N. (2005). "Unsaturated slope stability analysis with steady infiltration or evaporation using elasto-plastic finite elements." *International journal for numerical and analytical methods in geomechanics*, 29(3): 249–267.

Guan, Y., and Fredlund, D. G. (1997). "Use of the tensile strength of water for the direct measurement of high soil suction." *Canadian Geotechnical Journal*, 34(4): 604–614.

Guzzetti, F., Peruccacci, S., Rossi, M., and Stark, C. P. (2008). "The rainfall intensity–duration control of shallow landslides and debris flows: an update." *Landslides*, 5(1): 3–17.

Hamid, T. B., and Miller, G. A. (2009). "Shear strength of unsaturated soil interfaces." *Canadian Geotechnical Journal*, 46(5): 595–606.

Hazlett, R. W., and Hyndman, D. W. (1996). *Roadside Geology of Hawaii*.

Hihara, L. and Sugamoto, R. (2017) "Weather data". *Personal communication. Hawaii Corrosion Laboratory. Department of Mechanical Engineering, University of Hawaii.*

Hilf, J. W. (1956). "An investigation of pore water pressure in compacted cohesive soils."

Ho, D. Y. F., and Fredlund, D. G. (1982). "Increase in strength due to suction for two Hong Kong soils." *Proceedings of the ASCE specialty conference on engineering and construction in tropical and residual soils, Hawaii*, 263–296.

Hoyos Jr, L. R. (1998). "Experimental and computational modeling of unsaturated soil behavior under true triaxial stress states." PhD diss., Georgia Institute of Technology.

Hu, R., Chen, Y. F., Liu, H. H., and Zhou, C. B. (2013). "A water retention curve and unsaturated hydraulic conductivity model for deformable soils: consideration of the change in pore-size

distribution.” *Géotechnique*, 63(16): 1389–1405.

Huang, M., and Jia, C. Q. (2009). “Strength reduction FEM in stability analysis of soil slopes subjected to transient unsaturated seepage.” *Computers and Geotechnics*, 36(1–2): 93–101.

Huang, S., Barbour, S. L., and Fredlund, D. G. (1998). “Development and verification of a coefficient of permeability function for a deformable unsaturated soil.” *Canadian Geotechnical Journal*, 35(3): 411–425.

Huat, B. B. K., Ali, F. H., and Rajoo, R. S. K. (2006). “Stability analysis and stability chart for unsaturated residual soil slope.” *American Journal of Environmental Sciences*, 2(4): 154–160.

Hvorslev, M. J. (1937). “Uber die Festigkeitseigenshaften gestorter bindinger Bode.” *Ingeniorvidenskabelige Skrifter A45*.

Idso, S. B., Aase, J. K., and Jackson, R. D. (1975). “Net radiation-soil heat flux relations as influenced by soil water content variations.” *Boundary-layer meteorology*, 9(1): 113–122.

Iwamoto, M. K. (2018). “A Landslide Warning System For a Soil Slope on Oahu.” PhD Diss. University of Hawaii at Manoa.

Jacobs, J. M., Satti, S. R., and Fitzgerald, J. M. (2001). *Evaluation of reference evapotranspiration methodologies and AFSIRS crop water use simulation model*.

Jaky, J. (1948). “Pressure in silos.” *Proc. 2nd ICSM, 1948*.

Jennings, J. E. B., and Burland, J. B. (1962). “Limitations to the use of effective stresses in partly saturated soils.” *Géotechnique*, 12(2): 125–144.

Josa, A., Alonso, E. E., Lloret, A., and Gens, A. (1987). “Stress-strain behaviour or partially saturated soils.” *European conference on soil mechanics and foundation engineering. 9*: 561–564.

Kanjanakul, C., Chub-uppakarn, T., and Chalermyanont, T. (2016). “Rainfall thresholds for landslide early warning system in Nakhon Si Thammarat.” *Arabian Journal of Geosciences*,

9(11): 584.

Kassiff, G., and Shalom, A. Ben. (1971). “Experimental relationship between swell pressure and suction.” *Géotechnique*, 21(3): 245–255.

Keefer, D. K., Wilson, R. C., Mark, R. K., Brabb, E. E., Brown, W. M., Ellen, S. D., Harp, E. L., Wieczorek, G. F., Alger, C. S., and Zatkin, R. S. (1987). “Real-time landslide warning during heavy rainfall.” *Science*, 238(4829): 921–925.

Khalili, N., and Khabbaz, M. H. (1998). “A unique relationship of chi for the determination of the shear strength of unsaturated soils.” *Geotechnique*, 48(5).

Kohgo, Y., Nakano, M., and Miyazaki, T. (1993). “Theoretical aspects of constitutive modelling for unsaturated soils.” *Soils and foundations*, 33(4); 49–63.

Kohler, M. A., and Parmele, L. H. (1967). “Generalized estimates of free-water evaporation.” *Water Resources Research*, 3(4): 997–1005.

Kunze, R. J., Uehara, G., and Graham, K. (1968). “Factors Important in the Calculation of Hydraulic Conductivity 1.” *Soil Science Society of America Journal*, 32(6): 760–765.

Le, T. M. H., Gallipoli, D., Sánchez, M., and Wheeler, S. (2015). “Stability and failure mass of unsaturated heterogeneous slopes.” *Canadian Geotechnical Journal*, 52(11): 1747–1761.

Le, T. T., Cui, Y. J., Muñoz, J. J., Delage, P., Tang, A. M., and Li, X. L. (2011). “Studying the stress-suction coupling in soils using an oedometer equipped with a high capacity tensiometer.” *Frontiers of Architecture and Civil Engineering in China*, 5(2): 160–170.

Li, L., and Zhang, X. (2014). “Development of a new high-suction tensiometer.” *Soil Behavior and Geomechanics*, 416–425.

Li, L., and Zhang, X. (2015a). “Modified Unconfined Compression Testing System to Characterize Stress-Strain Behavior of Unsaturated Soils at Low Confining Stresses.” *Transportation Research Record: Journal of the Transportation Research Board*, (2510): 54–64.

Li, L., and Zhang, X. (2015b). “A new triaxial testing system for unsaturated soil characterization.” *Geotechnical Testing Journal*, 38(6): 823–839.

Li, L., Zhang, X., and Lin, C. (2015). “Development of an Oedometer Cell with Suction Measurement Ability.” *Innovative Materials and Design for Sustainable Transportation Infrastructure*, 179–188.

Lourenço, S. D. N., Gallipoli, D., Toll, D. G., and Evans, F. D. (2006). “Development of a commercial tensiometer for triaxial testing of unsaturated soils.” *Unsaturated Soils 2006*, 1875–1886.

Lu, N., Şener-Kaya, B., Wayllace, A., and Godt, J. W. (2012). “Analysis of rainfall-induced slope instability using a field of local factor of safety.” *Water Resources Research*, 48(9).

Ma, S., Huang, M., Hu, P., and Yang, C. (2013). “Soil-water characteristics and shear strength in constant water content triaxial tests on Yunnan red clay.” *Journal of Central South University*, 20(5): 1412–1419.

Macdonald, G. A., Abbott, A. T., and Peterson, F. L. (1983). *Volcanoes in the sea: the geology of Hawaii*.

Masin, D. (2010). “Predicting the dependency of a degree of saturation on void ratio and suction using effective stress principle for unsaturated soils.” *International Journal for Numerical and Analytical Methods in Geomechanics*, 34(1): 73–90.

Maswoswe, J. (1985). *Stress paths for compacted soil during collapse due to wetting*.

Matyas, E. L., and Radhakrishna, H. S. (1968). “Volume change characteristics of partially saturated soils.” *Géotechnique*, 18(4): 432–448.

Mbonimpa, M., Aubertin, M., Maqsoud, A., and Bussière, B. (2006). “Predictive model for the water retention curve of deformable clayey soils.” *Journal of Geotechnical and Geoenvironmental Engineering*, 132(9): 1121–1132.

Meilani, I., Rahardjo, H., Leong, E. C., and Fredlund, D. G. (2002). “Mini suction probe for matric

suction measurements." *Canadian Geotechnical Journal*, 39(6): 1427–1432.

Michalowski, R. L. (1995). "Slope stability analysis: a kinematical approach." *Geotechnique,* 45(2): 283–293.

Miller, G. A., and Hamid, T. B. (2006). "Interface direct shear testing of unsaturated soil." *Geotechnical Testing Journal,* 30(3): 182–191.

Miller, T. W., and Hamilton, J. M. (1989). "A new analsis procedure to explain a slope failure at the Martin Lake mine." *Geotechnique,* 39(1): 107–123.

Monteith, J. L., and Unsworth, M. H. (2008). *Principles of Environmental Physics, xxi, 418 p.*

Nam, S., Gutierrez, M., Diplas, P., and Petrie, J. (2011). "Determination of the shear strength of unsaturated soils using the multistage direct shear test." *Engineering Geology,* 122(3): 272–280.

Ng, C., Losso, J. N., Marshall, W. E., and Rao, R. M. (2002). "Freundlich adsorption isotherms of agricultural by-product-based powdered activated carbons in a geosmin–water system." *Bioresource technology,* 85(2): 131–135.

Ng, C. W. W., Cui, Y., Chen, R., and Delage, P. (2007). "The axis-translation and osmotic techniques in shear testing of unsaturated soils: a comparison." *Soils and Foundations,* 47(4): 675–684.

Ng, C. W. W., and Shi, Q. (1998). "A numerical investigation of the stability of unsaturated soil slopes subjected to transient seepage." *Computers and geotechnics,* 22(1): 1–28.

Nicholson, D., Tse, C. M., Penny, C., O Hana, S., and Dimmock, R. (1999). *The observational method in ground engineering: principles and applications*.

Novak, M. D., and Black, T. A. (1983). "The surface heat flux density of a bare soil." *Atmosphere-Ocean,* 21(4): 431-443.

Nuth, M., and Laloui, L. (2008). "Advances in modelling hysteretic water retention curve in deformable soils." *Computers and Geotechnics,* 35(6): 835–844.

Oliveira, O. M. de, and Marinho, F. A. M. (2007). “Suction equilibration time for a high capacity tensiometer.” *Geotechnical Testing Journal*, 31(1): 101–105.

Olivella, S., Gens, A., Carrera, J., and Alonso, E. E. (1996). “Numerical formulation for a simulator (CODE_BRIGHT) for the coupled analysis of saline media.” *Engineering computations*, 13(7): 87–112.

Oloo, S. Y., and Fredlund, D. G. (1996). “A method for determination of φ b for statically compacted soils.” *Canadian Geotechnical Journal*, 33(2): 272–280.

Penman, H. L. (1948). “Natural evaporation from open water, bare soil and grass.” *Proceedings of the Royal Society of London. Series A. Mathematical and Physical Sciences*, 193(1032): 120–145.

Peterson, D. M., Ellen, S. D., and Knifong, D. L. (1993). *Distribution of past debris flows and other rapid slope movements from natural hillslopes in the Honolulu District of Oahu, Hawaii*.

Price, V. E., and Morgenstern, N. R. (1965). “The analysis of the stability of general slip surfaces.” Geotechnique, 19(1): 159

Rahardjo, H., Heng, O. B., and Choon, L. E. (2004). “Shear strength of a compacted residual soil from consolidated drained and constant water content triaxial tests.” *Canadian Geotechnical Journal*, 41(3): 421–436.

Rahardjo, H., and Leong, E. C. (2006). “Suction measurements.” *Unsaturated Soils*, 2006: 81-104.

Rahardjo, H., Nio, A. S., Leong, E. C., and Song, N. Y. (2010). “Effects of groundwater table position and soil properties on stability of slope during rainfall.” *Journal of geotechnical and geoenvironmental engineering*, 136(11): 1555–1564.

Rahardjo, H., Ong, T. H., Rezaur, R. B., and Leong, E. C. (2007). “Factors controlling instability of homogeneous soil slopes under rainfall.” *Journal of Geotechnical and Geoenvironmental Engineering*, 133(12): 1532–1543.

Rahardjo, H., Satyanaga, A., and Leong, E. C. (2013). “Effects of flux boundary conditions on pore-water pressure distribution in slope.” *Engineering geology*, 165: 133–142.

Rahimi, A., Rahardjo, H., and Leong, E. C. (2010). “Effect of antecedent rainfall patterns on rainfall-induced slope failure.” *Journal of Geotechnical and Geoenvironmental Engineering*, 137(5): 483-491.

Ridley, A. M. (2002). “Stress-strain and strength relationships for a reconstituted clayey silt.” *Unsaturated Soils: Proceedings of the Third International Conference on Unsaturated Soils, UNSAT 2002, Recife, Brazil*.

Ridley, A. M., and Burland, J. B. (1993). “A new instrument for the measurement of soil moisture suction.” *Géotechnique*, 43(2): 321–324.

Ridley, A. M., Dineen, K., Burland, J. B., and Vaughan, P. R. (2003). “Soil matrix suction: some examples of its measurement and application in geotechnical engineering.” *Géotechnique*, 53(2): 241–253.

Rodríguez, R., Sanchez, M., Ledesma, A., and Lloret, A. (2007). “Experimental and numerical analysis of desiccation of a mining waste.” *Canadian Geotechnical Journal*, 44(6): 644–658.

Romero, E., Lloret, A., and Gens, A. (1995). “Development of a new suction and temperature controlled oedometer cell.” *Proceedings f the 1st international conference on unsaturated soils (UNSAT95), Paris, France*, 1995: 2.

Romero, E., and Vaunat, J. (2014). “Retention curves of deformable clays.” *Experimental evidence and theoretical approaches in unsaturated soils*, 99–114.

Roscoe, K., and Burland, J. B. (1968). *On the generalized stress-strain behaviour of wet clay.*

Rutqvist, J., Barr, D., Datta, R., Gens, A., Millard, A., Olivella, S., Tsang, C. F., and Tsang, Y. (2005). “Coupled thermal–hydrological–mechanical analyses of the Yucca Mountain Drift Scale Test-Comparison of field measurements to predictions of four different numerical models.” *International Journal of Rock Mechanics and Mining Sciences*, 42(5): 680–697.

Sánchez, M., Gens, A., do Nascimento Guimarães, L., and Olivella, S. (2005). "A double structure generalized plasticity model for expansive materials." *International Journal for Numerical and Analytical Methods in Geomechanics*, 29(8): 751–787.

Sarma, S. K. (1973). "Stability analysis of embankments and slopes." *Geotechnique*, 23(3): 423–433.

Satija, B. Sen. (1978). *Shear behaviour of partially saturated soils.*

Sharma, R. S. (1998). "Mechanical behaviour of unsaturated highly expansive clays." PhD diss. University of Oxford.

Sheng, D., Fredlund, D. G., and Gens, A. (2008a). "A new modelling approach for unsaturated soils using independent stress variables." *Canadian Geotechnical Journal*, 45(4): 511–534.

Sheng, D., Fredlund, D. G., and Gens, A. (2008b). "A new modelling approach for unsaturated soils using independent stress variables." *Canadian Geotechnical Journal*, 45(4): 511–534.

Sheng, D., Sloan, S. W., and Gens, A. (2004). "A constitutive model for unsaturated soils: thermomechanical and computational aspects." *Computational Mechanics*, 33(6): 453–465.

Sheng, D., and Zhou, A. N. (2011). "Coupling hydraulic with mechanical models for unsaturated soils." *Canadian Geotechnical Journal*, 48(5): 826–840.

Sidle, R., and Ochiai, H. (2006). "Processes, prediction, and land use." *Water resources monograph. American Geophysical Union, Washington*.

Simms, P. H., and Yanful, E. K. (2005). "A pore-network model for hydromechanical coupling in unsaturated compacted clayey soils." *Canadian Geotechnical Journal*, 42(2): 499–514.

Simunek, J., Van Genuchten, M. T., and Sejna, M. (2006). "The HYDRUS software package for simulating the two-and three-dimensional movement of water, heat, and multiple solutes in variably-saturated media." *Technical manual*, 1.

Sivakumar, V. (1993). "A critical state framework for unsaturated soil." PhD diss. University of Sheffield.

Spencer, E. (1967). “A method of analysis of the stability of embankments assuming parallel inter-slice forces.” *Geotechnique*, 17(1): 11–26.

Sun, D. A., Cui, H. B., Matsuoka, H., and Sheng, D. C. (2007a). “A three-dimensional elastoplastic model for unsaturated compacted soils with hydraulic hysteresis.” *Soils and Foundations*, 47(2): 253–264.

Sun, D. A., Sheng, D. C., Cui, H. B., and Sloan, S. W. (2007b). “A density-dependent elastoplastic hydro-mechanical model for unsaturated compacted soils.” *International journal for numerical and analytical methods in geomechanics*, 31(11): 1257–1279.

Sun, D., Sun, W., and Xiang, L. (2010). “Effect of degree of saturation on mechanical behaviour of unsaturated soils and its elastoplastic simulation.” *Computers and Geotechnics*, 37(5): 678-688.

Sun, Q., Zhang, L., Ding, X., Hu, J., and Liang, H. (2015). “Investigation of slow-moving landslides from ALOS/PALSAR images with TCPInSAR: A case study of Oso, USA.” *Remote Sensing*, 7(1): 72–88.

Take, W. A., and Bolton, M. D. (2003). “Tensiometer saturation and the reliable measurement of soil suction.” *Géotechnique*, 53(2): 159–172.

Tamagnini, R. (2004). “An extended Cam-clay model for unsaturated soils with hydraulic hysteresis.” *Géotechnique*, 54(3): 223–228.

Tarantino, A. (2009). “A water retention model for deformable soils.” *Géotechnique*, 59(9): 751–762.

Tarantino, A., and Mongiovi, L. (2003). “Calibration of tensiometer for direct measurements of matric suction.” *Géotechnique*, 53(1).

Taylor, D. W. (1948). *Fundamentals of Soil Mechanics.*

Thiebes, B., Bell, R., Glade, T., Jäger, S., Mayer, J., Anderson, M., and Holcombe, L. (2014). “Integration of a limit-equilibrium model into a landslide early warning system.” *Landslides*,

11(5): 859–875.

Thu, T. M., Rahardjo, H., and Leong, E. C. (2006). “Shear strength and pore-water pressure characteristics during constant water content triaxial tests.” *Journal of Geotechnical and Geoenvironmental Engineering*, 132(3): 411–419.

Torikai, J. D., and Wilson, R. C. (1992). *Hourly rainfall and reported debris flows for selected storm periods, 1935-91, in and near the Honolulu District, Hawaii*. US Geological Survey; Books and Open-File Reports Section [distributor].

Tsaparas, I., Rahardjo, H., Toll, D. G., and Leong, E. C. (2002). “Controlling parameters for rainfall-induced landslides.” *Computers and geotechnics*, 29(1): 1–27.

Turner, A. K., and Schuster, R. L. (1996). “Socioeconomic significance of landslides. Landslides: Investigation and Mitigation. Special Report, National Research Council US.” *Transportation Research Board*, 247.

Universitat Politecnica de Catalunya. (2017). CODE_BRIGHT Users Guide. Version 7.4. https://deca.upc.edu/en/projects/code_bright/downloads/users_guide/view.

Van Genuchten, M. T. (1980). “A closed-form equation for predicting the hydraulic conductivity of unsaturated soils 1.” *Soil science society of America journal*, 44(5): 892–898.

Vanapalli, S. K., Fredlund, D. G., Pufahl, D. E., and Clifton, A. W. (1996a). “Model for the prediction of shear strength with respect to soil suction.” *Canadian Geotechnical Journal*, 33(3): 379–392.

Vanapalli, S. K., Fredlund, D. G., Pufahl, D. E., and Clifton, A. W. (1996b). “Model for the prediction of shear strength with respect to soil suction.” *Canadian Geotechnical Journal*, 33(3): 379–392.

Vanapalli, S. K., and Lane, J. J. (2002). “A simple technique for determining the shear strength of finegrained unsaturated soils using the conventional direct shear apparatus.” *Proc. Second Canadian Specialty Conference on Computer Applications in Geotechnique, Winnipeg*, 245–253.

Vaunat, J., Romero, E., and Jommi, C. (2000). "An elastoplastic hydromechanical model for unsaturated soils." *Experimental evidence and theoretical approaches in unsaturated soils*, 20(0): 0.

Wheeler, S. J. (1988). "The undrained shear strength of soils containing large gas bubbles." *Géotechnique*, 38(3): 399–413.

Wheeler, S. J., and Karube, D. (1996). "Constitutive modelling." *Proceedings of the 1st international conference on unsaturated soils (UNSAT95), Paris, France,* 1995:3.

Wheeler, S. J., Sharma, R. S., and Buisson, M. S. R. (2003). "Coupling of hydraulic hysteresis and stress--strain behaviour in unsaturated soils." *Géotechnique*, 53(1): 41–54.

Wheeler, S. J., Sharma, R. S., and Buisson, M. S. R. (2004). "Coupling of hydraulic hysteresis and stress–strain behaviour in unsaturated soils." *Géotechnique,* 53(1): 41–54.

Wheeler, S. J., and Sivakumar, V. (1993). "Development and application of a critical state model for unsaturated soil." *Predictive soil mechnics proceedings of the worth memorial symposium, Oxford*.

Wilson, R. C. (1992). "Development of rainfall warning threshold for debris flows in Honolulu District, Oahu." *US Geological Survey Open-File Report,* 92–521.

Yu, H. S., Salgado, R., Sloan, S. W., and Kim, J. M. (1998). "Limit analysis versus limit equilibrium for slope stability." *Journal of Geotechnical and Geoenvironmental Engineering*, 124(1): 1–11.

Zhang, J., Li, J., and Lin, H. (2018). "Models and influencing factors of the delay phenomenon for rainfall on slope stability." *European Journal of Environmental and Civil Engineering*, 22(1): 122–136.

Zhang, X. (2015). "Constitutive Modeling of Unsaturated Soils Using Results from Suction Controlled Odometer Tests." In *IFCEE, 2015*: 2075–2083.

Zhang, X. (2016). "Limitations of suction-controlled triaxial tests in the characterization of

unsaturated soils." *International Journal for Numerical and Analytical Methods in Geomechanics*, 40(2): 269–296.

Zhang, X., Alonso, E. E., and Casini, F. (2016a). "Explicit formulation of at-rest coefficient and its role in calibrating elasto-plastic models for unsaturated soils." *Computers and Geotechnics*, 71: 56–68.

Zhang, X., Lu, H., and Li, L. (2016b). "Use of Oedometer Equipped with High-Suction Tensiometer to Characterize Unsaturated Soils." *Transportation Research Record: Journal of the Transportation Research Board*, (2578): 58–71.

Zhang, X., and Lytton, R. L. (2009a). "Modified state-surface approach to the study of unsaturated soil behavior. Part II: General formulation." *Canadian Geotechnical Journal*, 46(5): 553–570.

Zhang, X., and Lytton, R. L. (2009b). "Modified state-surface approach to the study of unsaturated soil behavior. Part I: Basic concept." *Canadian Geotechnical Journal*, 46(5): 536–552.

Zhang, X., and Lytton, R. L. (2011). "Modified state-surface approach to the study of unsaturated soil behavior. Part III: Modeling of coupled hydromechanical effect." *Canadian Geotechnical Journal*, 49(1): 98–120.

Zhou, A. N., Sheng, D., and Carter, J. P. (2012). "Modelling the effect of initial density on soil-water characteristic curves." *Géotechnique*, 62(8): 669–680.

Zhou, A., and Sheng, D. (2009). "Yield stress, volume change, and shear strength behaviour of unsaturated soils: validation of the SFG model." *Canadian Geotechnical Journal*, 46(9): 1034–1045.

APPENDIX A OEDOMETER COMPRESSION TEST RESULTS

Sample 5, Oedometer compression specimen 3, w=26.19%			
Normal stress (kPa)	H (mm)	Suction (kPa)	Specific v
1.2	25.50	-	2.085
29.5	25.38	353.6	2.075
58.9	25.30	349.4	2.069
117.8	25.25	342	2.064
235.6	25.10	321.7	2.053
353.5	24.94	298	2.039
471.3	24.81	274.5	2.028
706.9	24.59	237.2	2.010
942.6	24.38	214.5	1.993
1178.2	24.18	198.1	1.977
29.5	24.52	279.3	2.005

Sample 4, Oedometer compression specimen 2, w=29.84%			
Normal stress (kPa)	H (mm)	Suction (kPa)	Specific v
1.0	25.30	-	2.081
29.0	25.22	325.7	2.075
57.9	25.17	300.9	2.070
115.8	25.04	266.4	2.060
231.7	24.83	214.5	2.042
463.3	24.46	140.2	2.012
926.7	23.46	9.9	1.930
29.0	23.88	193.7	1.964

Sample 5, Oedometer compression specimen 2, w=30.09%			
Normal stress (kPa)	H (mm)	Suction (kPa)	Specific v
1.2	25.50	-	2.026
29.5	25.40	224.9	2.018
58.9	25.34	212.1	2.014
117.8	25.18	184.4	2.001
235.6	24.94	135.3	1.982
353.5	24.76	96.2	1.967
471.3	24.58	62.5	1.953
589.1	24.42	31.7	1.941
706.9	24.28	0	1.929
29.5	24.57	113.1	1.952

Sample 5, Oedometer compression specimen 1, w=33.56%			
Normal stress (kPa)	H (mm)	Suction (kPa)	Specific v
1.2	26.00	117.2	2.116
29.0	25.88	106.5	2.106
57.9	25.81	100.8	2.101
115.8	25.66	87.5	2.088
231.7	25.40	58.3	2.068
347.5	25.17	38.4	2.049
463.3	24.95	17.7	2.031
695.0	24.55	8.8	1.998
29.0	24.98	49.4	2.033

Sample 4, Oedometer compression specimen 1, w=34.23%			
Normal stress (kPa)	H (mm)	Suction (kPa)	Specific v
1.0	26.00	155.2	2.145
29.0	25.60	136.4	2.112
57.9	25.45	120.2	2.099
115.8	25.23	94.8	2.082
231.7	24.90	62.6	2.055
463.3	24.41	7.6	2.014
926.7	23.61	0	1.948
29.0	24.23	81.5	1.999

Sample 6, Oedometer compression specimen 1, w=34.64%			
Normal stress (kPa)	H (mm)	Suction (kPa)	Specific v
1.2	26.00	108.8	2.153
29.0	25.87	98.2	2.143
57.9	25.79	90.6	2.136
115.8	25.66	78.7	2.125
231.7	25.43	54.3	2.106
347.5	25.23	31.1	2.090
463.3	25.04	6.6	2.074
579.2	24.86	-1	2.059
29.0	25.24	57.1	2.090
1.2	26.00	108.8	2.153

Sample 2, Oedometer compression specimen 1, w=35.81%			
Normal stress (kPa)	H (mm)	Suction (kPa)	Specific v
1.0	24.40	-	2.280
29.0	24.10	386.3	2.252
57.9	24.05	361.4	2.247
115.8	23.92	307.1	2.235
231.7	23.59	214.6	2.204
463.3	22.87	94.6	2.137
926.7	21.58	0.2	2.016
29.0	21.85	182	2.041
1.0	21.92	205	2.048

Sample 3, Oedometer compression specimen 1, w=46.04%			
Normal stress (kPa)	H (mm)	Suction (kPa)	Specific v
1.0	26.00	-	2.485
29.0	25.93	56.3	2.478
57.9	25.86	50.3	2.471
115.8	25.70	40.9	2.456
231.7	25.34	27.4	2.422
463.3	24.79	1.68	2.369
926.7	23.89	0.7	2.283
29.0	24.46	13	2.337

APPENDIX B DIRECT SHEAR TEST RESULTS

Sample 1, direct shear specimen 1, w=30.32%, normal load = 463 kPa					
Displacement (mm)	H (mm)	Suction (kPa)	Shear load (N)	Stress (kPa)	Specific v
0	25.28	58.7	0	0.0	2.191
0.25	25.30	58.9	0	0.0	2.193
0.5	25.30	59.8	15.1	5.5	2.193
0.75	25.27	62.2	69.7	25.5	2.190
1	25.26	68.6	157.5	57.6	2.189
1.25	25.24	75.3	254.5	93.1	2.188
1.5	25.22	78.4	312.0	114.1	2.186
1.75	25.21	82.1	372.6	136.3	2.185
2	25.20	90	454.4	166.2	2.184
2.25	25.18	98.6	518.0	189.5	2.183
2.5	25.16	107.3	563.4	206.1	2.181
2.75	25.14	115	602.8	220.5	2.179
3	25.11	121	633.1	231.6	2.177
3.25	25.08	126.2	660.4	241.5	2.174
3.5	25.04	132	675.5	247.1	2.171
3.75	25.01	136.4	687.7	251.5	2.167
4	24.97	140.2	702.8	257.1	2.165
4.25	24.93	146.8	724.0	264.8	2.161
4.5	24.89	155.5	742.2	271.5	2.157
4.75	24.86	164	757.3	277.0	2.155
5	24.83	171.3	775.5	283.7	2.152
5.25	24.80	182	787.6	288.1	2.150
5.5	24.78	197.7	793.7	290.3	2.148
5.75	24.76	206	802.8	293.6	2.146
6	24.74	211.5	805.8	294.7	2.144
6.25	24.71	215.6	808.8	295.8	2.142
6.5	24.69	222.2	817.9	299.2	2.140
6.75	24.67	227.5	827.0	302.5	2.138
7	24.64	230	833.1	304.7	2.136
7.25	24.62	231.2	839.1	306.9	2.134
7.5	24.60	233	845.2	309.1	2.132
7.75	24.58	235.4	845.2	309.1	2.130
8	24.56	238.9	845.2	309.1	2.128

Sample 1, direct shear specimen 2, w=29.10%, normal load = 139 kPa					
Displacement (mm)	H (mm)	Suction (kPa)	Shear load (N)	Stress (kPa)	Specific v
0	25.48	403	0	0.0	2.209
0.35	25.48	401.7	36.9	13.5	2.209
0.7	25.46	392.5	99.2	36.3	2.206
1.05	25.44	381.5	110.6	40.4	2.205
1.4	25.44	370.1	148.8	54.4	2.205
1.75	25.44	357	212.6	77.8	2.205
2.1	25.45	338.5	266.5	97.5	2.206
2.45	25.47	318.7	326.0	119.3	2.207
2.8	25.50	301.7	381.3	139.5	2.210
3.15	25.50	286.2	428.1	156.6	2.210
3.5	25.55	276.3	470.6	172.1	2.215
3.85	25.61	269.8	510.3	186.7	2.220
4.2	25.71	221.6	484.8	177.3	2.228
4.55	25.77	224.7	467.8	171.1	2.234
4.9	25.83	221.6	467.8	171.1	2.239

Sample 2, direct shear specimen 1, w=35.81%, normal load = 463 kPa					
Displacement (mm)	H (mm)	Suction (kPa)	Shear load (N)	Stress (kPa)	Specific v
0	22.82	83.4	0	0.0	2.132
0.5	22.82	83.2	6.1	2.2	2.132
1	22.82	83.2	15.1	5.5	2.132
1.5	22.80	83.1	136.3	49.9	2.131
2	22.79	82.8	348.4	127.4	2.129
2.5	22.73	79.3	445.3	162.9	2.124
3	22.70	71.64	499.8	182.8	2.121
3.5	22.67	53.7	560.4	205.0	2.118
4	22.63	24.4	599.8	219.4	2.115
4.5	22.60	8.12	630.1	230.5	2.111
5	22.57	-4.7	651.3	238.2	2.109
5.5	22.54	-13	663.4	242.7	2.106
6	22.52	-16.7	672.5	246.0	2.104
6.5	22.50	-17.6	681.6	249.3	2.102
7	22.49	-17.9	687.7	251.5	2.101
7.5	22.47	-17	693.7	253.7	2.099
8	22.45	-7.8	699.8	256.0	2.097
8.5	22.44	-1.5	699.8	256.0	2.097
9	22.44	3	696.7	254.8	2.096

Sample 2, direct shear specimen 2, w=38.34%, normal load = 236 kPa					
Displacement (mm)	H (mm)	Suction (kPa)	Shear load (N)	Stress (kPa)	Specific v
0	25.45	87.9	0	0.0	2.204
0.25	25.45	87.9	9.1	3.3	2.204
0.5	25.45	88.4	42.4	15.5	2.204
0.75	25.45	91.1	112.1	41.0	2.204
1	25.44	96.7	227.2	83.1	2.203
1.25	25.41	100	302.9	110.8	2.200
1.5	25.37	104.3	360.5	131.9	2.197
1.75	25.36	113.9	418.0	152.9	2.195
2	25.34	126.7	463.5	169.5	2.194
2.25	25.33	134	484.7	177.3	2.193
2.5	25.32	137.7	499.8	182.8	2.192
2.75	25.31	132.5	505.9	185.0	2.191
3	25.29	128.9	507.4	185.6	2.190
3.25	25.27	130	505.9	185.0	2.188
3.5	25.25	135.3	502.9	183.9	2.186

Sample 2, direct shear specimen 3, w=41.38%, normal load = 116 kPa					
Displacement (mm)	H (mm)	Suction (kPa)	Shear load (N)	Stress (kPa)	Specific v
0	25.74	47.9	0	0.0	2.228
0.25	25.73	47.2	27.3	10.0	2.227
0.5	25.72	43	72.7	26.6	2.226
0.75	25.71	33.6	115.1	42.1	2.225
1	25.69	28.4	154.5	56.5	2.224
1.25	25.66	22.6	184.8	67.6	2.221
1.5	25.63	20.4	206.0	75.3	2.219
1.75	25.62	18.6	215.1	78.7	2.217
2	25.61	18.6	221.1	80.9	2.216
2.25	25.60	15.77	221.1	80.9	2.216
2.5	25.58	11.73	218.1	79.8	2.214

Sample 2, direct shear specimen 4, w=41.23%, normal load = 58 kPa					
Displacement (mm)	H (mm)	Suction (kPa)	Shear load (N)	Stress (kPa)	Specific v
0	25.84	87	0	0.0	2.235
0.25	25.82	87.2	0.0	0.0	2.233
0.5	25.81	88.8	27.3	10.0	2.233
0.75	25.80	94.9	75.7	27.7	2.232
1	25.80	97.6	136.3	49.9	2.232
1.25	25.79	87	178.7	65.4	2.231
1.5	25.79	77.1	209.0	76.5	2.231
1.75	25.79	73.7	218.1	79.8	2.231
2	25.79	71.1	212.1	77.6	2.231
2.25	25.79	62.6	196.9	72.0	2.231

Sample 3, direct shear specimen 1, w=44.23%, normal load = 232 kPa					
Displacement(mm)	H (mm)	Suction (kPa	Shear load (N)	Stress (kPa)	Specific v
0	24.21	18.9	0	0.0	2.313
0.25	24.20	18.4	42.4	15.5	2.312
0.5	24.18	16.99	136.3	49.9	2.310
0.75	24.17	16.5	166.6	60.9	2.309
1	24.16	16.22	227.2	83.1	2.309
1.25	24.16	16.3	327.2	119.7	2.309
1.5	24.16	17.2	390.8	142.9	2.309
1.75	24.17	19	442.3	161.8	2.309
2	24.17	20.5	466.5	170.6	2.310
2.25	24.18	22.8	469.5	171.7	2.310
2.5	24.18	24.2	472.6	172.9	2.310
2.75	24.18	25.6	469.5	171.7	2.310

Sample 3, direct shear specimen 3, w=32.00%, normal load = 463 kPa					
Displacement (mm)	H (mm)	Suction (kPa)	Shear load (N)	Stress (kPa)	Specific v
0	25.50	649.4	0.0	0.0	1.991
0.25	25.49	636.3	109.1	39.9	1.990
0.5	25.47	604.1	239.3	87.5	1.989
0.75	25.45	573.6	354.4	129.6	1.987
1	25.43	544	451.4	165.1	1.985
1.25	25.41	518.7	530.1	193.9	1.984
1.5	25.41	496	590.7	216.1	1.984
1.75	25.41	476.1	678.6	248.2	1.984
2	25.41	456	754.3	275.9	1.984
2.25	25.41	436	814.9	298.1	1.984
2.5	25.41	413	863.4	315.8	1.984
2.75	25.41	393	905.8	331.3	1.984
3	25.40	371	930.0	340.2	1.983
3.25	25.39	353	942.1	344.6	1.983
3.5	25.39	335	948.2	346.8	1.982
3.75	25.38	322	954.2	349.0	1.982
4	25.38	310	963.3	352.4	1.981
4.25	25.36	291	972.4	355.7	1.980
4.5	25.36	282	975.4	356.8	1.980
4.75	25.36	300	972.4	355.7	1.980

Sample 4, direct shear specimen 1, w=32.43%, normal load = 116 kPa					
Displacement (mm)	H (mm)	Suction (kPa)	Shear load (N)	Stress (kPa)	Specific v
0	23.94	81.5	0	0.0	1.973
0.25	23.94	81.9	6.1	2.2	1.973
0.5	23.92	82.1	48.5	17.7	1.971
0.75	23.90	82.3	90.9	33.2	1.970
1	23.88	82.5	136.3	49.9	1.968
1.25	23.87	82.9	175.7	64.3	1.968
1.5	23.88	83.1	215.1	78.7	1.968
1.75	23.85	83.2	257.5	94.2	1.966
2	23.86	83.6	302.9	110.8	1.966
2.25	23.89	83.7	345.3	126.3	1.969
2.5	23.91	83.7	360.5	131.9	1.971
2.75	23.93	84	369.6	135.2	1.973
3	23.95	84.6	366.5	134.1	1.974

Sample 4, direct shear specimen 2, w=33.72%, normal load = 58 kPa					
Displacement (mm)	H (mm)	Suction (kPa)	Shear load (N)	Stress (kPa)	Specific v
0	25.50	144.4	0.0	0.0	2.006
0.25	25.50	144.7	9.1	3.3	2.006
0.5	25.48	146.2	45.4	16.6	2.005
0.75	25.47	147.2	112.1	41.0	2.004
1	25.46	135.3	175.7	64.3	2.003
1.25	25.45	126.8	218.1	79.8	2.002
1.5	25.46	127.1	263.5	96.4	2.003
1.75	25.47	122	272.6	99.7	2.004
2	25.48	117.2	284.8	104.2	2.005
2.25	25.49	114	284.8	104.2	2.006
2.5	25.50	110.8	272.6	99.7	2.006
2.75	25.50	144.4	0.0	0.0	2.006